Development of conductive SPM probes for applications in Biology

Thesis presented to apply for the degree of Doctor in Electronic Engineering at the
Department of Electronic Engineering of Universitat Autonoma de Barcelona

By

Yigezu Mulugeta Birhane
Instituto de Microelectronica de Barcelona
Centro Nacional de Microelectronica
IMB-CNM (CSIC)

Joan Bausells Roige
(Advisor and University Tutor)
Research Professor
Instituto de Microelectronica de Barcelona
Centro Nacional de Microelectronica
IMB-CNM (CSIC)
and
Associate Professor
Universitat Autonoma de Barcelona
UAB

April 2014

Centre Nacional de Microelectrònica IMB CSIC CONSEJO SUPERIOR DE INVESTIGACIONES CIENTÍFICAS UAB

This page is left blank intentionally.

INSTITUTO DE MICROELECTRONICA DE BARCELONA
CENTRO NACIONAL DE MICROELECTRONICA
IMB-CNM (CSIC)

Joan Bausells Roige, Research Professor at the Instituto de Microelectronica de Barcelona - Centro Nacional de Microelectronica (IMB-CNM, CSIC) and Associate Professor at the Universitat Autonoma de Barcelona (UAB)

CERTIFIES:

That the thesis entitled “**Development of conductive SPM probes for applications in Biology**” was carried out by **Yigezu Mulugeta Birhane** under his supervision within IMB-CNM.

Cerdanyola del Valles, April 2014.

Prof. Joan Bausells Roige

INSTITUTO DE MICROELECTRONICA DE
BARCELONA
CENTRO NACIONAL DE MICROELECTRONICA
IMB-CNM (CSIC)

Development of conductive SPM probes for applications in Biology by Yigezu Mulugeta Birhane- Consejo Superior de Investigaciones Cientificas (CSIC) and Universitat Autonoma de Barcelona (UAB), 2010. Thesis

To My Family.

Table of Contents

Acknowledgements

I would like to express my deepest gratitude to my thesis supervisor Prof. Joan Bausells, for giving me the opportunity to join the nanofabrication group of IMB-CNM and hence, the MEMS world. I am very much thankful for his many suggestions and constant support during this research work. I would like to thank Prof. Francesc Perez-Murano, Prof. Gabriel Gomila, Dr. Georg Gramse and Dr. Jordi Otero for their support in the electrical and mechanical characterization of the fabricated conductive SPM probes.

I gratefully acknowledge the financial support from the Consejo Superior de Investigaciones Cientficas (CSIC) under the JAE predoctoral fellowship, Bioelectronic olfactory neuron device (BOND) project of the 7th Framework Programme of the European Union (NMP4-SL-2009-228685), and MINECO through projects TEC2011-23600 and Nanoselect-CSD2007-00041(Consolider-Ingenio2010 programme).

My special thanks goes to my mother Tiringo, my lovely wife Hana, my cheerful little baby boy Naod and my sisters Emebet and Zinash.

I would like to thank also Jordi Llobet (for his help in getting very good SEM micrographs of the fabricated probes), Dr. Giordano Tosolini, Dr. Josep Montserrat, Miguel Zabala, Carles Mateu, Javier Sanchez, Marta Duch, Marta Gerboles, Josep Maria Cirera and Roser Mas for their invaluable discussions in developing the technology for the fabrication of insulated conductive SPM probes.

Finally, I wish to thank all clean room staffs of IMB-CNM for their technical support and all members (past and present) of the nanofabrication group of the IMB-CNM for keeping a wonderful working environment.

Barcelona, Spain Yigezu Mulugeta
April, 2014

List of Figures

List of Tables

Chapter 1

Introduction

1.1 Atomic Force Microscopy

Binning et al introduced the first probe based microscopy, scanning tunneling microscope (STM), in 1981 which is capable of obtaining atomic scale topographic image resolution at IBM research laboratory in Zurich [1, 2]. The same group also introduced the first atomic force microscopy (AFM) in 1985 [3]. Binning and Bohrer won the Nobel Prize in Physics in 1986 for their former work.

In the STM, the tunneling current between the probe tip and the sample is the key parameter for the imaging capability of the equipment. The atomic scale topographic resolution relies on the exponential dependence of the tunneling current on the separation between the probe tip and the sample surface. Since STM constructs topographic image based on the variation of the tunneling current as it scans the sample surface, it needs samples that conduct to some degree to make the topographic imaging. Whereas, in the case of AFM the probe cantilever deflection due to Van der Waals interaction between the probe tip and sample surface, which varies as a function of the distance between the tip and sample surface, is the key parameter for its topographic imaging capability. Therefore, AFM is capable of obtaining topographic image of any sample whether it is conducting or non-conducting.

In addition to topographic characterization of samples, AFM could also be used for the extraction of diverse physical and chemical properties of samples of interest such as magnetic force, electrostatic force, surface charge and surface potential profiles. The use of AFM to undertake these studies rely on the flexibility of AFM instrument to be integrated with other well developed instruments for the development of STM and AFM derivative methods. Some of the derivatives of the STM and AFM are magnetic force microscopy (MFM) [4], friction or lateral force microscopy (FFM or LFM) [5], scanning surface potential microscopy(SSPM)or Kelvin probe microscopy (KPM) [6, 7], scanning capacitance microscopy (SCM) [8, 9], scanning voltage microscopy (SVM) [10], scanning impedance microscopy (SIM) [11, 12], nanoimpedance microscopy (NIM) [11, 13], and etc. Some of these methods are used to take simultaneously topographic information of the sample and other complementary information which is important for the analysis of the sample under consideration. For example, the SSPM or KPM method is used to get simultaneously the topographic and electrostatic surface potential information of samples under investigation.

The AFM relies on the scanning technique to produce very high resolution, 3-D images of sample surfaces. It measures ultra small forces at the nanoscale present between the AFM tip and a sample surfaces [14] by measuring probe cantilever deflections. In most AFM equipments cantilever deflection is detected by optical beam deflection, as illustrated in figure 1.1. A laser beam bounces off the back of the cantilever and is centered on a split photodiode. Cantilever deflections under normal loading at the tip are proportional to the difference signal between the upper and lower halves of the photodetectors. Sub-angstrom deflections can be detected and,

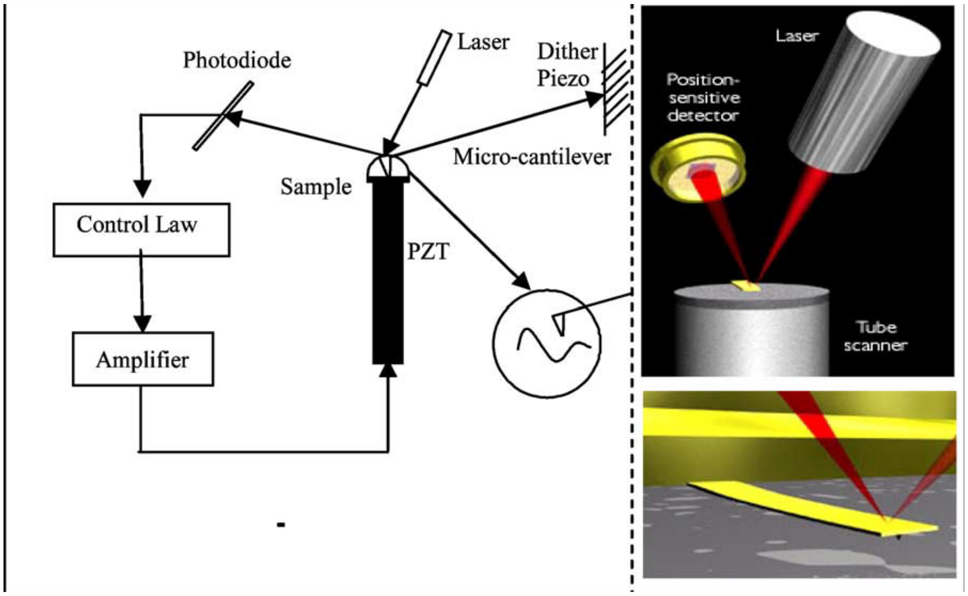

Figure 1.1: Schematic of basic AFM operation (left), real micro-cantilever and components (right) [14].

therefore, forces down to tens of picoNewtons can be measured. During scanning the AFMs operate either in contact (static), dynamic, or intermittent contact (tapping) mode of operations [14].

When AFM is operating in its contact mode, a sharp tip at the end of a cantilever brought in contact with a sample surface. During initial contact, the atoms at the end of the tip experience a very weak repulsive force due to electronic orbital overlap with the atoms in the sample surface. The force acting on the tip causes a cantilever deflection which is measured by tunneling, capacitive, or optical detectors. In the early days of contact mode AFM application, the deflection of the probe was continuously monitored to get information about the surface topology of the sample. Due to concerns of sample and probe tip damages, a feedback circuit has been developed to keep the probe deflection at a given deflection set point during scanning and the voltage applied to the z-piezo scanner by the feedback circuit to move the sample in order to keep the deflection of the cantilever at its set point gives topographic information of the sample.

Contrary to the static mode, in the dynamic mode of its operation the AFM probe tip is not in physical contact at any instant of time during imaging with the sample surface. In this mode the probe is externally driven to higher frequencies near its resonance frequency and the amplitude or phase shift is monitored during scanning. A feedback circuit is used to keep the probe not at a given deflection set point which is the case for the static mode but at given amplitude or phase shift set point. This mode minimizes or eliminates sample damage since there is no physical contact between sample and the probe tip during imaging. But the probe tip will stuck into the sample and eventually be broken while characterizing samples with this mode due to the existence of liquid meniscus in many sample surfaces.

In the tapping mode operation, the cantilever/tip assembly is driven to near or at its resonance frequency by a piezo mounted above it. The cantilever is held at constant amplitude (20-100nm) in the vertical direction. The oscillating tip slightly taps the sample surface only periodically during scanning. This mode minimizes or eliminates sample and/or probe damages observed during contact and dynamic mode operations. That is why tapping mode AFM topographic imaging is the most common mode than the other two. Similar to the dynamic mode, the variation from amplitude or phase set points during scanning gives information about the topography of the sample.

1.2 Scanning Probe Microscopy Probes

The probe is an essential part of the SPM machines. Various probes (cantilevers and tips) are used for SPM studies. The probe used in SPM should meet the following criteria: low normal spring constant (stiffness), a high resonance frequency, a high quality factor, high lateral stiffness, short cantilever length, and a sharp protruding tip. In order to register a measurable deflection with small forces, the cantilever must flex with relatively low forces (of the order of few nN), requiring a vertical probe cantilever stiffness of 0.01-100N/m for atomic resolution measurement in contact mode. The imaging rate in SPMs is limited by the mechanical resonance frequency of the probe cantilever used. The combined requirement of low probe cantilever stiffness and high resonance frequency is met by reducing the mass of the probe cantilever. In addition, the probes used for normal force profiling in contact mode should have high lateral stiffness value to minimize the effects of lateral forces between probe tip and sample surfaces. Whereas, low lateral stiffness cantilever probes are required to measure lateral (friction) force that exists between the probe tip and sample surfaces. The SPM probes should also have tip radii much smaller than the radii of corrugations in the sample in order for this to be measured accurately.

During the early days of AFM use, cantilevers were made by hand from thin metal foils or formed from fine wires. Tips for these cantilevers were prepared by attaching diamond fragments to the ends of the cantilevers by hand, or in the case of wire cantilevers by electrochemical etching of the wire to a sharp point [15, 16]. Various cantilever geometries such as L-shaped, V-shaped and double X-shaped configurations for wire cantilevers have been used [15, 16]. However, the small dimensions and low mass requirements of probes in various SPM uses made the hand fabrication of the cantilever a very difficult process with poor reproducibility. At the beginning of the 90s, several groups reported fabrication of cantilevers with tips using typical batch fabrication techniques from microelectronics (microfabrication) [17–23]. Conventional microfabrication technique is ideal for constructing planar thin-film structures which have sub-micron lateral dimensions. Most of the SPMs probes currently in use are fabricated with microcabrication techniques [24–27].

The unique feature of microfabrication technique compared to the hand fabrication is that cantilevers from whole range of materials could be fabricated. Most commonly cantilevers are made of silicon nitride, silicon, and Diamond. With microfabrication technique cantilevers and integrated tips could be fabricated from the same [24–27] or different [28] materials. Silicon nitride cantilevers are less expensive than those made of other materials. They are very rugged and well suited in imaging in almost all environments; are especially compatible for studying organic and biological samples. Microfabricated silicon nitride triangular beams with integrated square pyramidal tips made of plasma enhanced chemical vapor deposition (PECVD) are most commonly used [17]. An alternative to silicon nitride cantilevers with integrated tips are microfabricated single-crystal silicon cantilever with integrated tips. One of the advantage of Silicon probes over the silicon nitride ones is that silicon probes with very sharp tips could be fabricated owing to the existence of orientation dependent wet etching condition for single crystal silicon. Single crystal silicon tips with tip radii less than 10nm could be microfabricated [18].

For electrical measurement of samples using SPM, one needs conductive SPM probes. There are wide classes of conducting probes for use in electrical characterization of samples using SPM equipment which are fabricated by different microfabrication techniques. Some of these probes are all metal SPM probes and conventional SPM probes with conducting layer realized by different techniques [29–32]. The conducting layer goes from the electrical contact pad area to the apex of the tip. For electrical measurement of samples in air there is no material restriction as a tip material as long as it is electrically conducting. But for the application in liquid environment one needs to take in to account the wear resistance and the electrochemical neutrality of the tip materials. The SPM electrical characterization technique has been extended by some groups for electrical characterization of small signal samples such as Biological samples [33]. For these applications one needs conductive SPM probes that are electrically isolated from the environment except at the apex of the tip and pad area where electrical contact with the sample and external circuitry is made, respectively.

SPM could also be used for scratching, wear, indentation and nanolithogrphy study of samples. For these studies specifically microfabricated SPM probes with Pyramidal diamond tips are needed. These studies rely on the hardness of diamond compared to silicon and silicon nitride tips [34].

1.3 Impedance Spectroscopy

1.3.1 Bulk Impedance Measurement

Impedance is systems property to impede the flow of electrical current in the system. The impedance is defined as the ratio of the sinusoidal voltage signal applied across the system to the resulted sinusoidal current response. By measuring the impedance over a range of frequencies, an impedance spectrum could be constructed. The frequency-resolved modulus (amplitude of impedance) and phase angle (phase difference between the applied sinusoidal voltage and current response) information allows the extraction of some relaxation times of the system. These relaxation times could be associated with various physicochemical processes including ionic transport, charge transfer, and diffusion [11].

Impedance measurements are generally performed in either a two-electrode or a four-electrode configuration. In the two-electrode configuration, a sinusoidal voltage perturbation is applied across a sample of interest through two contacting electrodes and the resulting sinusoidal current response is measured (figure 1.2(a)). In this set-up, the measured impedance includes the response from the system and the electrodes. An alternative is the four-probe impedance measurement, in which electrode contribution is separated from the system response (figure 1.2(c)). Because standard IS measurements utilize bulk electrodes, the technique produces bulk, or system-averaged, results. In other words, standard IS measurements do not provide spatial resolution. Due to the rapid development of electrical scanned-probe techniques, it is now possible to combine the capabilities of SPM with impedance measurement to acquire spatially resolved impedance measurements (figure 1.2(b,d)). If the impedance spectroscopy is employed to measure the impedance of a solution, then the technique is generally called electrochemical impedance spectroscopy [35].

1.3.2 Localized Impedance Measurement

With the advent of AFM many local characterization schemes are developed by integrating the AFM with the other well developed technologies. Integrating the AFM

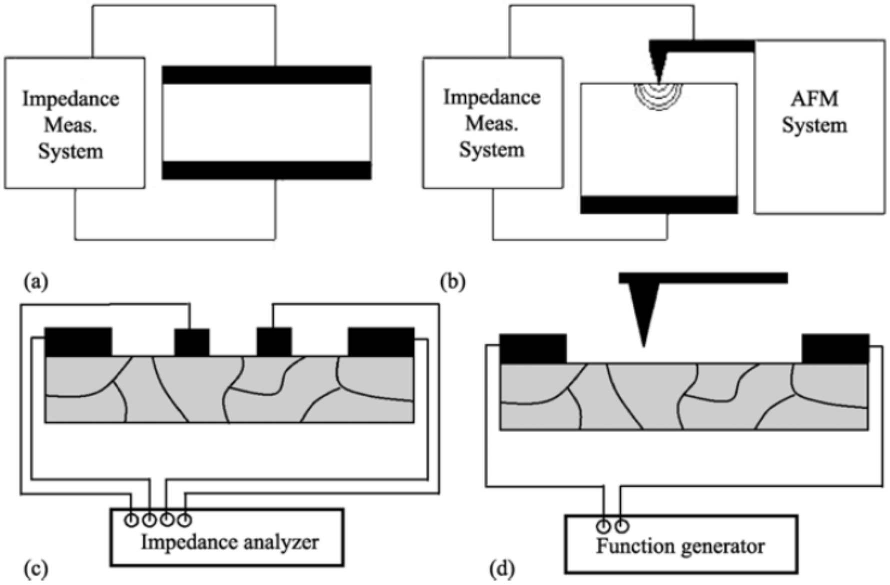

Figure 1.2: Bulk vs. SPM impedance measurement. (a) General concept of a two-electrode impedance measurement. An impedance measurement system acquires an ac impedance spectrum from a sample of interest sandwiched between two bulk electrodes. (b) In SPM impedance measurement, impedance is measured between a local probe (the SPM tip) and a bulk electrode. (c) Four probe impedance measurements allowing minimization of contact contribution to measured impedance. (d) In Scanning impedance microscopy, tip acts as a force-based moving voltage electrode, enabling spatial resolution [11].

with the impedance spectroscopy provides one with the local impedance characterization of samples which is not possible with the conventional impedance spectroscopy equipment alone. To this end, in the case of nanoimpedance spectroscopy, the AFM probe tip substitutes one of the bulk electrodes in the conventional two electrode impedance spectroscopy (figure 1.2(b)). Hence, in this case the AFM probe is used as current sensing electrode. While in the scanning impedance spectroscopy, the AFM probe is used as a local voltage sensing electrode to trace local voltage distribution (figure 1.2(d)).

Recently, the use of AFM based impedance measurements in Biology has been demonstrated [36]. The schematic measuring system is as shown in the figure 1.3. It consists of a commercial AFM coupled to a custom-made current-to-voltage amplifier connected to the AFM tip. While scanning in contact over the surface under force feedback control, a sinusoidal input voltage signal,$\nu_{AC}(\omega)$, is applied between the AFM probe and the bottom electrode of the sample, and the ac current $\iota_{AC}(\omega)$ that flows through the sample is measured by the current amplifier. The amplified signal is fed into an analogue lock-in-board included in the AFM electronics, which measures the in-phase and out-of-phase components of the current, thus extracting the real part (conductance, G) and imaginary part (susceptance,B), respectively, of the sample admittance (the inverse of the impedance, $\frac{1}{Z}$). The lock-in-analogue outputs are then sampled simultaneously to the AFM control signals by the 16 bit 15kSs^{-1} analogue-to-digital (ADC) board of the AFM electronics. Thus, simultaneously to the acquisition of topography, images of conductance G and susceptance B are acquired in real time.

For electrical characterization of samples in liquid environment with this instrumentation, there are two parasitic impedance sources. These are the parasitic conductance between the conducting layer in the extended probe cantilever and the liquid environment. And the second source of parasitic impedance signal is the stray capacitance coupling between the sample and cone apex, cantilever, probe chip and probe holder as shown in figure 1.4. The magnitude of the parasitic impedance signal will be higher than the actual impedance coupling between the AFM probe tip and small signal samples, such as biological samples. Therefore, the conductive AFM probes employed for electrical characterization of biological samples should minimize the parasitic impedance signal. This can be done by adding an additional dielectric

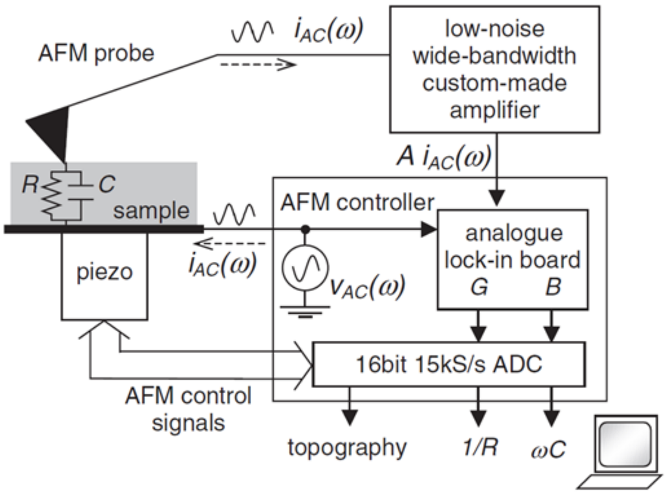

Figure 1.3: Diagram of the instrumentation for capacitance imaging using ac current sensing AFM. While the AFM tip is maintained in contact with the surface under scanning force control, simultaneous topography and capacitance imaging is performed. A custom-made current-to-voltage amplifier, connected to the AFM tip and coupled to a lock-in board included in the AFM electronics, allows measurement of the admittance, of both real part G (conductance, $G = \frac{1}{R}$) and the imaginary part (susceptance, $B = \omega C$), of the sample. The capacitance image is obtained directly from the imaginary component of the admittance [36].

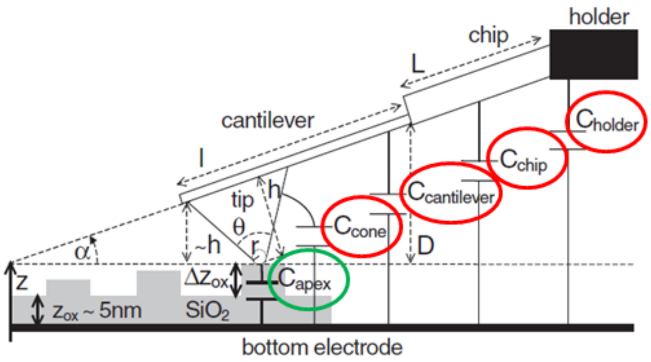

Figure 1.4: Diagram of the AFM probe in contact with the silicon oxide nanostructure. The total capacitance is modeled by five capacitors in parallel (tip apex, tip cone, cantilever, chip and tip holder). Only the tip apex capacitor represents the local capacitance, whereas the others are parasitic contributions [36].

material, which encapsulates the conducting layer in the probe except the probe tip and in the electrical contact pad area, and by engineering the conducting layer in the probe to minimize the parasitic conductance between the extended probe cantilever and the liquid environment and the stray capacitance contributions to the parasitic impedance signal, respectively.

1.4 The Bioelectronic Olfactory Neuron Device (BOND) Project

The Bioelectronic olfactory neuron device (BOND) project developed a new electronic nose device whose odor sensitive part was based on olfactory neurons prepared in the form of nanoliposomes (nanosomes) immobilized into a nanoelectrode with special immobilization techniques. It was previously demonstrated experimentally that the detection of specific odorants by nanoliposomes containing olfactory receptors (ORs) immobilized on microelectrodes produces a change in the polarization resistance of

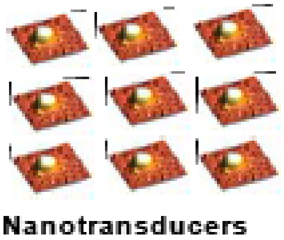

Figure 1.5: Nanoelectrodes immobilized with nanosomes.

the impedance spectrum of the biosensor. The magnitude of the changes was unambiguously correlated the concentration of odorant molecules. Polarization resistance can be associated to electrochemical reactions taking place at the electrode (background current). Nanosome response was inferred to affect these processes indirectly through changes in its intrinsic electrical properties, mainly, its polarizability associated to the ORs conformational change. However, these conclusions were reached by modeling an isolated protein, and thus a deeper understanding including the whole nanovesicle and the liquid media become necessary. To this end the nanobiosensor should be characterized using electrochemical impedance spectroscopy technique using specifically microfabricated conductive SPM probes to have deeper understanding of the working principle of the Biosensors [33].

To mimic the working principle of the mammalian sense of odor, array nanoelectrodes immobilized with specific types of olfactory receptors have been proposed as the nanoplatform for the Biosensor. The nanoplatform for the Biosensor is as shown in the figure 1.5. Signal is acquired from each Biosensor by the signal processing unit and the pattern recognition unit discriminates the odor molecules in a mixture comparing with previously acquired information of known samples which is similar to the the working principle of the mammalian sense of odor.

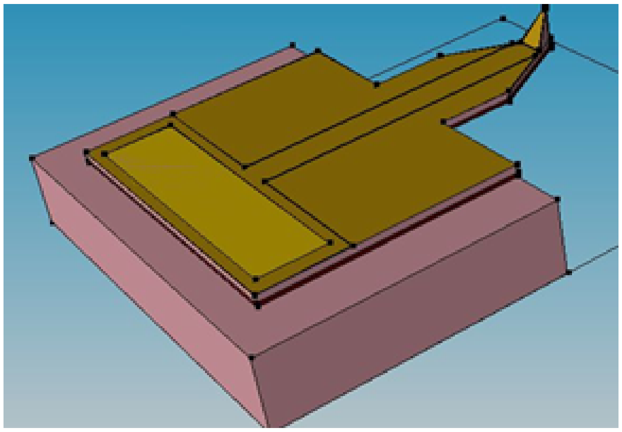

Figure 1.6: Schematic diagram of insulated C-SPM probe for low noise electrical characterization of samples in liquid invironment

The Bioelectronic olfactory neuron device developed by our project partners will be characterized with the recently developed SPM based electrical characterization technique for Biology. For this specifically microfabricated conductive SPM probes which are insulated with a dielectric material except at contact pad area and at the apex of the probe tip are required. The commercial scanning probe microscopy probes are not useful for this applications due to lack of electrical insulation which increases the dc parasitic current between the extended probe cantilever and the sample. And the other source of parasitic impedance signal in the commercial scanning probe microscopy probes is the stray capacitive between the sample and the extended probe cantilever, cone apex and probe substrate. To minimize the stray capacitance contributions to the parasitic impedance signal one needs to engineer the conducting layer in the scanning probe microscopy probes. Schematic diagram of the SPM probe that minimizes both the parasitic DC and AC impedances is shown in the figure 1.6. The fabrication of conductive scanning probe microscopy probes which are used for low noise electrical measurement in Biology is the objective of this thesis work.

1.5 Thesis outline

The following chapters are organized as follows:

Chapter 2 Theoretical back ground. In this chapter first the theoretical and finite element method simulation (FEM)studies of crystalline silicon rectangular cantilever beams will be presented. Then the theoretical and FEM simulation studies of crystalline silicon rectangular cantilever beams with an additional thin plasma enhanced chemical vapor deposited (PECVD) silicon nitride layer will be presented to understand the modulations to the mechanical properties of the silicon cantilever due to the additional dielectric material.

Chapter 3 - Design and fabrication. In this chapter we will present the mask design and the fabrication of insulated conductive scanning probe microscopy (C-SPM) probes that could be employed for local electrical and mechanical characterization of Biological samples in their physiological environment.

Chapter 4 - Mechanical and Electrical characterization. In this chapter, the mechanical and electrical characterization of the fabricated insulated C-SPM probes in air performed to extract the mechanical properties (force constant, fundamental resonance frequency and tip radii) and to understand the electrical behavior of the probes will be presented.

Chapter 5 - Conclusions. In this chapter, we will highlight the most important results of the work and give suggestions for future research directions.

Appendix - We will conclude the thesis work by presenting the list of our publications and conference presentations during this research work in the appendix.

Bibliography

[1] G. Binnig, H. Rohrer, Ch. Gerber, and E. Weibel. Tunneling through a controllable vacuum gap. *Applied Physics Letters*, 40(2):178–180, 1982.

[2] G. Binnig, H. Rohrer, Ch. Gerber, and E. Weibel. Surface studies by scanning tunneling microscopy. *Phys. Rev. Lett.*, 49:57–61, Jul 1982.

[3] G. Binnig, C. F. Quate, and Ch. Gerber. Atomic force microscope. *Phys. Rev. Lett.*, 56:930–933, Mar 1986.

[4] D. Rugar, H. J. Mamin, P. Guethner, S. E. Lambert, J. E. Stern, I. McFadyen, and T. Yogi. Magnetic force microscopy: General principles and application to longitudinal recording media. *Journal of Applied Physics*, 68(3), 1990.

[5] E Meyer, R Lthi, L Howald, W Gutmannsbauer, H Haefke, and H-J Gntherodt. Friction force microscopy on well defined surfaces. *Nanotechnology*, 7(4):340, 1996.

[6] Wilhelm Melitz, Jian Shen, Andrew C. Kummel, and Sangyeob Lee. Kelvin probe force microscopy and its application. *Surface Science Reports*, 66(1):1 – 27, 2011.

[7] Th. Glatzel, M. Ch. Lux-Steiner, E. Strassburg, A. Boag, and Y. Rosenwaks. Principles of kelvin probe force microscopy. In Sergei Kalinin and Alexei Gruverman, editors, *Scanning Probe Microscopy*, pages 113–131. Springer New York, 2007.

[8] G. Gomila, J. Toset, and L. Fumagalli. Nanoscale capacitance microscopy of thin dielectric films. *Journal of Applied Physics*, 104(2):024315, 2008.

[9] J. J. Kopanski. Scanning capacitance microscopy for electrical characterization of semiconductors and dielectrics. In Sergei Kalinin and Alexei Gruverman, editors, *Scanning Probe Microscopy*, pages 88–112. Springer New York, 2007.

[10] Scott B. Kuntze, Dayan Ban, Edward H. Sargent, St. John Dixon-Warren, J. Kenton White, and Karin Hinzer. Scanning voltage microscopy: Investigating the inner workings of optoelectronic devices. In Sergei Kalinin and Alexei Gruverman, editors, *Scanning Probe Microscopy*, pages 561–600. Springer New York, 2007.

[11] Ryan OHayre, Minhwan Lee, FritzB. Prinz, and SergeiV. Kalinin. Frequency-dependent transport imaging by scanning probe microscopy. In Sergei Kalinin and Alexei Gruverman, editors, *Scanning Probe Microscopy*, pages 132–172. Springer New York, 2007.

[12] Sergei V. Kalinin and Dawn A. Bonnell. Scanning impedance microscopy of an active schottky barrier diode. *Journal of Applied Physics*, 91(2):832–839, 2002.

[13] Ryan O'Hayre, Gang Feng, William D. Nix, and Fritz B. Prinz. Quantitative impedance measurement using atomic force microscopy. *Journal of Applied Physics*, 96(6):3540–3549, 2004.

[14] Nader Jalili and Karthik Laxminarayana. A review of atomic force microscopy imaging systems: application to molecular metrology and biological sciences. *Mechatronics*, 14(8):907 – 945, 2004.

[15] Y. Martin, C. C. Williams, and H. K. Wickramasinghe. Atomic force microscope-force mapping and profiling on a sub 100- scale. *Journal of Applied Physics*, 61(10):4723–4729, 1987.

[16] O. Marti, B. Drake, and P. K. Hansma. Atomic force microscopy of liquid-covered surfaces: Atomic resolution images. *Applied Physics Letters*, 51(7):484–486, 1987.

[17] T. R. Albrecht, S. Akamine, T. E. Carver, and C. F. Quate. Microfabrication of cantilever styli for the atomic force microscope. *Journal of Vacuum Science and Technology A*, 8(4):3386–3396, 1990.

[18] O. Wolter, Th. Bayer, and J. Greschner. Micromachined silicon sensors for scanning force microscopy. *Journal of Vacuum Science and Technology B*, 9(2):1353–1357, 1991.

[19] P. Grutter, D. Rugar, H. J. Mamin, G. Castillo, S. E. Lambert, C.-J. Lin, R. M. Valletta, O. Wolter, T. Bayer, and J. Greschner. Batch fabricated sensors for magnetic force microscopy. *Applied Physics Letters*, 57(17):1820–1822, 1990.

[20] R.A. Buser, J. Brugger, C. Linder, and N.-F. de Rooij. Micromachined silicon cantilevers and tips for bidirectional force microscopy. In *Solid-State Sensors and Actuators, 1991. Digest of Technical Papers, TRANSDUCERS '91., 1991 International Conference on*, pages 249–252, June 1991.

[21] M M Farooqui, A G R Evans, M Stedman, and J Haycocks. Micromachined silicon sensors for atomic force microscopy. *Nanotechnology*, 3(2):91, 1992.

[22] J. Brugger, R.A. Buser, and N.F. de Rooij. Silicon cantilevers and tips for scanning force microscopy. *Sensors and Actuators A: Physical*, 34(3):193 – 200, 1992.

[23] J Brugger, R A Buser, and N F de Rooij. Micromachined atomic force microprobe with integrated capacitive read-out. *J. Micromech. Microeng*, 2:218–220, 1992.

[24] B. W. Chui, T. D. Stowe, T. W. Kenny, H. J. Mamin, B. D. Terris, and D. Rugar. Low-stiffness silicon cantilevers for thermal writing and piezoresistive readback with the atomic force microscope. *Applied Physics Letters*, 69(18):2767–2769, 1996.

[25] G. Villanueva, J.A. Plaza, A. Sanchez, K. Zinoviev, F. Perez-Murano, and J. Bausells. DRIE based novel technique for AFM probes fabrication. *Microelectronic Engineering*, 84(58):1132 – 1135, 2007.

[26] R.P. Ried, H.J. Mamin, B.D. Terris, Long-Sheng Fan, and D. Rugar. 6-MHz 2-N/m piezoresistive atomic-force microscope cantilevers with INCISIVE tips. *Microelectromechanical Systems*, 6(4):294–302, 1997.

[27] J Thaysen, A Boisen, O Hansen, and S Bouwstra. Atomic force microscopy probe with piezoresistive read-out and a highly symmetrical wheatstone bridge arrangement. *Sensors and Actuators A: Physical*, 83(13):47 – 53, 2000.

[28] Shinya Akamine and Calvin F. Quate. Microcantilever with integral self-aligned sharp tetrahedral tip. *U.S. Patent*, (5,021,364), June, 1991.

[29] A. Kueng, C. Kranz, B. Mizaikoff, A. Lugstein, and E. Bertagnolli. Combined scanning electrochemical atomic force microscopy for tapping mode imaging. *Applied Physics Letters*, 82(10):1592–1594, 2003.

[30] Phillip S. Dobson, John M. R. Weaver, Mark N. Holder, Patrick R. Unwin, and Julie V. Macpherson. Characterization of batch-microfabricated scanning electrochemical-atomic force microscopy probes. *Analytical Chemistry*, 77(2):424–434, 2005.

[31] J A J Steen, J Hayakawa, T Harada, K Lee, F Calame, G Boero, A J Kulik, and J Brugger. Electrically conducting probes with full tungsten cantilever and tip for scanning probe applications. *Nanotechnology*, 17(5):1464, 2006.

[32] Jun Zou, Xuefeng Wang, David Bullen, Kee Ryu, Chang Liu, and Chad A Mirkin. A mould-and-transfer technology for fabricating scanning probe microscopy probes. *Journal of Micromechanics and Microengineering*, 14(2):204, 2004.

[33] A. Errachid et al. G. Gomila, I. Casuso. Advances in the production, immobilization, and electrical characterization of olfactory receptors for olfactory nanobiosensor development. *Sens. Actuators B: Chemical*, 116:66–71, 2006.

[34] Keun-Ho Kim, Nicolaie Moldovan, Changhong Ke, Horacio D. Espinosa, Xingcheng Xiao, John A. Carlisle, and Orlando Auciello. Novel ultrananocrystalline diamond probes for high-resolution low-wear nanolithographic techniques. *Small*, 1(8-9):866–874, 2005.

[35] E. Masi E. Azzarello and S. Mancuso. Electrochemical impedance spectroscopy. In Alexander G. Volkov, editor, *Plant Electrophysiology: Methods and Cell Electrophysiology*, pages 205–225. Springer New York, 2012.

[36] L Fumagalli, G Ferrari, M Sampietro, I Casuso, E Martnez, J Samitier, and G Gomila. Nanoscale capacitance imaging with attofarad resolution using AC current sensing atomic force microscopy. *Nanotechnology*, 17(18):4581, 2006.

Chapter 2

Mechanics of Cantilever Beams

2.1 Introduction

A cantilever beam is a mechanical structure anchored at one end and free at another end. It is a well known mechanical structure that has been widely used in constructions during the last two centuries [1], mainly for bridges and balconies. In addition, they have also been used as mechanical transducers in some sensors, e.g. with strain gauges for force or thermal gradient measurements, as fundamental part of some devices like phonograph, etc.

As a mechanical transducer such as in AFM probe, cantilever beams can be used in two different modes of operations, namely static and dynamic modes. In the static mode of operation, static deflection of cantilever in response to an applied loads is continuously monitored (figure 2.1). Whereas, in the dynamic mode changes in the resonant frequency, phase or amplitude of mechanical vibrations are measured (figure 2.2).

Deformations in cantilever profile (static mode) can be produced by acceleration, mechanical surface stress and punctual forces, while changes in resonant frequency

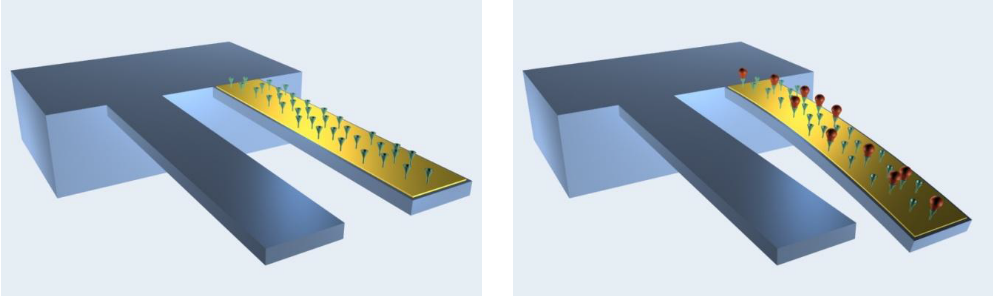

Figure 2.1: Schematic of a typical static-mode operation. Two cantilevers, one of them with a gold and functionalized layer on top and the other working as a reference cantilever (left), are exposed to the flux of some biomolecules, which will bind with the functionalization of measuring cantilever causing it to deflect (right) [2].

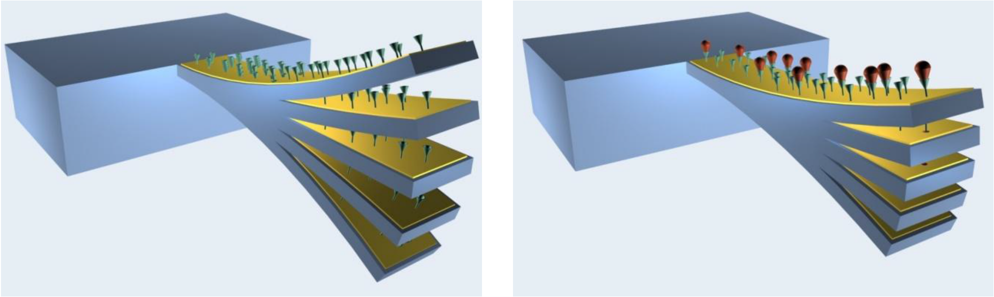

Figure 2.2: Schematic of a typical dynamic-mode operation. A functionalized cantilever is oscillating at its resonant frequency (left). When biomolecules bind to the surface, mass of the cantilever increases, causing the resonant frequency to decrease (right) [2].

can be produced by mass addition and punctual forces. As transducers, cantilevers sensitivity is bigger when decreasing their dimensions. Hence, the smaller the cantilever, the more sensitive it is.

In order to quantify an external load applied to a cantilever beam necessitates knowledge of some of the mechanical properties of the beam such as its force constant and fundamental resonance frequency of the mechanical vibrations. These information could be obtained analytically using beam equations derived using small deformation approximation or using the finite element modeling technique.

In this chapter we will present the static and transient studies of cantilever beams to choose cantilever dimensions for the design of AFM probes that satisfy the specifications as required by the BOND project [3]. The solutions extracted using the beam equations will be compared with those obtained using the Finite Element method (FEM) simulation technique to know the significance of approximations taken in driving the beam equations. We will also make FEM simulations of a simple rectangular crystalline silicon cantilever beams with an additional thin dielectric material to obtain the modulation to the static and dynamical responses of the simple rectangular silicon cantilever beams due to the additional thin dielectric material.

2.2 Analytical study

2.2.1 Static Response

A typical AFM probe geometry with length L, width b and thickness h cantilever dimensions and tip height ℓ is shown in the figure 2.3. In the static mode of AFM operation, the force on the tip due to tip-sample interaction is translated into cantilever deflection and gives topographic information of the sample [4]. To quantify the interaction force between the AFM probe tip and the sample under investigation, one should know the force constant of the probe cantilever in use. To this end, if a concentrated punctual force W (which can be positive or negative depending on the choice of the coordinate axes) is applied at the free end of a cantilever beam, then its bending moment about an axis passing through a point x from the free end of the cantilever in the direction of the thickness h of the cantilever is given by [5],

$$M(x) = EI(x)\frac{d^2y}{dx^2} = Wx, \tag{2.2.1}$$

where, $M(x)$ is the bending moment at a point x due to the loading W at the free end of the beam, E is the Young's Modulus of the beam, x is the distance along the length of the beam measured from its free end and $I(x)$ is the second moment of area of the beam at point x along the cantilever length which is given by the expression,

$$I(x) = \int_{y=0}^{b(x)} \int_{z=-\frac{h(x)}{2}}^{\frac{h(x)}{2}} z^2 dydz. \tag{2.2.2}$$

For cantilever beams with uniform cross-sectional area, one could get the deflection of the cantilever at point x from its free end along the cantilever length by integrating equation 2.2.1 twice and then inserting the appropriate boundary conditions as,

$$y = \frac{1}{EI}[\frac{Wx^3}{6} - \frac{WL^2x}{2} + \frac{WL^3}{3}]. \tag{2.2.3}$$

And the expression for the second moment of area for a uniform cantilever beam reduces to,

$$I = \frac{h^3b}{12}. \tag{2.2.4}$$

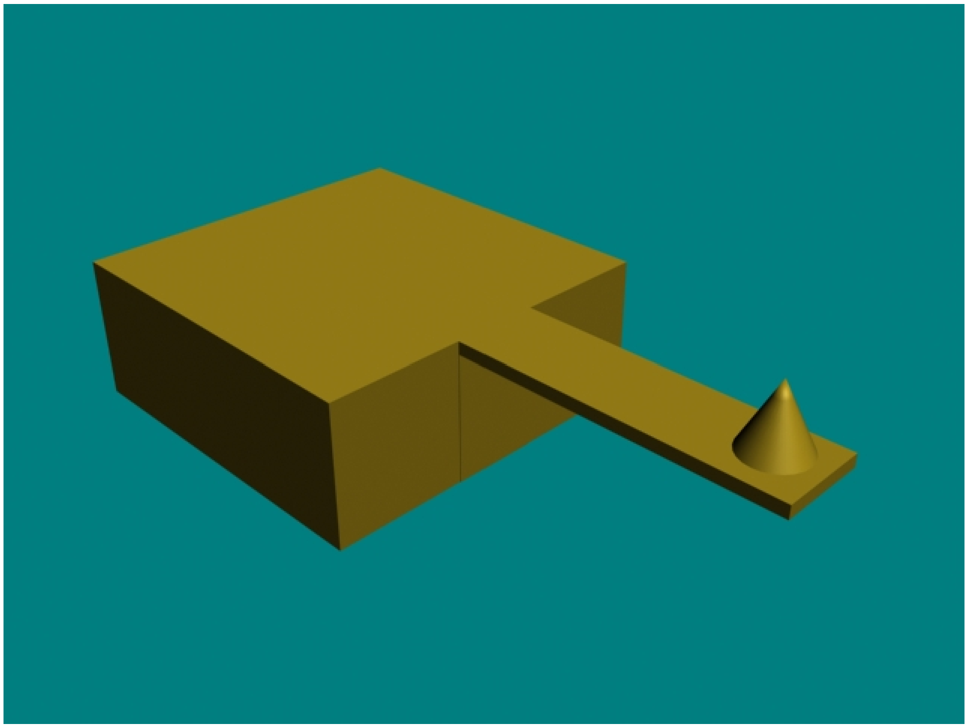

Figure 2.3: A typical AFM probe structure

The maximum deflection of the cantilever occurs at its free end and is given by,

$$y_{max} = \frac{WL^3}{3EI}. \tag{2.2.5}$$

Hence, the force constant k of the cantilever becomes

$$k = \frac{3EI}{L^3}, \tag{2.2.6}$$

By substituting equation 2.2.4 into equation 2.2.6, the force constant of the cantilever beam is expressed using only the geometrical parameters of the cantilever and the Young's modulus of the material it made of as,

$$k = \frac{Ebh^3}{4L^3}. \tag{2.2.7}$$

2.2.2 Vibrational Mode

In the dynamic operation modes of an AFM, the probe cantilever is deliberately vibrated at or close to the fundamental mechanical resonance frequency f_0 of the probe cantilever. There are two basic methods of dynamic operation: amplitude modulation (AM) and frequency modulation (FM) operation. In AM-AFM, the actuator is driven by a fixed amplitude A_{drive} at a fixed frequency f_{drive}, where f_{drive} is close to f_0. When the tip approaches the sample, elastic and inelastic interactions cause a change in both the amplitude and the phase (relative to the driving signal) of the cantilever. These changes are used as the feedback signal [4].

The change in amplitude in AM mode does not occur instantaneously with a change in the tip-sample interaction, but on a time scale of $\tau_{AM} \approx 2Q/\ f_0$, where Q is the quality factor of the cantilever beam. Hence, the AM mode is slow with high-Q cantilevers [4]. However, the use of high Q-factors reduces noise. Whereas in the frequency modulation (FM) mode, the change in eigenfrequency settles on a time scale of $\tau_{FM} \approx \frac{1}{f_0}$ [6]. Hence, the fundamental mechanical resonance frequency of an AFM probe cantilever is one factor that determines the scanning speed of AFM in its dynamic operation modes.

In the previous section, we have used the static response (static deflection) of a cantilever beam to a normal force applied at its free end to extract its force constant value. To understand the dynamics of a cantilever beam (namely the time rate of change of cantilever deflection) one should solve the partial differential equation governing the beam dynamics. Boundary conditions allow only certain solutions of the differential equation. Each solution or mode of vibration is characterized by a certain discrete frequency. Transversal vibrations of a cantilever beam in the direction of the beam thickness is described by the the partial differential equation [7,8]

$$\frac{\partial^2}{\partial x^2}(EI(x)\frac{\partial^2 y}{\partial x^2}) = \mu\frac{\partial^2 y(x)}{\partial t^2}. \tag{2.2.8}$$

If $I(x)$ is not function of x which is the case for a uniform beam and E is not function of x as well, 2.2.8 reduces to,

$$EI\frac{d^4 y(x)}{dx^4} - \mu\frac{d^2 y(x)}{dt^2} = 0, \tag{2.2.9}$$

where μ is the mass per unit length of the beam. By solving equation 2.2.9, one can get the angular resonance frequencies for the different modes of oscillation of a cantilever beam with length L, width b and thickness h as,

$$\begin{aligned}
\omega_1 &= (1.03\frac{E}{\rho_m})^{\frac{1}{2}}\frac{h}{L^2} && (2.2.10)\\
\omega_2 &= (40.5\frac{E}{\rho_m})^{\frac{1}{2}}\frac{h}{L^2} && (2.2.11)\\
\omega_n &= (\frac{(2n-1)^4\pi^4}{192}\frac{E}{\rho_m})^{\frac{1}{2}}\frac{h}{L^2}; \forall n \geq 2, && (2.2.12)
\end{aligned}$$

where ρ_m is the mass density of the cantilever beam and ω_i is the angular resonance frequency of the i^{th}-mode of oscillation of the cantilever beam.

2.3 FEM Simulation of rectangular cantilever beams

The Finite Element Method (FEM)is a powerful computational technique for approximate solutions to a variety of "real-world" engineering problems having complex domains subjected to general boundary conditions. FEM has become an essential step in the design or modeling of a physical phenomenon in various engineering disciplines [9].

The basis of FEM relies on the decomposition of the domain into a finite number of subdomains (elements) for which the systematic approximate solution is constructed by applying the variational or weighted residual methods. In effect, FEM reduces the problem to that of a finite number of unknowns by dividing the domain into elements and by expressing the unknown field variable in terms of the assumed approximating functions within each element. These functions (also called interpolation functions) are defined in terms of the values of the field variables at specific points, referred to as nodes. Nodes are usually located along the element boundaries, and they connect adjacent elements. The number of nodes used in an element also decides the degree of the interpolation functions.

We will simulate the mechanics of simple crystalline silicon cantilever beams with rectangular dimensions and compare the results with the analytical counter part to see the significance of the approximation taken in the derivation of the analytical expressions. Then we will simulate the simple rectangular crystalline silicon cantilever beams with an additional thin PECVD grown silicon nitride layer and compare the simulation results with that of the simple rectangular crystalline silicon beam to observe the magnitude of the force constant and resonance frequency modulations of the beams due to the additional dielectric material. In these simulations, simple rectangular cantilever beam with displacement loading acted at the base of a cantilever connecting it with the chip will be used [2].

2.3.1 Static Response

The static FEM simulation was performed to extract the force constant of the different rectangular cantilever beams shown in table 2.1. In this simulation, in addition to the displacement loading at the base of a cantilever connecting with the chip, a concentrated normal loading of 100nN was applied at the free end of the cantilevers. Figure 2.4 shows the static deflections of the $L3$ and $L9$ cantilever beams in response to the normal loading. And the force constant of the different cantilever beams obtained using the static FEM simulation and the analytical techniques are shown in the K_{FEM} and K_{th} columns of table 2.3, respectively.

2.3.2 Vibrational Mode

The transient simulation was used to extract the dynamical properties of the cantilevers, the mechanical resonance frequencies. The first two modes of vibrations of the $L3$ and $L9$ beams are shown in the figures 2.5 and 2.6, respectively. The fundamental resonance frequency of the different rectangular cantilever beams (table 2.1) obtained using the transient FEM simulation are shown in the column f_{FEM} of table 2.3. And for comparison, the fundamental resonance frequencies of the beams

Table 2.1: Rectangular cantilever beams considered in the static and transient FEM simulation study to extract the force constant and resonance frequencies of the beams.

cantilever	length	width	thickness
L1	$200\mu m$	$40\mu m$	$4\mu m$
L2	$200\mu m$	$30\mu m$	$4\mu m$
L3	$250\mu m$	$40\mu m$	$4\mu m$
L4	$250\mu m$	$30\mu m$	$4\mu m$
L5	$275\mu m$	$40\mu m$	$4\mu m$
L6	$275\mu m$	$30\mu m$	$4\mu m$
L7	$300\mu m$	$40\mu m$	$2\mu m$
L8	$300\mu m$	$30\mu m$	$2\mu m$
L9	$400\mu m$	$40\mu m$	$2\mu m$
L10	$400\mu m$	$30\mu m$	$2\mu m$

Table 2.2: Material properties of crystalline silicon

material properties	
Young's modulus (E)	160GPa
Mass density (ρ_m)	2330 kg/m^3
Poisson coefficient (υ)	0.27

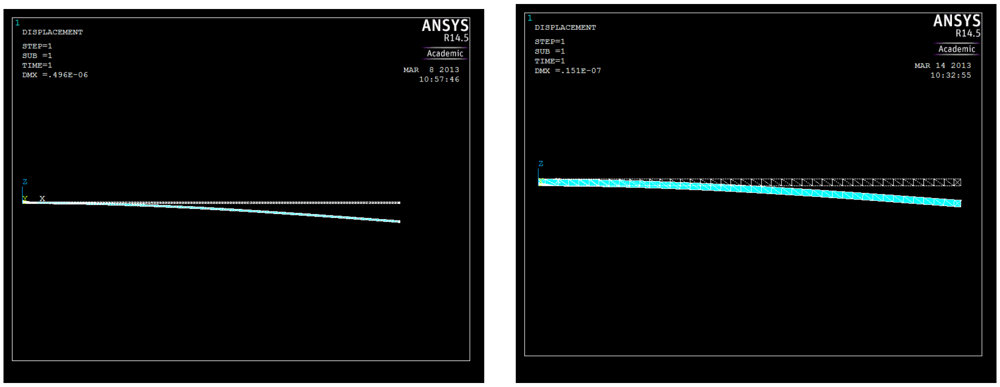

Figure 2.4: The static responses (static deflections) of $L9$(left) and $L3$ (right) cantilever beams under 100nN normal loading at the free end of the cantilevers.

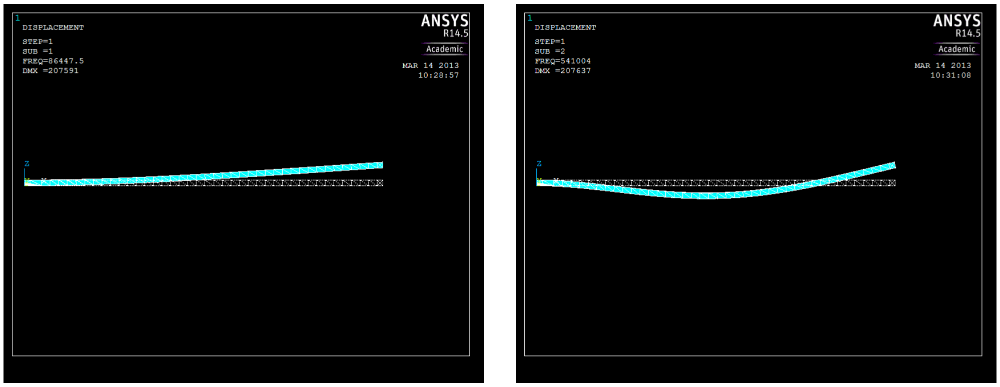

Figure 2.5: The first two modal solutions of $L3$ cantilever beam. The fundamental mode (left) and the first harmonics (right).

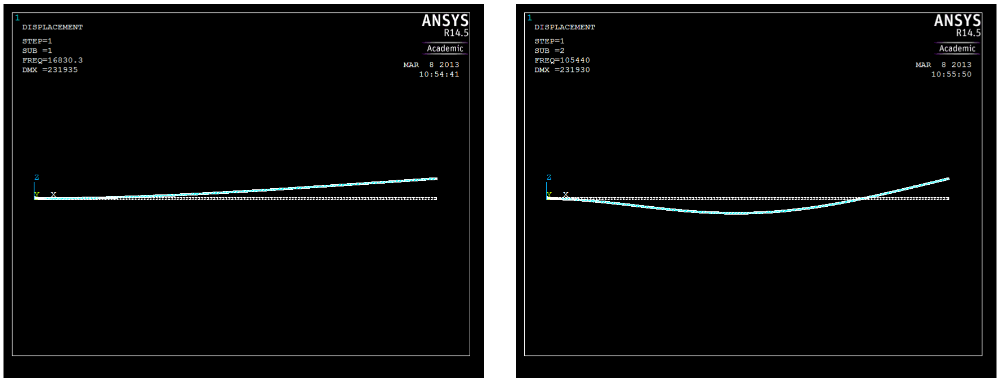

Figure 2.6: The first two modal solutions of $L9$ cantilever beam.The fundamental mode (left) and the first harmonics (right).

obtained with the beam equations are shown in column f_{th} of the same table. As could be seen in the table 2.3, the variations of the FEM and the analytical solutions of the force constant and fundamental resonance frequency values of the rectangular cantilever beams are very small indicating that the approximations taken in the derivation of the beam equations are not significant.

As can be seen in the table 2.3, the force constant and fundamental resonance frequency of vibrations of the different cantilever beams obtained using the beam equations and the finite element modeling technique are approximately equal. This

Table 2.3: The force constant and fundamental resonance frequencies of crystalline silicon cantilever beams obtained using the beam equations and FEM simulations

	k_{th}(N/m)	k_{FEM}(N/m)	f_{Th}(kHz)	f_{FEM}(kHz)
L1	12.800	13.210	135.303	133.918
L2	9.600	9.708	134.993	133.918
L3	6.554	6.623	85.708	86.447
L4	4.915	4.975	85.708	86.264
L5	4.924	3.73	70.833	71.383
L6	3.693	3.731	70.833	71.241
L7	0.474	0.478	29.76	29.973
L8	0.356	0.358	29.76	29.920
L9	0.2	0.202	16.74	16.83
L10	0.15	0.151	16.74	16.807

indicates that the approximations taken in driving the beam equations are not significant.

2.4 Cantilever beams with a thin dielectric material

In conductive SPM probes intended to be used in low noise electrical measurements in liquid environment, the conducting layer in the whole probe structure except at the tip and at the contact pad area should be covered with a dielectric material to minimize the parasitic DC conductance between the sample and the extended probe cantilever in electrical measurements in liquid environment. Although it has a clear advantage in terms of electrical isolation of the cantilever from the surrounding environment, it also modifies the mechanical properties of the SPM probes which is not desirable in most cases. In this section we will study the mechanics of a rectangular cantilever beam whose material properties are the same as the previous cantilever beams as shown in

Table 2.4: Thickness and Material properties of an additional dielectric material on a rectangular silicon cantilever beams considered for the FEM simulation studies.

material properties of PECVD silicon nitride	
Young's Modulus (E)	160GPa
Mass density (ρ_m)	$2500 kg/m^3$
Poisson's ratio (ν)	0.253
Thickness (h)	400nm

the table 2.1 with an additional dielectric material covering the whole cantilever. The material properties and the thickness of the additional dielectric material is shown in the table 2.4.

In order to determine the static and dynamic responses of a combined cantilever beam, it is important to consider the cantilever beam made of an imaginary material with a combined Young's modulus (E_c), combined density ρ_c, combined height h_c and the combined Poisson's ratio ϑ_c given by the expressions [10],

$$E_c = \frac{h_1 E_1 + h_2 E_2}{h_1 + h_2}, \tag{2.4.1}$$

$$\rho_c = \frac{\rho_1 h_1 + \rho_2 h_2}{h_1 + A_2}, \tag{2.4.2}$$

$$h_c = h_1 + h_2, \tag{2.4.3}$$

and

$$\vartheta_c = \frac{E_c h_c}{\sum_i \frac{E_i h_i}{\vartheta_i}}, \tag{2.4.4}$$

where h_1, E_1, ρ_1, and ϑ_1 are the height, Young's modulus, mass density and Poisson's ratio of the crystalline silicon beam, respectively and h_2, E_2, ρ_2 and ϑ_2 are the thickness, Young's modulus, mass density and Poisson's ration of the additional

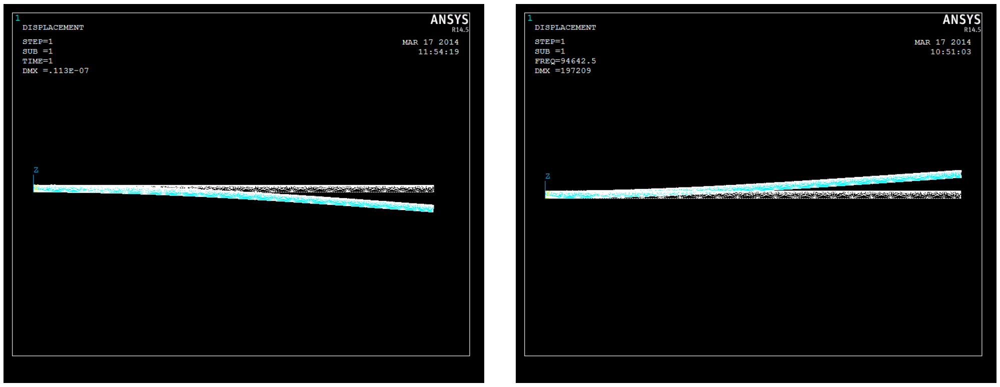

Figure 2.7: The static response under 100nN normal loading (left) and the fundamental resonance frequency (right)of $L3$ with the additional 0.4 μm PECVD grown nitride layer.

dielectric material (PECVD grown silicon nitride layer). Therefore, by using the combined Young's modulus, the combined mass density, the combined thickness and the combined Poisson's ration values in equations 2.2.7, 2.2.10-2.2.12, one can get the force constant and modal solutions of the combined cantilever beams. The point here is to convert the combined cantilever beam to a simple rectangular cantilever beam of imaginary material with Young's modulus E_c, mass density ρ_c, thickness h_c and Poisson's ration ϑ_c shown above.

Here we will present FEM simulation result of a combined cantilever beam discussed above. The material properties [11] and thickness of the dielectric material used are shown in the table 2.4. Figures 2.7 and 2.8 shows the static and the fundamental modal solutions of the $L3$ and $L9$ beams with the additional dielectric material, respectively. And table 2.5 shows the force constant and fundamental resonance frequency of $L3$ and $L9$ cantilever beams with and without the additional dielectric material, obtained using the FEM simulation.

As it can be seen in the table 2.5, the additional 400nm thick PECVD grown silicon

Figure 2.8: The static response under 100nN normal loading (left) and the fundamental resonance frequency (right)of $L9$ with the additional 0.4 μm PECVD grown nitride layer.

Table 2.5: The force constant $k(N/m)$ and fundamental resonance frequency f_0 (kHz) of the $L3$ and $L9$ rectangular crystalline silicon cantilever beams with and without the additional dielectric material obtained using the FEM simulation.

Cantilever beams	PECVD Si3N4 thickness in μm	k(N/m)	f_0 (kHz)
L3	0	6.623	86.448
L3	0.4um	8.85	94.643
L9	0	0.201	16.740
L9	0.4um	0.348	20.070

nitride thin film modifies the force constant and fundamental resonance frequencies of the crystalline silicon cantilever beams. Depending on ones intended application of the cantilever beams, these modifications would be big and undesirable. We have taken into considerations the modifications to the force constant and fundamental resonance frequencies of cantilever beams due to the additional PECVD grown silicon nitride thin film in designing the DC and AC probes that will be discussed in the next chapter.

Bibliography

[1] L.M. Roth. *Understanding architecture : its elements, history, and meaning.* New York, NY: Icon Editions, 1993, P.542.

[2] Luis Guillermo Villanueva Torrijo. *Development of cantilevers for biomolecular measurements*. PhD thesis, Universitat Autonoma de Barcelona, December 2006.

[3] Bioelectronic olfactory neuron device (BOND) project of the 7th Framework Programme of the European Union (NMP4-SL-2009-228685). ***www.bondproject.org***.

[4] Bharat Bhushan, editor. *Springer Handbook of Nanotechnology*, chapter 2, pages 97–98. Springer, University of Warwick, United Kingdom, 2004.

[5] E. J. Hearn. *Mechanics of Materials 1*, volume 1, chapter 2, pages 97–98. Butterworth-Heinemann, University of Warwick, United Kingdom, third edition, 1977.

[6] T. R. Albrecht, P. Grtter, D. Horne, and D. Rugar. Frequency modulation detection using high-q cantilevers for enhanced force microscope sensitivity. *Journal of Applied Physics*, 69(2):668–673, 1991.

[7] M. V. Salapaka, H. S. Bergh, J. Lai, A. Majumdar, and E. McFarland. Multimode noise analysis of cantilevers for scanning probe microscopy. *Journal of Applied Physics*, 81:2480–2487, March 1997.

[8] H.-J. Butt and M. Jaschke. Calculation of thermal noise in atomic force microscopy. *Nanotechnology*, 6:1–7, January 1995.

[9] Erdogan Madenci and Ibrahim Guven. *The Finite Element Method and Applications in Engineering Using ANSYS*. Springer, The University of Arizona, 2006.

[10] E. J. Hearn. *Mechanics of Materials 1*, volume 1, chapter 2, pages 27–40. Butterworth-Heinemann, University of Warwick, United Kingdom, third edition, 1977.

[11] MIT Material Properties Database. **www.mit.edu**.

Chapter 3

Design and Fabrication of Insulated Conductive Scanning Probe Microscopy (C-SPM) Probes

3.1 Introduction

As discussed in chapter 1, a number of techniques based on Scanning Probe Microscopy (SPM) have evolved as fundamental tools in biology and nanobiotechnology [1]. Specifically, electrical SPM characterization techniques such as scanning electrochemical microscopy (SCEM) [2], impedance imaging-spectroscopy and electrostatic force microscopy (EFM) [3] should allow the study of the behavior of biomolecules at the nanoscale.

With the objective of characterizing olfactory receptor proteins for the development of olfactory biosensors [4] as discussed in section 1.4, we have developed conductive SPM probes for impedance imaging and spectroscopy in liquid environment. This requires the use of conductive probes that minimize the parasitic impedance associated with the extended cantilever and the biological sample under investigation.

This can be achieved by minimizing both the parasitic capacitance and the parasitic DC current between the extended probe cantilever and the sample. The parasitic DC current can be minimized by insulating the SPM probe with a dielectric material except at the tip and the electrical contact pad. The parasitic capacitance can be minimized by engineering the geometry of the conducting layer. Kranz et al. [2] fabricated conducting and insulated AFM probes for SECM, but required serial processing using focused ion beam. Akiyama et al. [5] fabricated silicon nitride probes bonded to pyrex handling chips. Dobson et al. [6] fabricated SECM-AFM probes using electron beam lithography to define the electrode. But to date commercial conductive SPM probes are not suitable for electrical studies in liquid environment due to the lack of electrical insulation which is the key to minimize the parasitic DC current.

As described below, our probes have been fabricated in silicon-on-insulator (SOI) substrates as cantilevers with sharp tetrahedral tips [7] at their free end (Figure 3.1). We prepared separate designs for DC probes (to be used for DC electrical measurement of samples in contact mode) and AC probes (to be used to measure the AC response of the sample in dynamic mode). Cantilever lengths range from 200 to $400\mu m$, widths from 30 to $40\mu m$ and the thickness is 2 or $4\mu m$. These cantilever dimensions are chosen so that the probes will satisfy the specification as required by the BOND project, as confirmed by the theoretical and FEM modeling studies of cantilever beams presented in chapter 2. The width of the conducting layer in the cantilevers ranges from 10 to $20\mu m$.

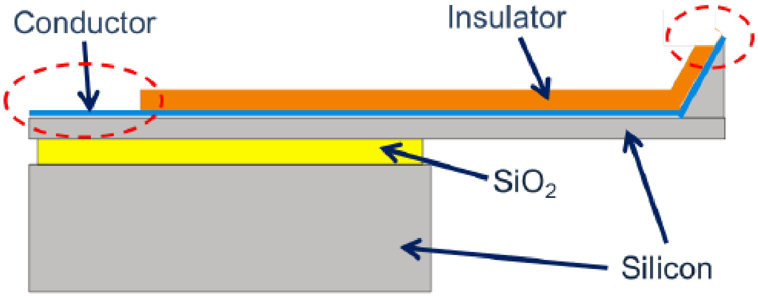

Figure 3.1: Schematic structure of the fabricated probes. Two types of probes with either a conducting thin film or a doped silicon layer have been developed.

3.2 Overview of this chapter

In this chapter, the technology developed at IMB-CNM for the fabrication of DC and AC probes will be presented.

In section 3.3, the design and technology for the fabrication of tetrahedral tips along with results and problems encountered will be presented. Next, the design and technology for the fabrication of prototype AC and DC probes will be discussed in section 3.4. In section 3.5, the various test runs performed to solve the problems encountered in the tetrahedral tips and prototype probes fabrication processes will be discussed in detail. The improved photo mask set for the fabrication of AC and DC probes will also be presented in section 3.5. Then, the fabrication of AC and DC probes with optimized process and design parameters will be discussed in section 3.6. An alternative technology test run will be presented in section 3.7. Later an overview of alternative technology for the fabrication of AC probes will be presented in the section 3.8. Finally, a block diagram summary of all the runs performed in developing the technology for the fabrication of AC and DC probes will be presented in the last section (section 3.9).

3.3 Tetrahedral tip fabrication process: Run 5571

As the geometry and shape of the tip is an essential part of the SPM probes, our first task in the fabrication of the insulated C-SPM probes was to design the photo mask (CNM510) and to test the tip definition technologies available at IMB-CNM clean room facility. Shown in the figure 3.2 is the schematic diagram of a tip mask with the geometrical parameters (a-c) being the width of the sides indicated, *e* being angle in degree and *d* being the perpendicular distance from the corner at *e* to the side *c*. We used different values of these parameters in designing the tip mask, typically we used 37°, 54° and 90° for the angle *e*. And shown in the figure 3.3 is the CNM510 photo mask at different level of detail. We preferred tetrahedral tips over pyramidal ones as tetrahedral tips which are formed by the connection of three planes are in principle sharper than pyramidal ones which are formed by the connection of four or more planes. Next we will describe the process for the fabrication of a sharp tetrahedral silicon tips that could be integrated to the free end of silicon cantilever beams.

The starting material that we used for this test run was a standard (100) oriented silicon technology wafers. Figure 3.4 is the schematic diagram of the fabrication process sequence for the fabrication of sharp tetrahedral tips. 370Å thin thermal oxide plus 3000Å low pressure chemical vapor deposited (LPCVD) nitride layers are grown on both sides of the wafers. The thin thermal oxide is needed for better adhesion of the LPCVD silicon nitride layer which will later be used as an oxidation mask. Later $0.1\mu m$ thick aluminum and $2\mu m$ thick photoresist layers are deposited on the device layer of the wafers. The photoresist is patterned with a photolithographic step using the CNM510 mask to open a window on the aluminum layer having the same shape as the tip mask, figure 3.2. The exposed aluminum and the subsequently exposed

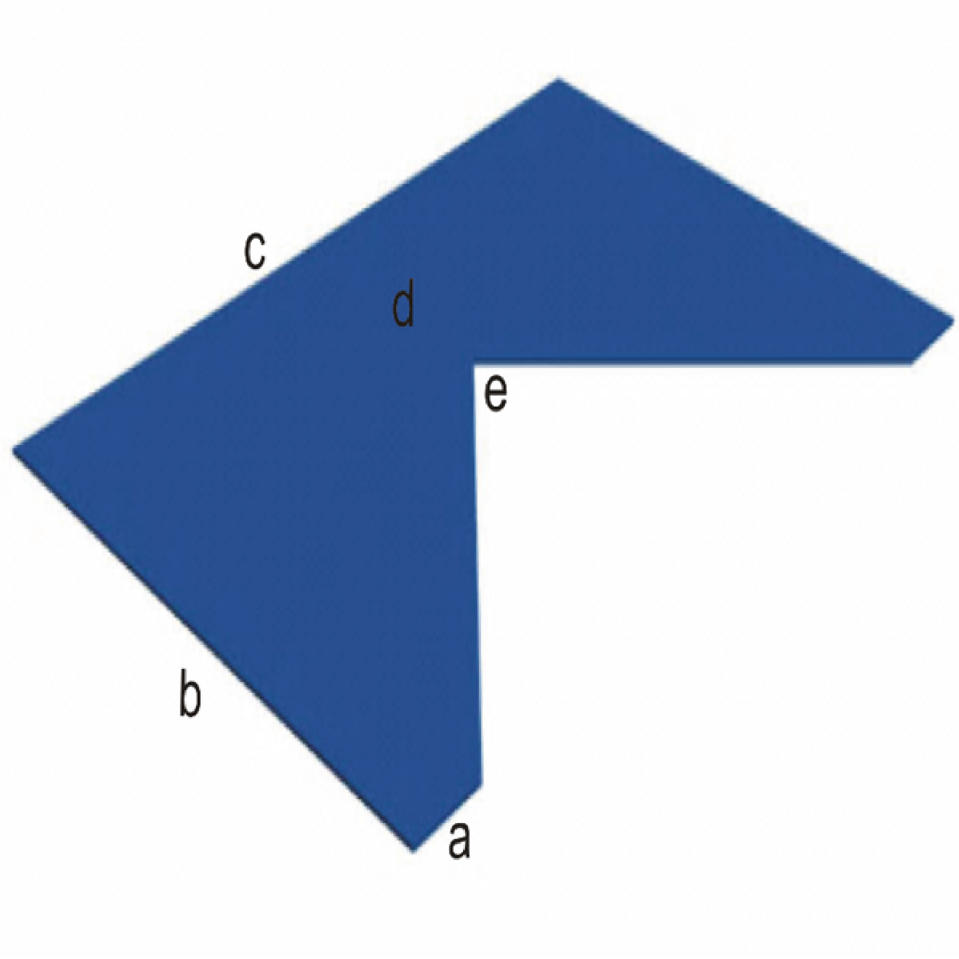

Figure 3.2: Schematic diagram of tetrahedral tip mask with a-c being the lengths of the sides indicated, e being the angle and d being the perpendicular distance between the corner at e and the side c.

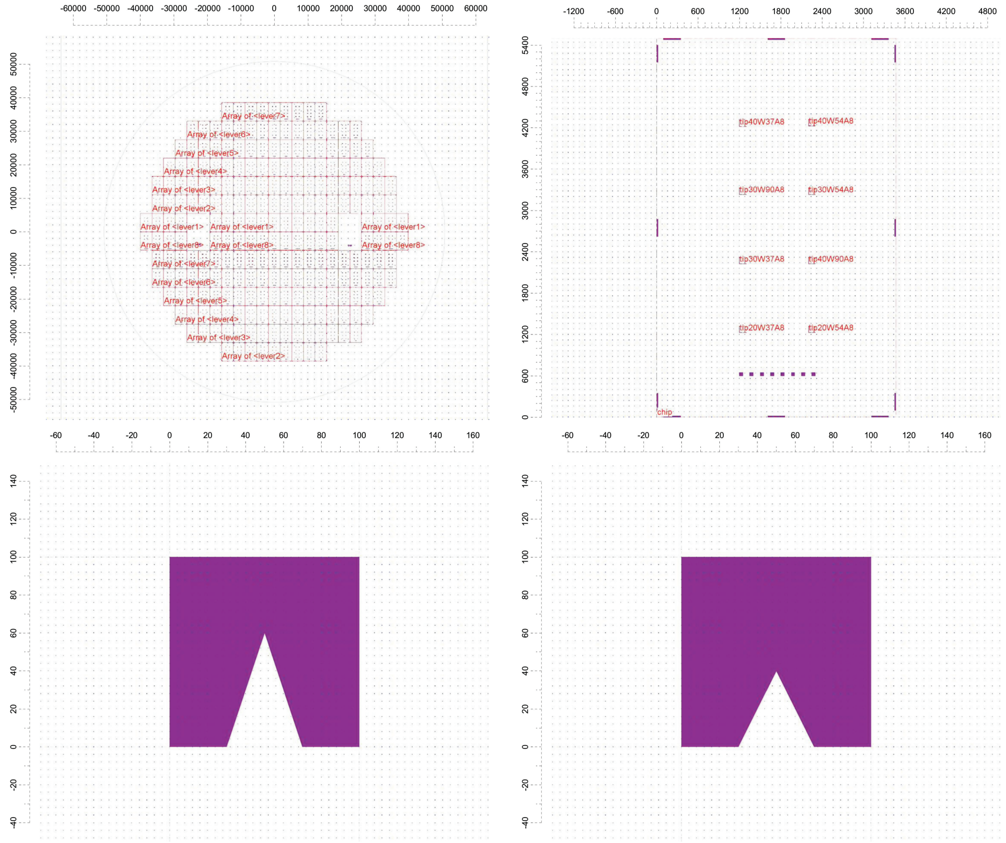

Figure 3.3: CNM510 tip mask. Top: whole wafer level mask and single chip. Bottom: Two tip masks with different geometrical parameters

Table 3.1: P601DEEP recipe of DRIE of silicon process parameters

Gases	sccm	modes	Order	Time	% valve opening	RF Source	RF substrate	T ($^\circ C$)
SF_6	300	pulse	2	7 s	18	1800 W	13 W	20
C_4F_8	200	pulse	1	3.5 s	18	1800 W	13 W	20

nitride and oxide layers are etched with Reactive Ion Etching (RIE) processes. At this stage of the fabrication process, the whole wafer is covered with photoresist except the tip area where the exposed layer is silicon. Then $15\mu m$ thick silicon is etched with P601DEEP condition of Deep Reactive Ion Etching (DRIE) of silicon to define the two vertical side walls of the tetrahedral tips (figure 3.4 B). The process parameters of the P601DEEP recipe of DRIE of silicon is shown in table 3.1. After the aluminum layer is removed in wet etching and the wafers are cleaned in piranha solution, 4000Å thick wet thermal oxide, which will be used as a mask for the subsequent Tetramethylammonium hydroxide (TMAH) etching step, is grown on the exposed silicon: on the vertical walls of the tetrahedral tips and in the window area (figure 3.4 C). Later the 3000Å nitride and 370Å thin thermal oxide layers grown at the start of the fabrication process are removed in wet etching and the wafers are etched in a 25% TMAH at $80^\circ C$ etching solution to define the third plane of the tetrahedral tips, (111) plane. Finally the 4000Å thermal oxide is removed from the vertical walls of the tetrahedral tips and from the window using 6:1 volume ratio of 40% NH_4F in water to 49% HF in water etching solution (SiO-etch), figure 3.4 D.

Shown in the figure 3.5 is Scanning Electron Microscopy (SEM) micrographs of tetrahedral tips taken at different stages of the fabrication process. The SEM micrograph in figure 3.5 (a) was taken after the thin thermal oxide and the 3000Å silicon nitride layers had been removed in wet etching. Whereas the SEM image in figure

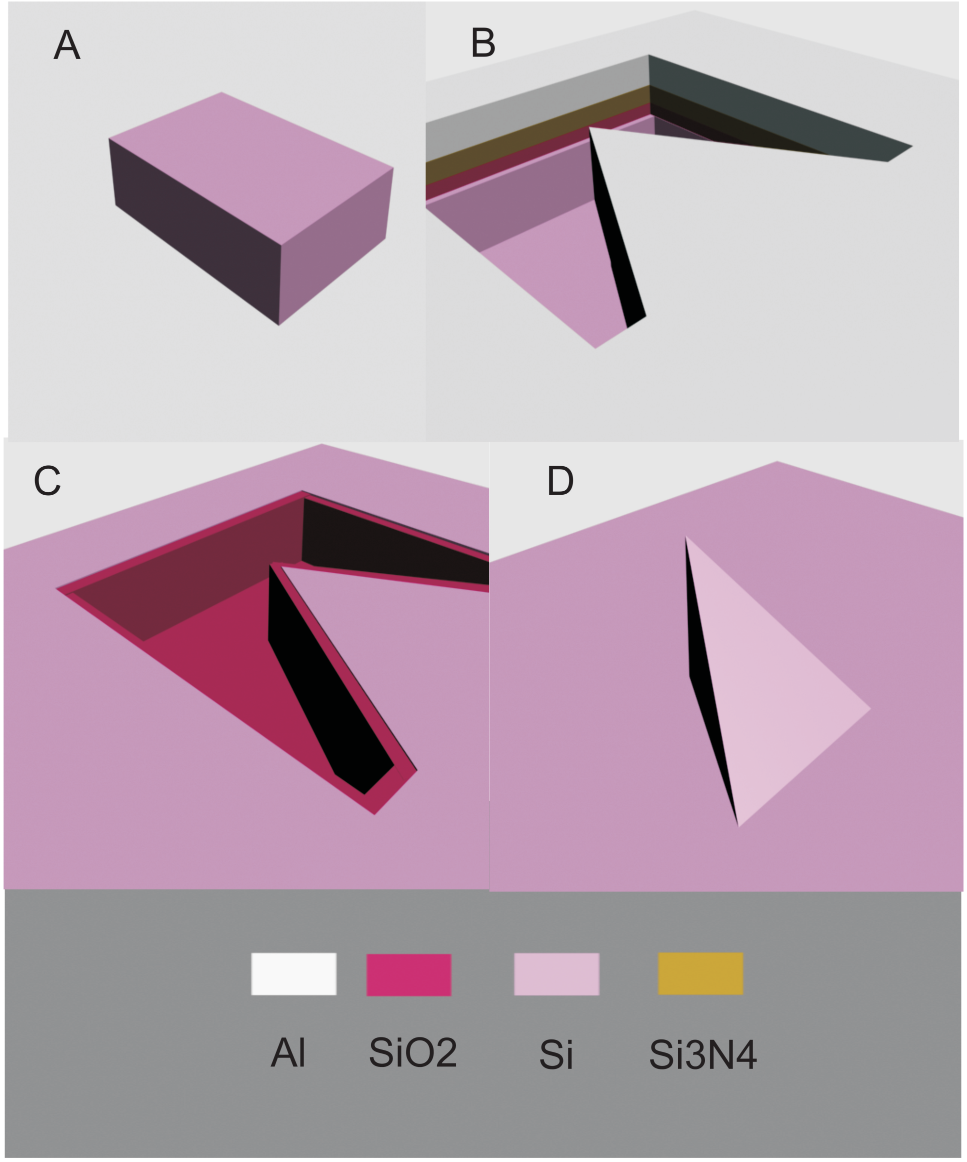

Figure 3.4: Schematic diagram of tetrahedral tip fabrication process sequence

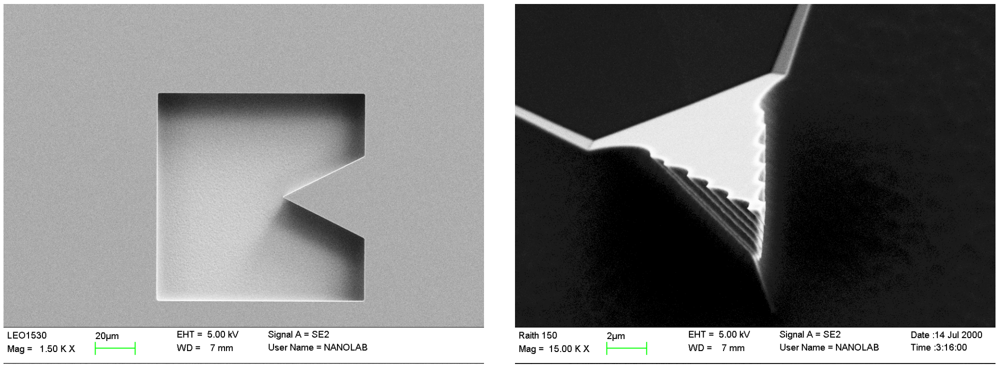

Figure 3.5: SEM micrographs of tetrahedral tips taken after 15um deep hole was drilled on the front side of silicon with DRIE of silicon that defines the two vertical side walls of the tetrahedral tips (left) and taken after the third plane (111)of the tetrahedral tips was formed by anisotropic wet etching process with TMAH (right).

3.5 (b) was taken at the end of the fabrication process. As it can be clearly seen especially in figure 3.5 (b) there is a scalloping defect in the tips. This scalloping defect arises from the DRIE of silicon process. Except for the appearance of the scalloping defect, we obtained tetrahedral tips in all combinations of the geometrical parameters we used in designing the tip mask. But due to this scalloping effect we couldn't clearly see which combinations of the geometrical parameters of the tip mask resulted in sharper tetrahedral tips.

3.4 Prototype C-SPM probes fabrication: Run 5918 and 5919

After we have checked the possibility of defining tetrahedral tips with the technologies in the IMB-CNM clean room facility, we proceeded designing the photo mask sets for the fabrication of insulated C-SPM probes (cantilevers integrated with sharp tetrahedral tips at their free end). We designed two separate photo mask sets namely DC1

Table 3.2: The design parameters of the DC1 mask set

Beams	Length (μm)	Width (μm)	Conducting layer width (μm)	Angle
L1	400	40	10	37
L2	400	40	20	37
L3	400	30	10	37
L4	400	30	20	37
L5	300	40	10	37
L6	300	40	20	37
L7	300	30	10	37
L8	300	30	20	37

and AC1 photo mask sets for the fabrication of DC and AC probes, respectively. The design parameters for these two photo mask sets are cantilever length and width, conducting layer width in the cantilever and the angle e in the tip mask (figure 3.2). The values of the design parameters of the DC1 and AC1 photo mask sets are as shown in the tables 3.2 and 3.3, respectively. The layout of the DC1 and AC1 mask sets are shown in the figures 3.6 and 3.8, respectively at different level of details. Besides cantilever dimensions, the other major difference between the DC and AC probes was on the choice of the tip material. In the DC probes the conducting layer was realized with high dose boron implantation plus annealing. Whereas the conducting layer in the AC probes was realized by physical vapor deposition of Cr + Au thin films and patterned with a lift-off process. These choices of tip materials satisfies the electro-chemical neutrality and Bio-compatibility properties as the probes were intended for topography and impedance spectroscopy measurement of Biological samples in their physiological environment.

100 mm diameter (100) oriented n-type Silicon on Insulator (SOI) technology wafers with $15\mu m$ device layer, $1\mu m$ buried oxide (BOX) layer and $500\mu m$ thick bulk

Table 3.3: The design parameters of the AC1 mask set

Beams	Length (μm)	Width (μm)	Conducting layer width (μm)	Angle
L1	200	40	10	37
L2	200	40	20	37
L3	200	30	10	37
L4	200	30	20	37
L5	225	40	10	37
L6	225	40	20	37
L7	225	30	10	37
L8	225	30	20	37

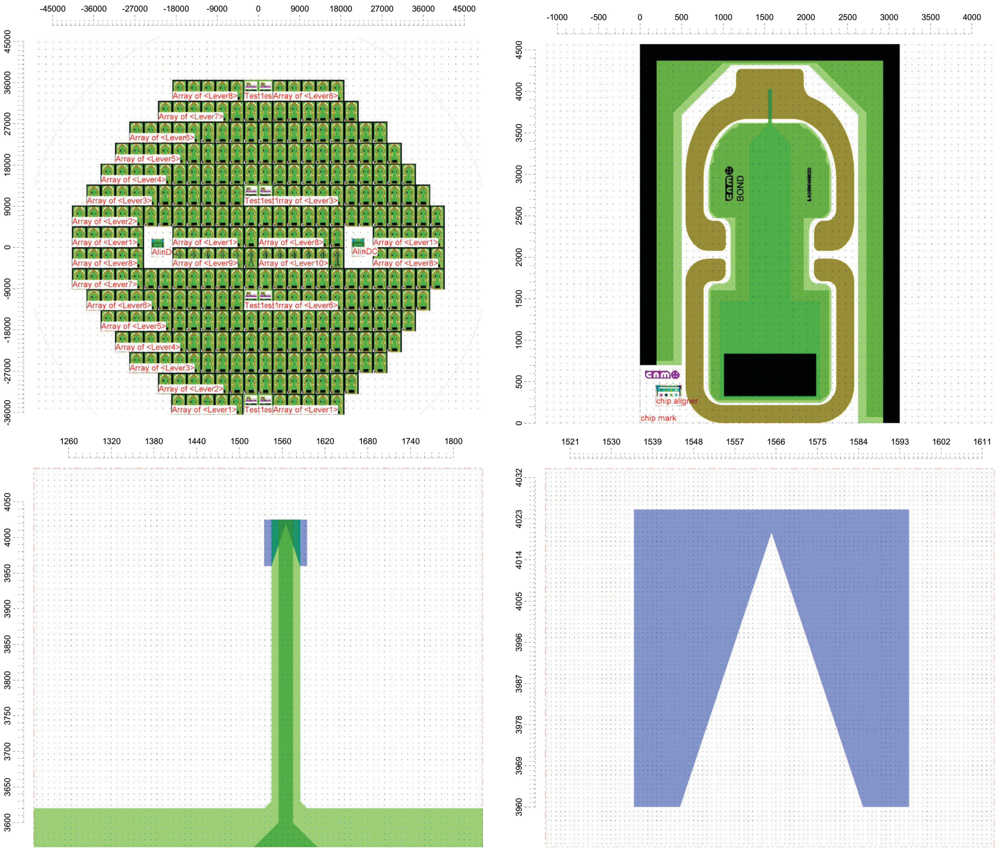

Figure 3.6: Layout of DC1 mask set at different level of detail. Top: whole wafer scale (left), a chip (right). Bottom: a probe cantilever (left) and a probe tip (right).

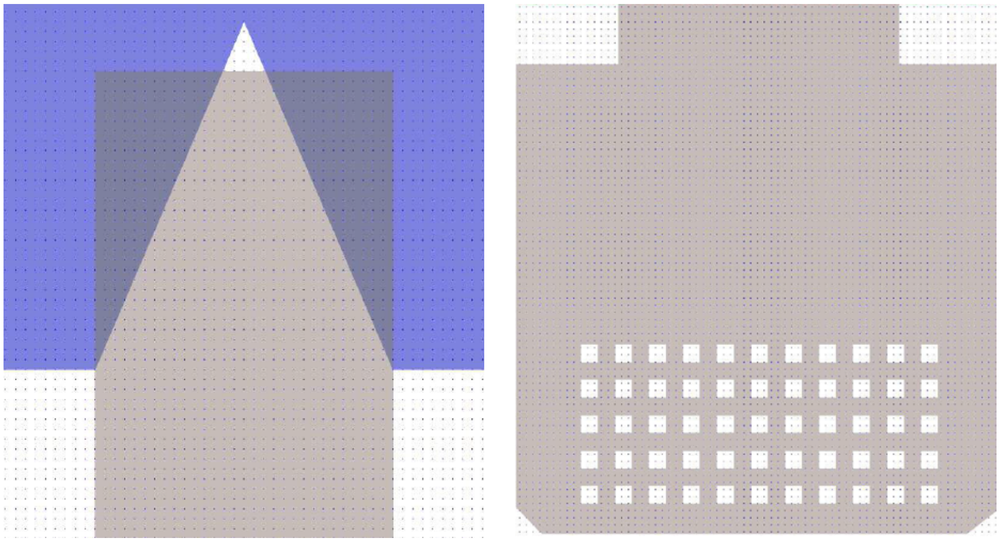

Figure 3.7: Layout of dielectric patterning level mask (gray) for the fabrication of prototype DC probes. Left: near the tip together with the tip mask (blue). Right: near the contact pad area.

silicon were used as a starting material for these runs. Figure 3.10 is the schematics of the process sequence that we followed for fabricating the probes. The fabrication process begins by fabricating the tips by opening a hole in the Si device layer with the NANO1 recipe of DRIE of silicon process, whose process parameters are shown in table 3.4, using the BOX layer as an etch stop. The top surface is covered by a thin thermal oxide,100 nm thick LPCVD silicon nitride plus 100nm Al (figure 3.10a). This defines the two vertical planes of the tetrahedral tips. The Al layer is removed in wet etching and the wafers undergo a wet thermal oxidation process to grow a 400 nm thermal oxide on the exposed silicon walls using the silicon nitride layer as an oxidation mask. The silicon nitride and the thin thermal oxide layers are removed using wet etching processes and the wafers are etched in a 25% TMAH solution at 80°C with time as a control parameter to define the third (111) plane of the tetrahedral tips and the thickness of the cantilevers. This wet etching process is

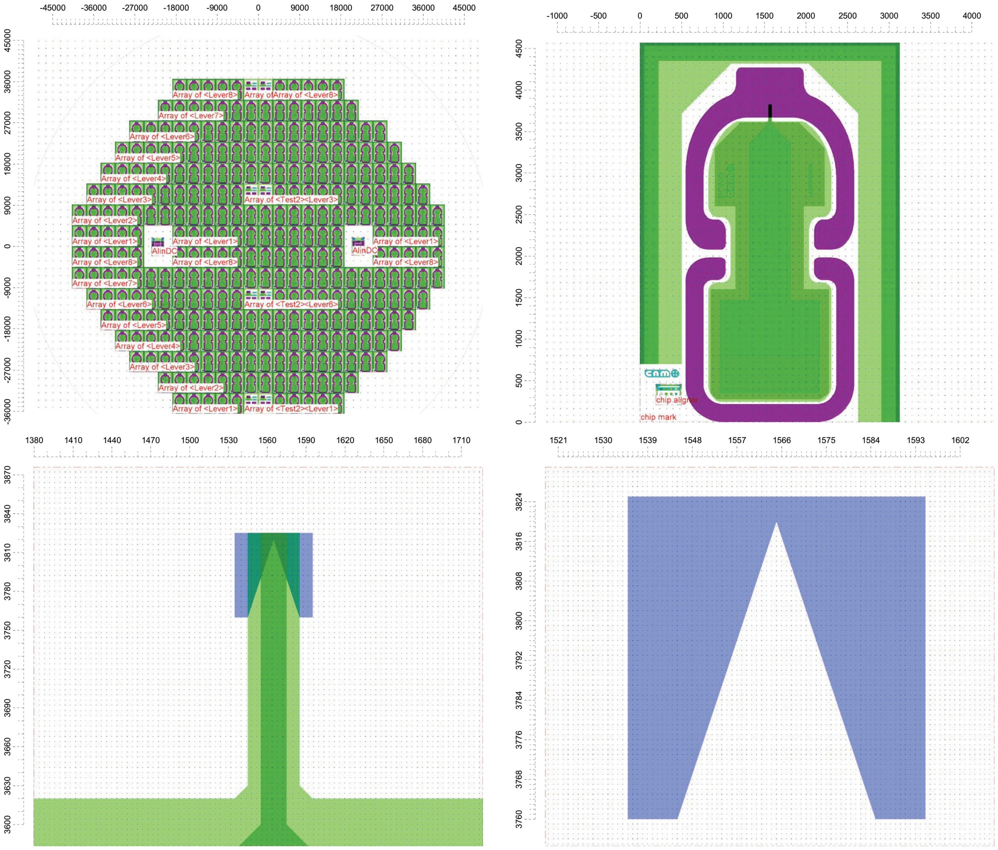

Figure 3.8: Layout of AC1 mask set at different level of detail. Top: whole wafer scale (left), a chip (right). Bottom: a probe cantilever (left) and a probe tip (right).

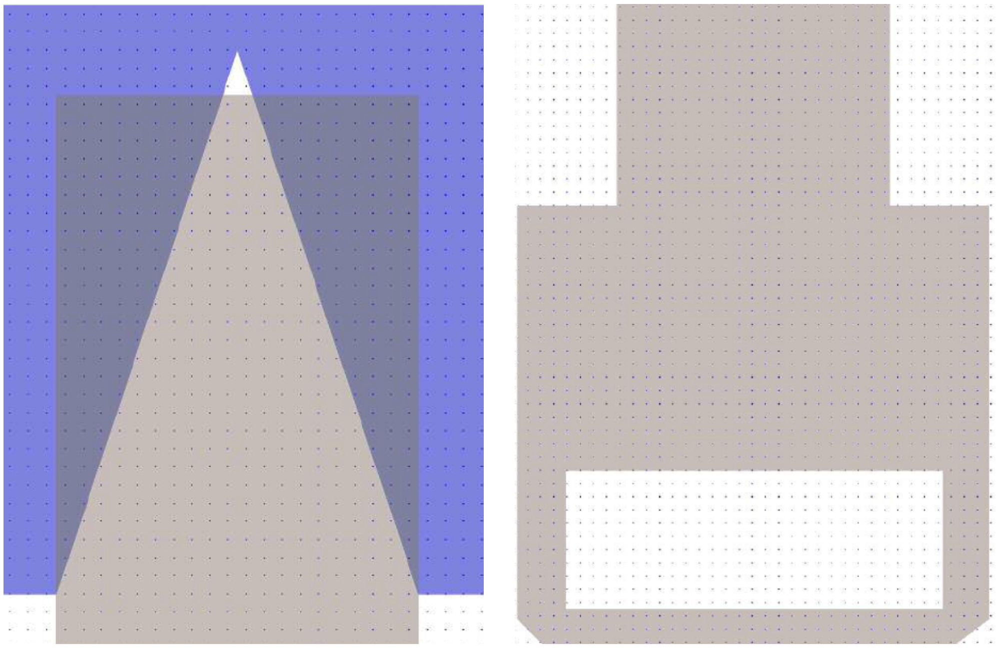

Figure 3.9: Layout of dielectric patterning level mask (gray) for the fabrication of prototype AC probes. Left: near the tip together with the tip mask (blue). Right: near the contact pad area.

terminated as soon as the remaining silicon layer in the wafers matches the required cantilevers thickness ($2\mu m$ for DC probes and $4\mu m$ for AC probes). The cantilever and substrate shapes are defined with a photolithographic step using $24\mu m$ thick photoresist and silicon etching using DRIE (figure 3.10b). later the 400nm thermal oxide grown on the vertical side walls of the tetrahedral tips is removed using wet etching. Then a conducting layer is realized in the probes (figure 3.10c). In the wafers for the AC probes 30 nm Cr + 100 nm Au are deposited using physical vapor deposition and patterned with a lift-off process. In the wafers for the DC probes, the conducting layer is realized with high-dose boron ion implantation (Dose=5×10^{15} ions/cm^2 and Energy=30keV) plus annealing at 950 $^{\circ}C$ for 20min in a conventional furnace annealing equipment. Later a 400 nm thick silicon nitride layer is deposited using plasma enhanced chemical vapor deposition (PECVD) and patterned using a photolithographic step, which is performed using the dielectric patterning photo mask whose layout is as shown in figure 3.7 for the DC probes and figure 3.9 for AC probes, and RIE process so that the whole probe is insulated except at the tips and electrical contact pads (figure 3.10d). For the DC probes, a $1\mu m$ thick aluminum layer is sputter deposited and patterned to make electrical contact to the high boron doped conducting layer in the pad area. The substrate is etched from the backside by DRIE process [8] using a $1\mu m$ thick Al mask layer and using the BOX as an etch stop. Finally the cantilevers are released by 49% HF vapor etching of the BOX. The 49% HF vapor etching solution is prepared by half-filling a teflon beaker of 90mm in diameter with 49% HF acid, cover with a teflon covering plate and then waiting for about 30min for the system to stabilize in the ambient pressure and temperature before starting the etching processes. Then the BOX is etched by placing the wafers

Table 3.4: NANO1 recipe of DRIE of silicon process parameters

gases	sccm	modes	order	time	% valve opening	RF source	RF substrate	T ($^\circ C$)
SF_6	150	pulse	2	1 sec.	25	1500 W	13 W	20
C_4F_8	100	pulse	1	2.5 sec.	25	1500 W	13 W	20

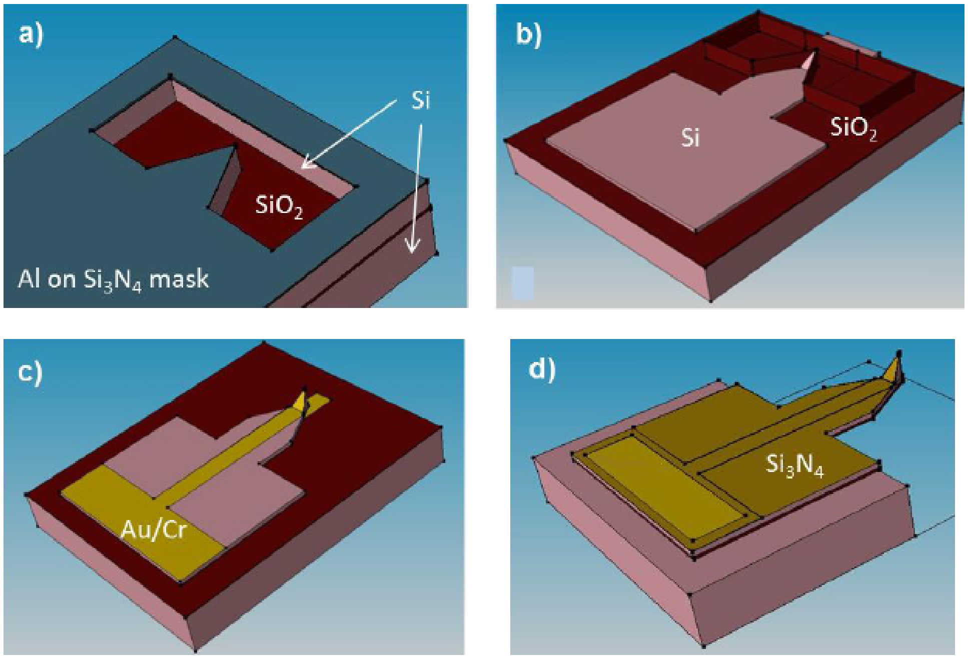

Figure 3.10: Schematic diagram for the fabrication of insulated conductive SPM probes.

on the teflon beaker with the backside of the wafers facing the vapor. During the backside processing steps, the device layer of the wafers is covered with a $24\mu m$ thick resist layer that protects the tips from physical damage and give mechanical support to the fragile cantilevers.

Figures 3.11 and 3.12 are the SEM micrographs and optical microscope images, respectively of the DC and AC probes taken at the end of the fabrication processes. As it could be clearly seen in the bottom right of figure 3.11, there is scalloping defect in the AC probes' tip similar to the first test run we discussed in the previous section.

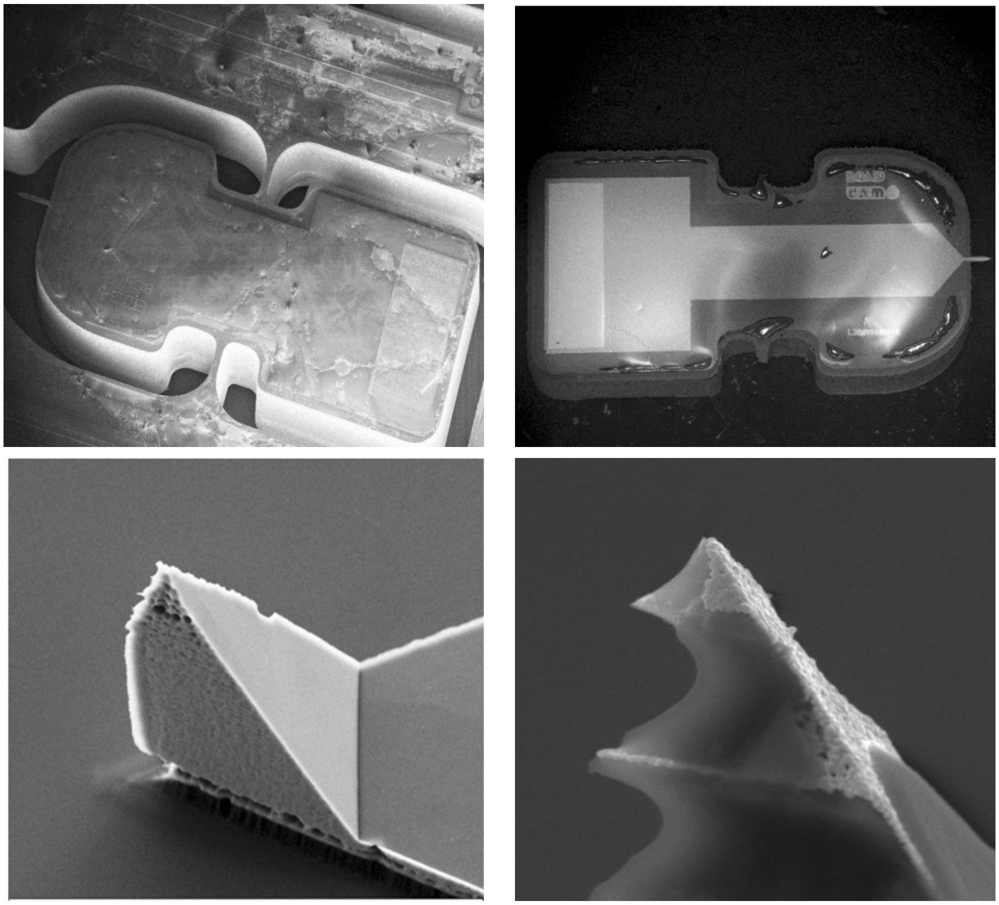

Figure 3.11: SEM micrographs of the prototype probes. Top: whole probe structure of DC (left) and AC (right) probes. Bottom: Magnified tip of a DC (left) and an AC (right) probes.

This is because the hole in the device silicon, that defines the two vertical planes of the tetrahedral tips, was performed with the P601DEEP recipe of the DRIE of silicon instead of NANO1 by mistake. Whereas in the bottom left of the same figure, which is the magnified SEM micrograph of a tetrahedral tip of a DC probe, the hole was opened with NANO1 recipe. In the DC probes' tip, the scalloping defect have been eliminated but at the expense of the appearance of another defect, undercut at the tip. Another critical problem that we observed during the fabrication of the prototype probes was the damage on the PECVD nitride layer in the front side of the wafers, which is intended to be used as an electrical insulation of the conducting layer in the probes, during the BOX etching with 49% HF vapor from the backside of the wafers. In the case of the DC probes, we had processed the wafers in the HF vapor for 5min and we observed that the HF vapor had piled up the thick resist layer in the front side of the wafers and damaged completely the nitride layer, figure 3.12 (left). To avoid similar damage, we exposed the wafers for the AC probes for only 2min and 30s. Still in this short time the HF vapor had diffused through the thick resist layer and damaged part of the nitride layer in the cantilevers, figure 3.12 (right).

3.5 Further tests performed to extract optimal process parameters

3.5.1 Test run 6246

This process run was designed to solve the problems encountered in the previous technology process runs, scalloping, tip undercut and PECVD silicon nitride electrical insulation layer damage. In the first part of this run we tested the remaining two tip

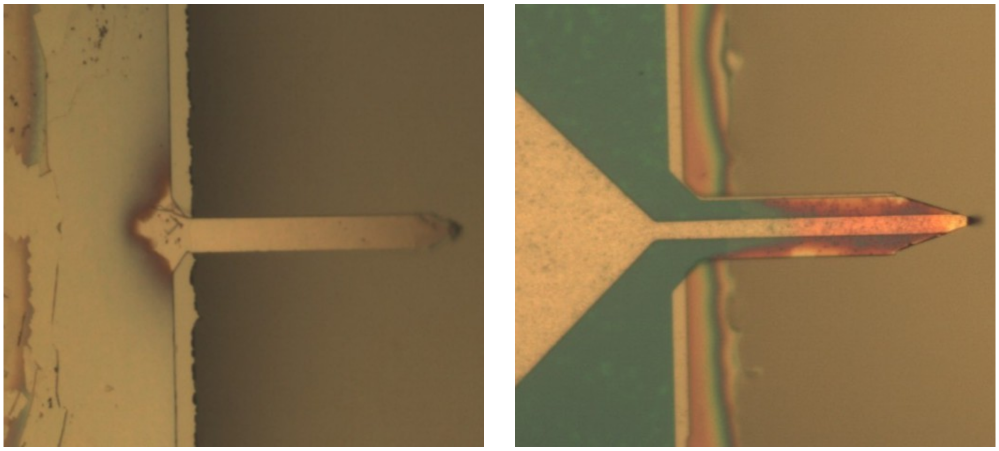

Figure 3.12: Optical microscope images of a prototype DC (left) and AC (right) probes taken at the end of the fabrication process.

defining DRIE of silicon technologies namely 3G and P601POLI recipes available at IMB-CNM clean room facility. The second part of this run was intended to test the resistant to HF vapor attack and process compatibility of Atomic Layer Deposited (ALD)Al_2O_3 and parylene-c dielectric materials.

(100) oriented standard technology wafers were used as a starting material to test the tetrahedral tip defining technologies. We followed similar processing steps with the tetrahedral tip definition steps of the prototype runs described in the previous subsection. Here we used 3G and P601POLI DRIE of silicon recipes to make the hole on the front side of the wafers, that defined the two vertical side walls of the tetrahedral tips. The process parameters of these two DRIE of silicon technologies are as shown in table 3.5.

Figure 3.13 is SEM micrographs of the tetrahedral tips, where the hole on the front side of the wafers that defined the two vertical side walls of the tetrahedral tips was opened with the 3G (left) and P601POLI (right) recipes. The 3G DRIE of silicon process gives much better tetrahedral tips than all the other DRIE conditions

Table 3.5: P601POLI and 3G recipes of DRIE of silicon process parameters

Process	SF_6 flux (sccm)	C_4F_8 flux (sccm)	O_2 flux (sccm)	RF Source power	RF substrate power	Pressure
P601POLI	35	45	-	800 W	5 W	2 Pa
3G	300	300	100	1500 W	80 W	5-8 Pa

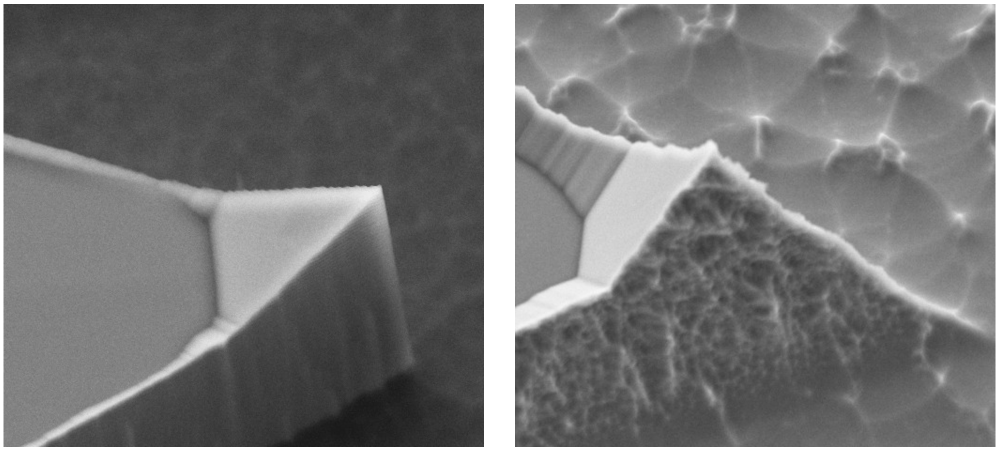

Figure 3.13: Tetrahedral tips in which the 15um thick deep hole on the device silicon, that defined the two vertical side walls of the tips, was made with 3G (left) and P601POLI (right) recipes of the DRIE of silicon.

available at IMB-CNM clean room facility. Hence, we will use 3G condition to open a hole in the device layer of wafers in the coming runs to fabricate the tetrahedral tips for the DC and AC probes.

Here we will describe the process for the dielectric test. Figure 3.14 shows the schematic of the fabrication process sequence. The starting material is an n-type (100) oriented SOI technology wafer with $2\mu m$ thick device layer, $1\mu m$ thick BOX and $500\mu m$ thick bulk silicon (figure 3.14 A). The wafers will be passed through in either one of the two process sequence options (primed or unprimed processes). In the unprimed process sequence, first 200nm thick PECVD silicon nitride is grown on the device layer of the wafers and then the cantilever and substrate shapes are defined using a photolithography, RIE and DRIE processes (figure 3.14 B). In the primed process sequence, first the cantilever and substrate shape is defined using a photolithographic step and DRIE process (figure 3.14 B') and then 30nm thick ALD Al_2O_3 is grown on the device layer of the wafers and patterned using photolithography and RIE processes (figure 3.14 C'). The substrate is etched from the backside of the wafers with DRIE using a $1\mu m$ thick Al mask layer and using the BOX as an etch stop. Finally the cantilevers are released by 49% HF vapor etching of the BOX layer (figure 3.14 C and C'). During the backside processing steps the front side of the wafers in the unprimed process are protected with $1.5\mu m$ parylene-c, which was grown Centre National de la Recherche Scientifique (CNRS) in France, plus 24um thick photoresist layers. Whereas the wafers in the primed process are protected only with a $24\mu m$ thick photoresist layer.

Figure 3.15 is the optical microscope image of wafers processed in the primed process taken after the Al_2O_3 layer was patterned with RIE process. The BOX layer was cracked due to the induced stress by the Al_2O_3 layer. As the same cracking defect in the BOX layer was observed in all the wafers processed in the primed process, the process was terminated before the wafers were passed through the remaining processing steps. In the case of the unprimed process, after a 200 $°C$ thermal treatment just before a photolithographic step on the backside of the wafers to pattern the Al mask, we observed too many bubbles on the Al in all the wafers. We removed the Al and redeposit new Al layer hopping that the bubbles will disappear. But the same sorts of bubbles were observed on the newly deposited Al just before any thermal treatment step was performed. So, the wafers in this process were also terminated before passing through the remaining process steps.

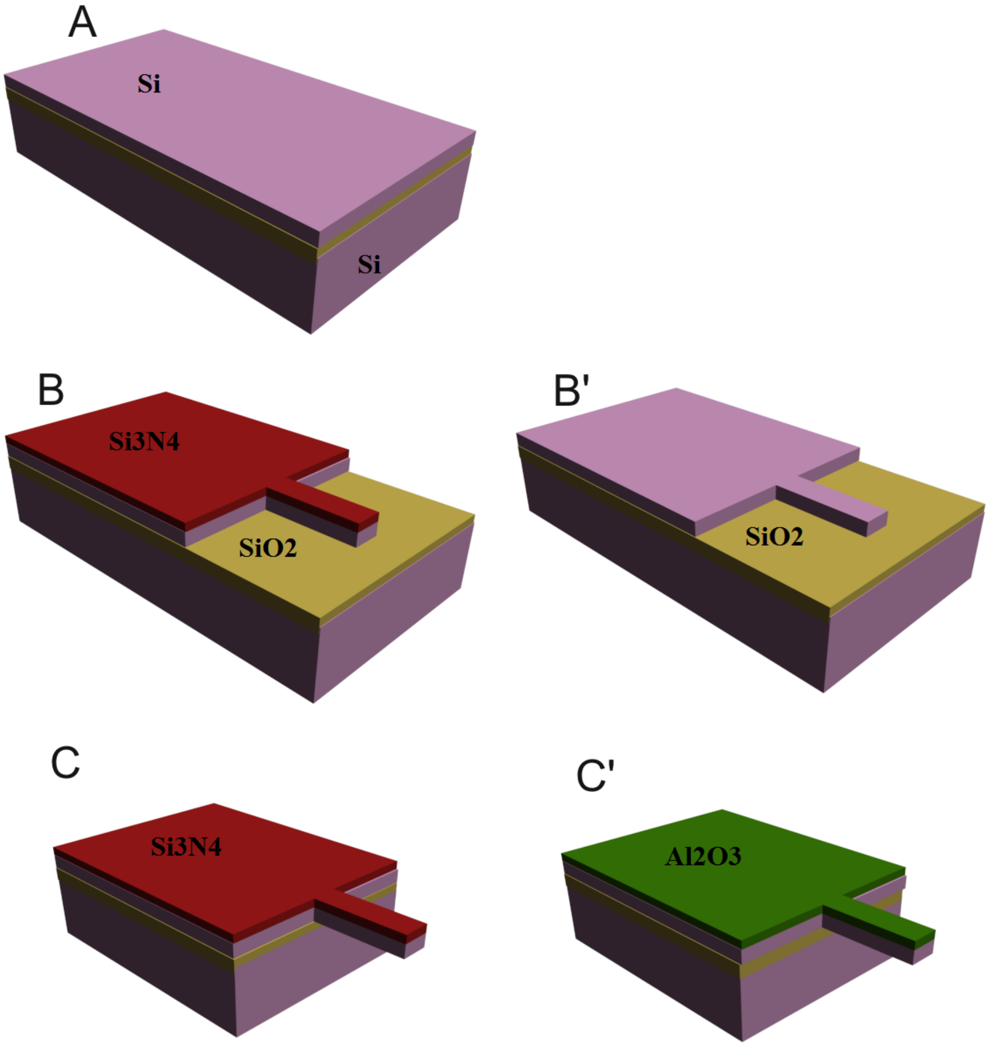

Figure 3.14: Schematics of a silicon cantilever fabrication with an additional thin dielectric material covering the whole cantilever and substrate assembly.

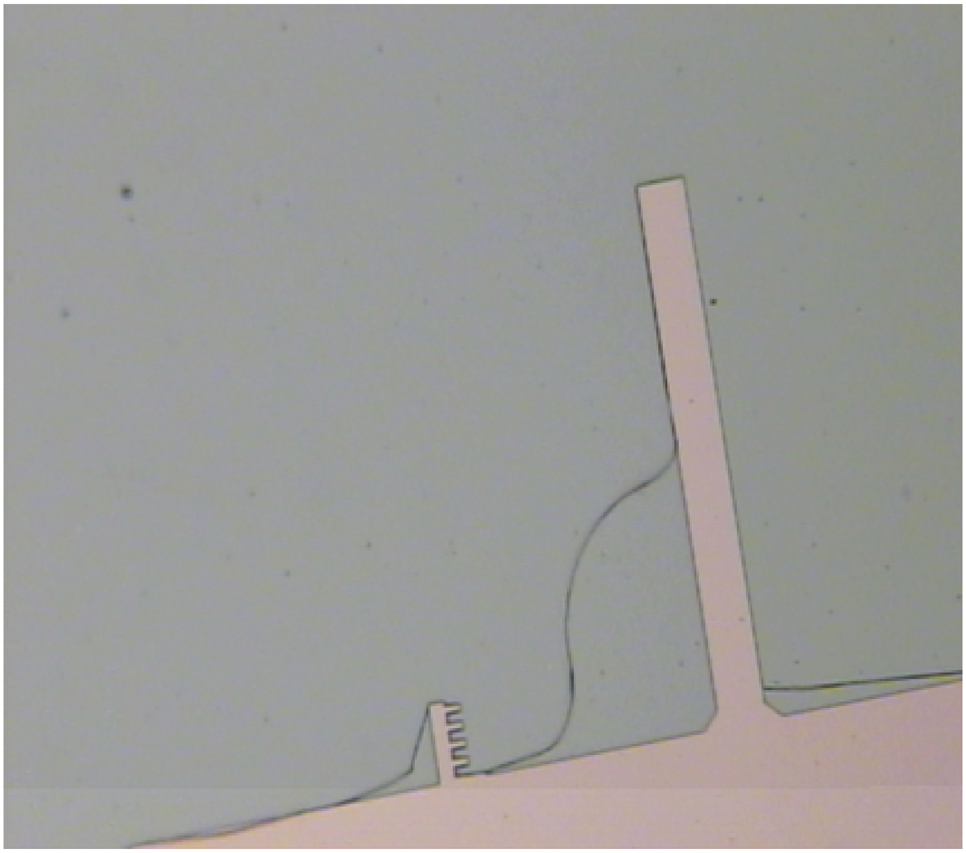

Figure 3.15: Optical microscope image of ALD grown Al_2O_3 thin film taken after it had been patterned with photolithography plus RIE processes.

3.5.2 Test Run 6341

The conducting layer in the DC prototype probes discussed before was made by high boron doping plus annealing. In these probes we were not able to make DC electrical contact with a conducting substrate. This is due to the existence of thin native oxide on the tips as the tip material is silicon. To solve this problem we proposed to use either titanium or tantalum silicide layers formed using rapid thermal processing [9–14] as a conducting layer for the DC probes as silicide layers are resistant to an oxidizing environment. This run was designed to test the possibility of forming hard and low sheet resistance titanium and tantalum silicide layers on silicon substrate that could be used as a tip material for a conductive SPM probe intended for contact mode electrical and topographic characterization of samples in liquid environment.

Standard silicon technology wafers were used as a starting material. Schematic of the fabrication process is shown in figure 3.16. The wafers are cleaned in a standard cleaning solution to remove the thin native oxide on the wafers. 100nm thick Ti or metal rich tantalum silicide (Ta_2Si) layer is sputter deposited on the device layer of the wafers (figure 3.16 B). In the case of titanium silicide formation, the wafers are passed two rapid thermal annealing (RTA) steps to form low sheet resistivity $TiSi_2$ layer. The first RTA is made at 690 $°C$ for 30s in nitrogen atmosphere that form high resistivity $TiSi_2$, C49 at the Ti-Si interface (figure 3.16 C). Then the non reacted Ti metal and TiN layer formed by the reaction of Ti with the nitrogen gas are selectively stripped with $H_2O : NH_4OH : H_2O_2 =$ 5:1:1 solution at 55 $°C$ for 10min (figure 3.16 D) [10]. The second RTA at 850 $°C$ for 10s is made to convert the high sheet resistivity titanium silicide (C49) to the low sheet resistivity one, C54 (figure 3.16 D) [14]. Whereas in the tantalum silicide (Ta_2Si) formation, the wafers

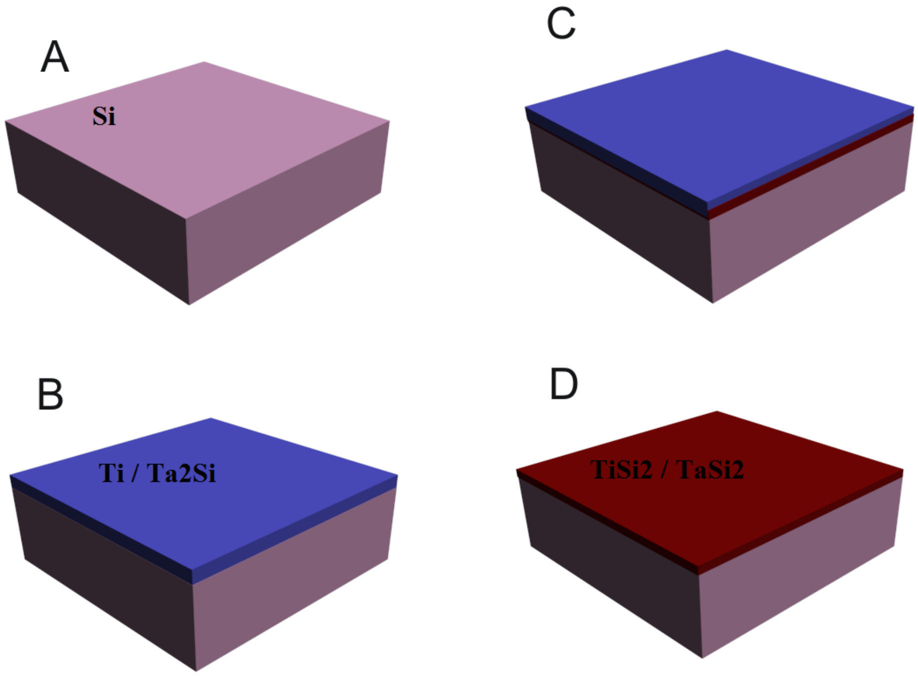

Figure 3.16: Schematics of Titanium silicide and Tantalum silicide formation on silicon wafers.

are treated with only one RTA step at 900 °C for 30s in nitrogen atmosphere to form low sheet resistivity tantalum silicide ($TaSi_2$) layer (figure 3.16 D) [13].

The four probe sheet resistance measuring equipment was employed to measure the sheet resistance at different level of the silicide fabrication process. The average sheet resistance of as-deposited titanium and metal rich tantalum silicide were measured to be 12.20264 ± 0.45951 Ω/□ and 24.45043 ± 0.45746 Ω/□, respectively. The average sheet resistance of the metal rich tantalum silicide have dropped to 3,89554 ± 0.09624 Ω/□ after the RTA step. Whereas the average sheet resistance of the titanium silicide measured after the selective stripping of the non reacted titanium metal was found to be 8.40782 ± 3.08684 Ω/□. After the second RTA step, the sheet resistance of the titanium silicide layer has dropped to 2.47069 ± 0.41506 Ω/□.

Nanoindentation technique has been employed to extract the hardness and the bulk modulus of the fabricated salicide films. The average bulk modulus and the hardness of the tantalum silicide film was found to be 222,184 ± 14,608GPa and 17,285 ± 1,487GPa, respectively. Whereas the average bulk modulus and the hardness values of the titanium silicide film was measured to be 180,341 ± 17,436GPa and 11,339 ± 1,423GPa, respectively. The hardness value of these silicide films are comparable to that of bulk silicon.

3.5.3 Run 6260 and 6283

These two runs,6260 and 6283, are designed to fabricate conductive SPM probes for DC and AC applications respectively with improved technology process parameters and photo mask designs. The photo mask sets CNM623 and CNM624 have been designed for the fabrication of DC and AC probes respectively. The design parameters of these two photo mask sets, CNM623 and CNM624, are shown in the tables 3.6 and 3.7, respectively. The CNM623 photo mask set has identical design parameters to that of DC1 except in the CNM623 we included additional SPM probes designs with 30° tip mask angle,angle e in figure 3.2, that will give sharper tetrahedral tips. Whereas in the CNM624 photo mask sets, apart from including additional SPM probes designs with 30° tip mask angle, the length of the SPM probes' cantilevers have been modified to 250μm and 275μm as opposed to 200μm and 225μm in the AC1 photo mask sets to solve the laser alignment problem encountered in characterizing the AC prototype probes that will be discussed in the next chapter. Figure 3.17 and 3.18 shows the CNM623 and CNM624 photo mask sets at different level of detail.

Similar fabrication process to that of the prototype runs is designed for these two

Table 3.6: The design parameters of the CNM623 mask set

Beams	Length (μm)	Width (μm)	Conducting layer width (μm)	Angle
L1	400	40	10	37
L2	400	40	20	37
L3	400	30	10	37
L4	400	30	20	37
L5	300	40	10	37
L6	300	40	20	37
L7	300	30	10	37
L8	300	30	20	37
L9	400	40	10	30
L10	400	40	20	30
L11	400	30	10	30
L12	400	30	20	30
L13	300	40	10	30
L14	300	40	20	30
L15	300	30	10	30
L16	300	30	20	30

Table 3.7: The design parameters of the CNM624 mask set

Beams	Length (μm)	Width (μm)	Conducting layer width (μm)	Angle
L1	250	40	10	37
L2	250	40	20	37
L3	250	30	10	37
L4	250	30	20	37
L5	275	40	10	37
L6	275	40	20	37
L7	275	30	10	37
L8	275	30	20	37
L9	250	40	10	30
L10	250	40	20	30
L11	250	30	10	30
L12	250	30	20	30
L13	275	40	10	30
L14	275	40	20	30
L15	275	30	10	30
L16	275	30	20	30

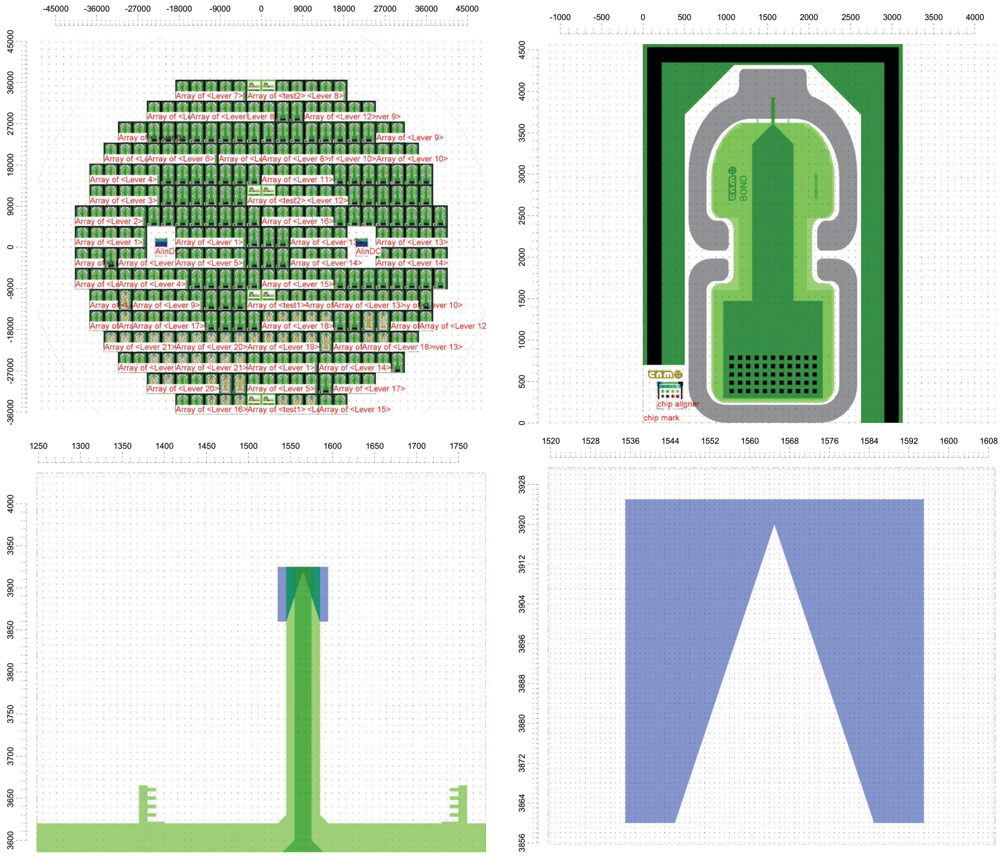

Figure 3.17: Layout of CNM623 mask stet at different level of detail. Top: whole wafer scale (left), a chip (right). Bottom: a probe cantilever (left) and a probe tip (right).

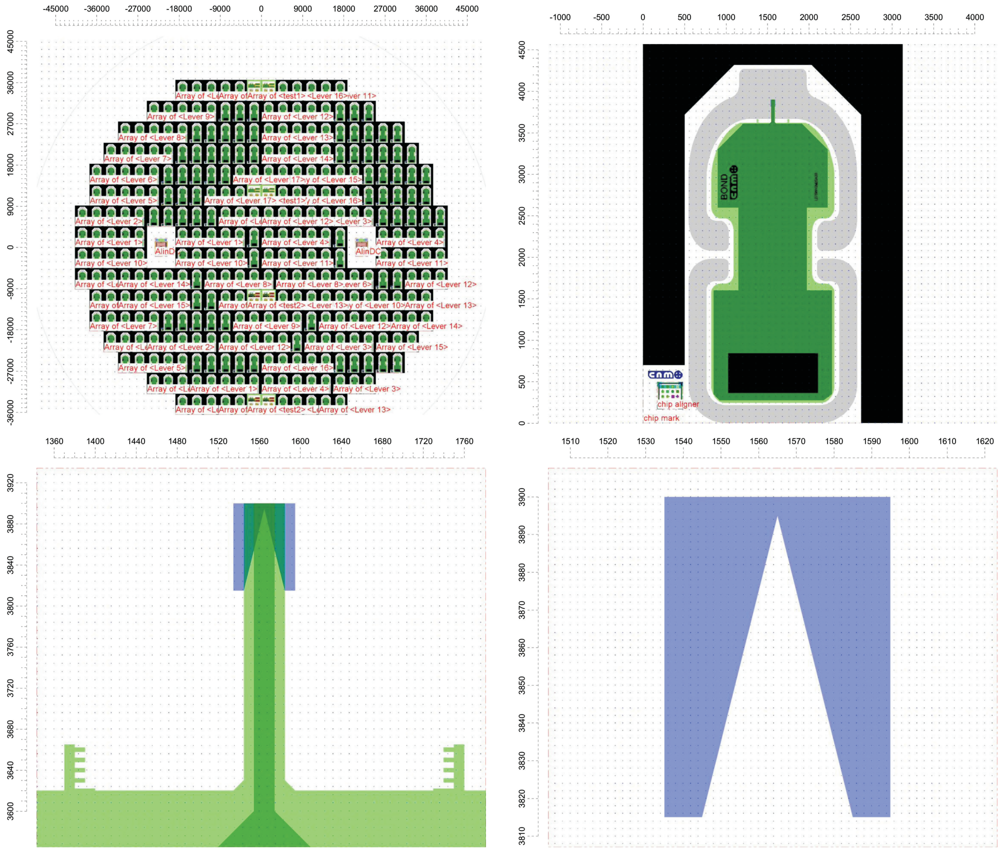

Figure 3.18: Layout of CNM624 mask stet at different level of detail. Top: whole wafer scale (left), a chip (right). Bottom: a probe cantilever (left) and a probe tip (right).

runs, schematically shown in figure 3.10. The starting material is a (100) oriented n-type SOI wafer with $15\mu m$ device layer, $1\mu m$ buried oxide (BOX) layer and $500\mu m$ thick bulk silicon. First we fabricate the tetrahedral tips by opening a hole in the Si device layer with 3G recipe of deep reactive ion etching (DRIE) using the BOX as an etch stop. The top surface is covered by a thin thermal oxide, 100 nm thick silicon nitride plus 100nm thick aluminum (figure 3.10a). This defines the two vertical planes of the tetrahedral tips. The aluminum layer is removed in wet etching and a 400 nm thick wet thermal oxide is grown on the exposed silicon walls using the silicon nitride layer as a mask. The silicon nitride and the thin thermal oxide are removed using wet etching and the wafers are etched in a 25% TMAH solution at 80°C with time control to define the third (111) plane of the tetrahedral tips and the thickness of the cantilevers. This wet etching process is terminated as soon as the remaining silicon layer in the wafers matches the required cantilevers thickness ($2\mu m$ for DC probes and $4\mu m$ for AC probes). The structures of the cantilever and substrate are patterned using $24\mu m$ thick photoresist and NANO1 recipe of DRIE (figure 3.10b). Figure 3.19 is the SEM micrographs of the tetrahedral tips taken at this stage of the fabrication process. Then the 400nm thermal oxide is removed from the vertical side walls of the tetrahedral tips with wet etching and a conducting layer is added to the probes (figure 3.10c). For the AC probes 30 nm Cr + 100 nm Au are deposited using physical vapor deposition and patterned with a lift-off process. 1min ultrasound is used to agitate the lift-off process. For the DC probes the conducting layer is made with 100nm Ti deposition with physical vapor deposition, patterning using a lift-off process plus two thermal annealing steps. 2min ultrasound is employed to agitate the lift-off process. The two thermal annealing steps are performed with a rapid

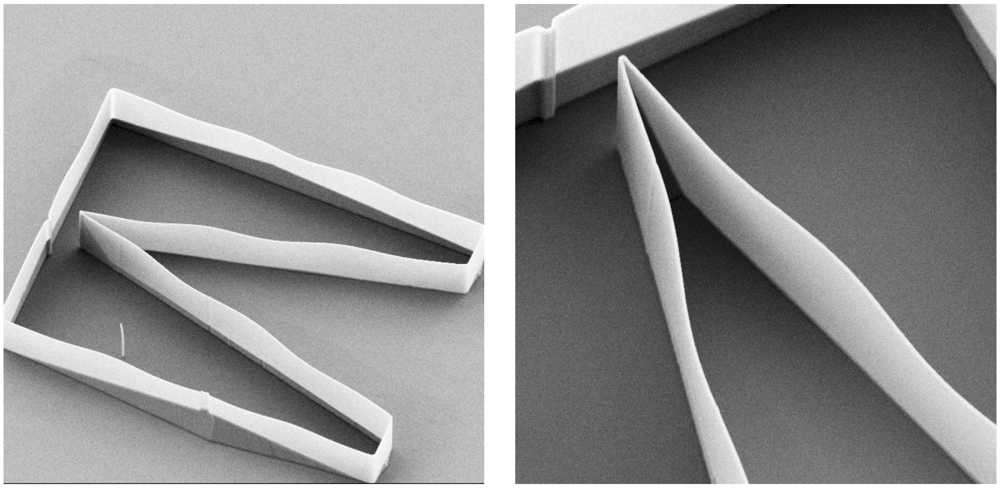

Figure 3.19: SEM micrographs of tetrahedral tips taken after the TMAH etching step that defined the third plane (111) of the tips. Left: side view. Right: front view.

thermal annealing (RTA) equipment. These thermal annealing steps are required to form titanium silicide film as a conducting layer. The firs RTA is performed at 690°C for 30s in nitrogen environment. The non reacted titanium metal and TiN film formed with the reaction of titanium metal with the nitrogen atmosphere are selectively stripped with $H_2O : NH_4OH : H_2O_2$ = 5:1:1 solution at 55°C for 10min. The second RTA is performed at 850°C to convert the high sheet resistivity titanium silicide formed by the first RTA step to low sheet resistivity titanium silicide film. Later a 400 nm thick silicon nitride layer is deposited and patterned so that the whole probe is insulated except at the tips and electrical contact pads (figure 3.10d). Aluminum is added in the DC probes to contact the titanium silicide layer in the pad area. The substrate is etched from the backside by DRIE using an Al mask and the BOX layer as an etch stop. Finally the cantilevers are released by 20min wet etching in SiO-etch solution plus 30s 49% HF vapor etching of the BOX.

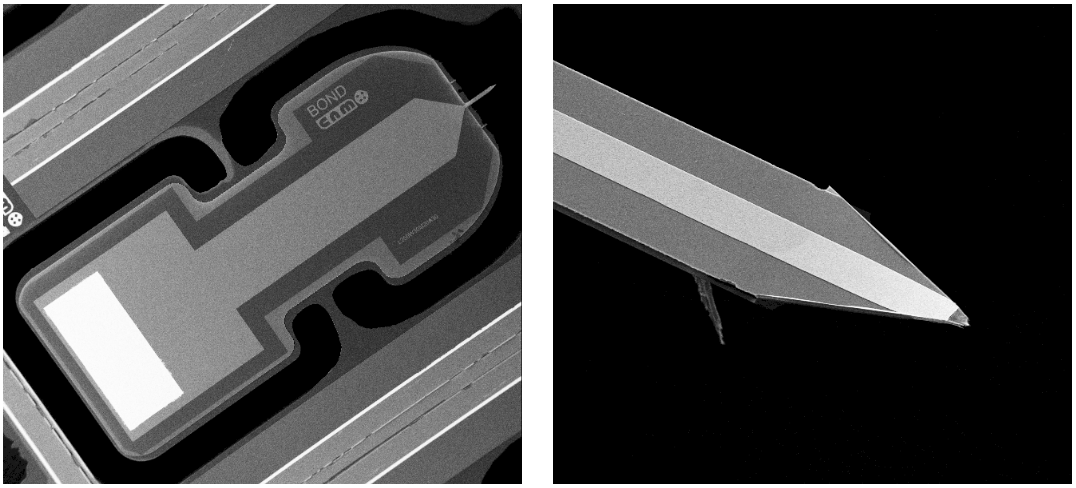

Figure 3.20: SEM micrographs of magnified tip region of AC probes with broken tips.

Figure 3.20 shows the SEM micrographs of whole probe structure (left)and magnified probe tip region (right) of an AC probe. As shown in the SEM micrograph of the whole probe, figure 3.20 (left), the probe cantilever is quite well aligned and the nitride insulation layer is not damaged by the BOX etching conditions. Unfortunately, the BOX etching process described above is not reliable. Additionally, as it is apparent in the SEM micrograph of magnified tip region, figure 3.20 (right), the probe tip is missing. In almost all chips the tips have been broken in a similar pattern. The tips of the DC probes have also been broken in the same manner, figure 3.21. We suspected that the ultrasound used in the lift-off process was the source of tip damage. In addition to tip damage, we also found that the nitride etching technologies available at IMB-CNM clean room facility have poor selectivity to titanium silicide.

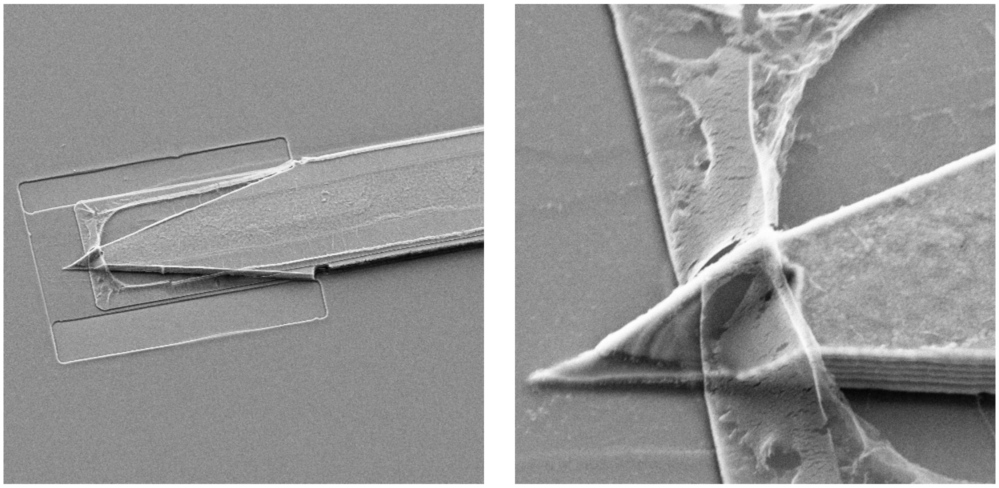

Figure 3.21: SEM micrographs of magnified tip region of DC probes with broken tips.

3.5.4 Test Run 6640

This test run was designed to make some more tests in the BOX etching step from the backside of the wafers to release the probe cantilevers. Figure 3.22 is schematic of the fabrication process. The starting material is a (100) oriented p-type SOI technology wafers with $2\mu m$ thick device layer, $2\mu m$ thick BOX and $490\mu m$ thick bulk silicon. The structures of the cantilever and substrate are defined using photolithography and DRIE (Figure 3.22 B). 100nm thick Al is sputter deposited on the device layer of some of the wafers (Figure 3.22 C). Later $24\mu m$ thick photoresist is coated on the front side of all the wafers to provide mechanical stability to the fragile cantilevers during the backside processing steps. The thin Al layer is intended to protect the photoresist in the device layer from direct contact with an HF vapor during the BOX etching step. The substrate is etched from the backside by DRIE using an Al mask and using the BOX layer as an etch stop. The cantilevers are released by 30% or 49% HF vapor etching of the BOX. The BOX in the wafers with 100nm Al in their

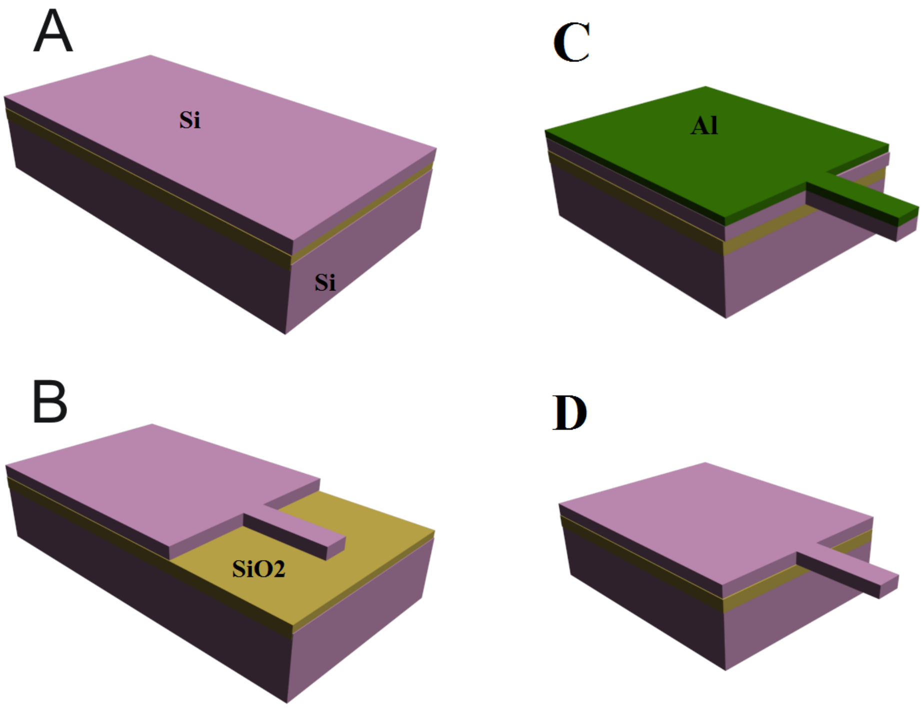

Figure 3.22: Schematics of cantilever fabrication process for the BOX etching test run.

device layer is etched with 49% HF vapor. The wafers without the additional Al in their front side are exposed to 30% or 49% HF vapors to etch the BOX. Later the $24\mu m$ thick photoresist is removed with oxygen plasma. Finally the thin Al layer in the device layer of some of the wafers is removed using wet etching (Figure 3.22 D).

After the BOX etching process was performed, we observed no cracks in the $24\mu m$ thick resist layer in the wafers with the additional 100nm thick Al in their front side. The 100nm thick intermediate Al layer between the photoresist and the BOX layer has completely protected the HF vapor from reaching the resist. Unfortunately, we couldn't remove the thin Al layer completely from the cantilevers after wards (figure 3.23). We have observed multiple cracks in the $24\mu m$ thick photoresist in the wafers

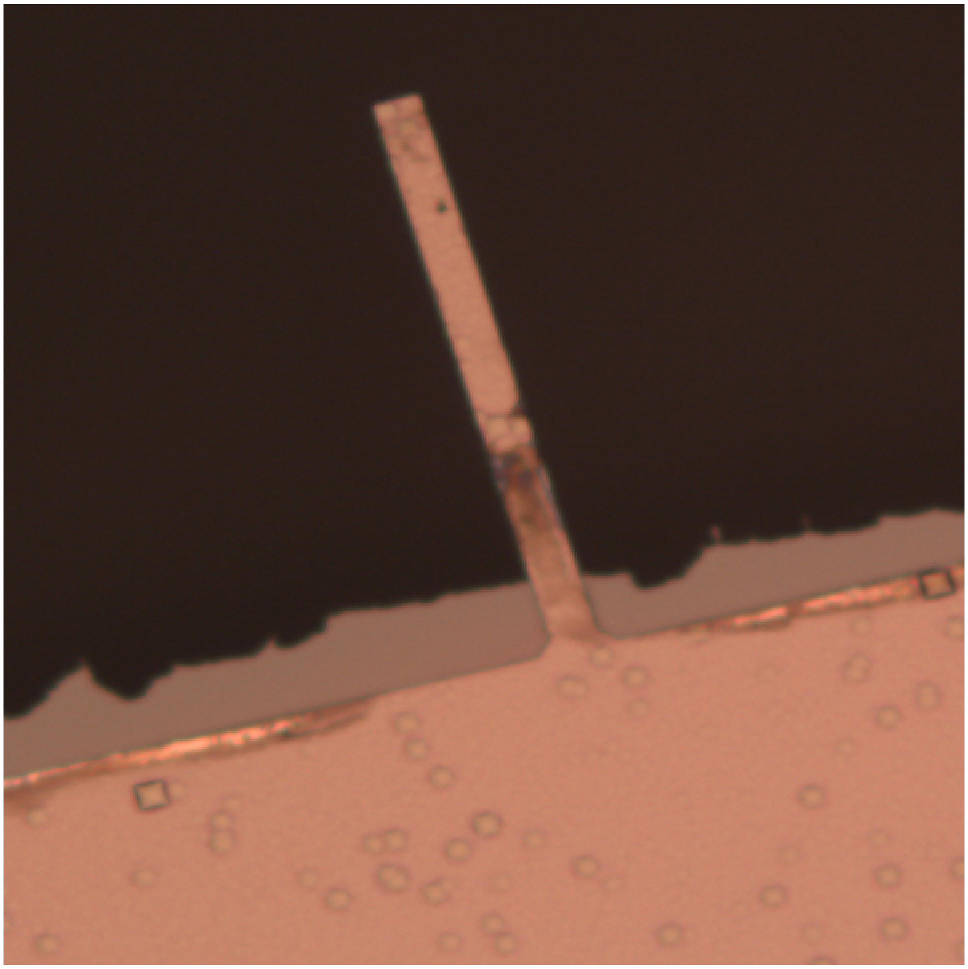

Figure 3.23: Optical microscope image of a cantilever fabricated in this run taken after the fabrication process was finalized.

without the intermediate Al layer due to the diffusion of the HF vapor into the photoresist. There was no significant difference between the wafers processed in 49% HF and 30% HF vapors regarding the crack defects.

3.5.5 Run 6626

This run was designed after we had seen that almost all the tips in the run 6283 were broken. The starting material was a (100) oriented n-type SOI technology wafers with

$15\mu m$ thick device layer, $1\mu m$ thick BOX and $490\mu m$ thick bulk silicon. Essentially, we used identical fabrication process sequences with the run 6283 with very few modifications. The first modification from run 6283 was that the 1min ultrasound used in the lift-off process to define the conducting layer was omitted in this run. The other modification that we made in designing this run was that a sputter deposition step, which deposits 100nm Al on the device layer of the wafers as in section 3.5.4, is introduced just before the $24\mu m$ thick photoresist, which protects the tips and provides mechanical support to the fragile cantilevers during the backside processing steps, was coated. The Al layer was intended to protect the Si_3N_4 layer from the HF vapor attack during the BOX etching step from the backside of the wafers. The fabrication process was finalized by removing the Al layer with wet etching.

During the lift-off process that was employed to pattern the conducting layer of the probes, the wafers were left in acetone for two days. But there were rests of resist and hence metal on the wafers' surface after such a long period in acetone. We tried to remove these rest layers in stripper but we were not successful. Finally we used 3-4 pulses of ultrasound and eventually these rest layers were removed. We inspected the wafers with SEM before and after the application of the ultrasound. Before the ultrasound we didn't observe any broken tips. But after the 3-4 pulses of ultrasound was applied we observed very few tips broken in the same way as in the wafers of runs 6260 and 6283 discussed before.

Figure 3.24 is SEM micrograph of a whole probe (left) and cantilever (right) of an AC probe fabricated in this run. The 100nm thick intermediate Al layer between the photoresist and the BOX layer has completely protected the HF vapor from reaching the resist during the BOX etching with 49% HF vapor from the backside of the wafers

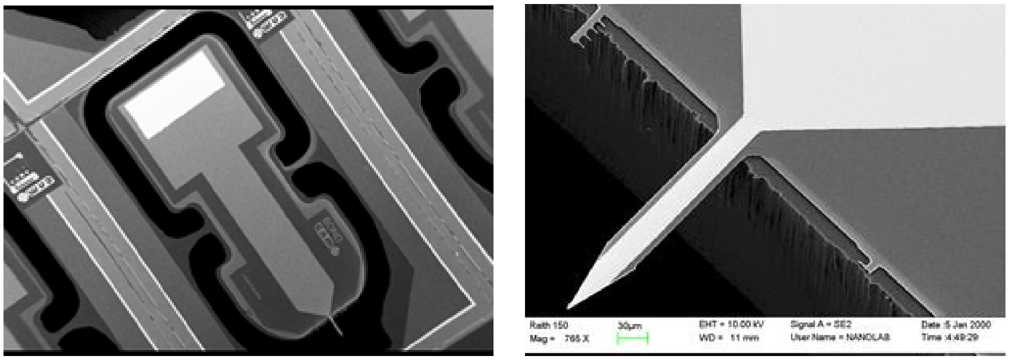

Figure 3.24: SEM micrographs whole probe (left) and cantilever (right) of an AC probe fabricated in this run.

and hence protected Si_3N_4 dielectric from the HF vapor attack (figure 3.25). But in some chips, we observed that the gold conducting layer in the tips and in the contact pad area of the probes was peeled up (Figure3.26).

3.6 Fabrication using optimized process parameters: Runs 6574 and 6729

The starting material is a 100 mm diameter (100) oriented n-type SOI technology wafers with $15\mu m$ device layer, $1\mu m$ buried oxide (BOX) layer and $400\mu m$ thick bulk silicon. Similar fabrication process sequences to that of the prototype runs as in the previous section are used. The fabrication process begins by fabricating the tips by opening a hole in the Si device layer with the 3G recipe of DRIE of silicon process using the BOX layer as an etch stop. The top surface is covered by a thin thermal oxide,100 nm of silicon nitride plus 100nm Al (Figure 3.10a). This defines the two vertical planes of the tetrahedral tips. The Al layer is removed in wet etching and the wafers undergo a wet thermal oxidation process to grow a 400 nm thermal oxide on the

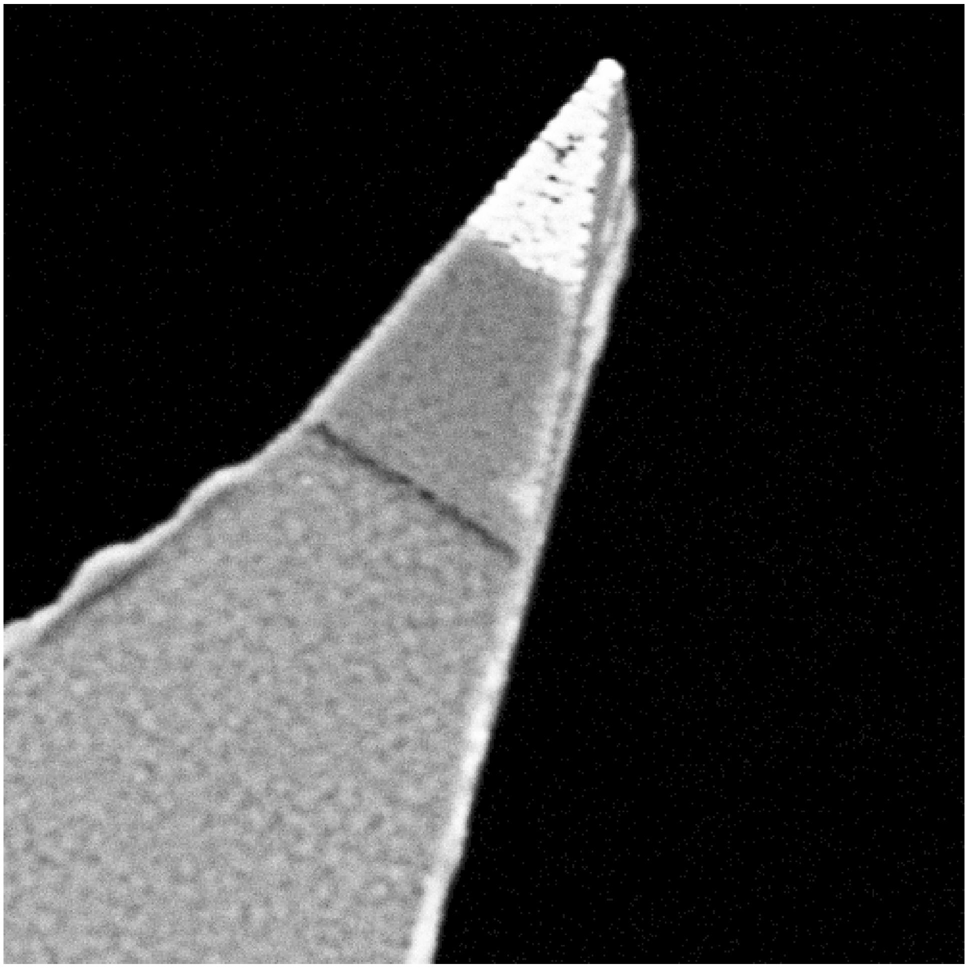

Figure 3.25: SEM micrographs of magnified tip of an AC probe fabricated in this run.

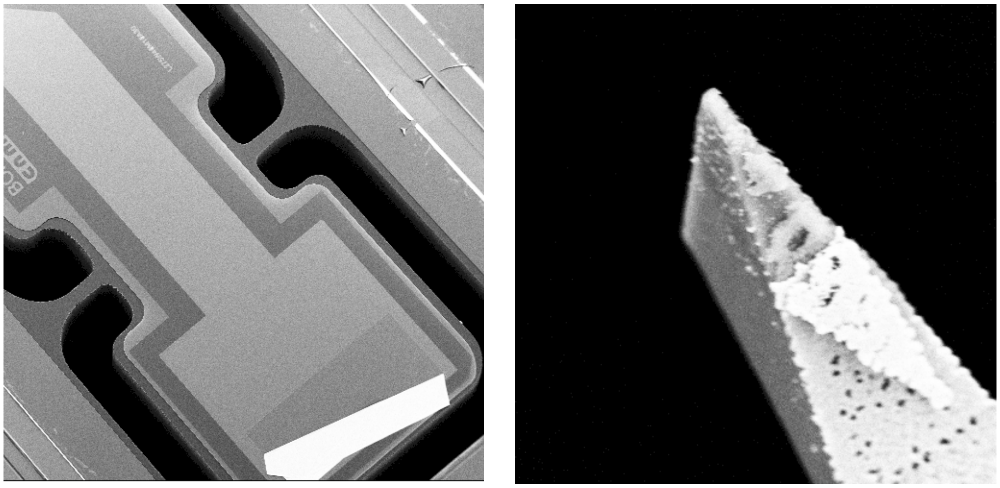

Figure 3.26: SEM micrographs of contact pad area (left) and magnified tip (right) of AC probes fabricated in this run.

exposed silicon walls using the silicon nitride layer as an oxidation mask. The silicon nitride and the thin thermal oxide layers are removed using wet etching processes and the wafers are etched in a 25% tetramethylammonium hydroxide (TMAH) solution at 80°C with time as a control parameter to define the third (111) plane of the tetrahedral tips and the thickness of the cantilevers. This wet etching process is terminated as soon as the remaining silicon layer in the wafers matches the required cantilevers thickness ($2\mu m$ for DC probes and $4\mu m$ for AC probes). The cantilever and substrate shapes are defined with a photolithographic step using $24\mu m$ thick photoresist and etching using DRIE (Figure 3.10b). Then a conducting layer is realized in the probes (Figure 3.10c). In the wafers for the AC probes 30 nm Cr + 100 nm Au are deposited using physical vapor deposition and patterned with a lift-off process. 3-4 pulses of ultrasound is used to agitate the lift-off process. In the wafers for the DC probes, the conducting layer is realized with high-dose boron ion implantation plus annealing. Later a 400 nm thick silicon nitride layer is deposited using PECVD and patterned so that the whole probe is insulated except at the tips and electrical contact pads (Figure 3.10d). For the DC probes, a $1\mu m$ thick aluminum layer is sputter deposited and patterned to make electrical contact to the high boron doped conducting layer in the pad area. The substrate is etched from the backside by DRIE using a 1um thick Al mask layer and using the BOX as an etch stop. Finally the cantilevers are released by etching of the BOX. As the wet etching of the 400nm thick thermal oxide from the vertical side walls of the tetrahedral tips also etched the exposed BOX layer, the BOX layer thickness in the region outside of the cantilevers and probe substrates is less than 1um. The BOX is etched in a step of 30s with 49% HF vapor. The HF vapor etching is stopped when the BOX layer in the region outside of the cantilevers and probe substrates is completely etched, which can be deduced from the optical microscope image color difference in the border of the probe substrates. In the DC probes the remaining BOX layer on the back of the probe cantilevers is removed using dry etching. No further BOX etching is required for the AC probes as the remaining thin BOX layer won't bend the cantilevers. $24\mu m$ thick photoresist is coated on the front side of the wafers to protect the tips and provide mechanical support to the fragile cantilevers during the backside processing steps.

Figure 3.27 is SEM micrograph of tip region (left) and magnified tip (right) of a DC probe taken after the tetrahedral tip definition step was finalized. Figure 3.28 is SEM micrographs of magnified tip taken, after the Cr + Au conducting layer was patterned with a lift-off process, by tilting a wafer to 30° (left) and with no tilt (right). We have obtained very good morphology tetrahedral tips for both DC and AC probes. Figures 3.29 and 3.30 are SEM micrographs of whole probe structure and cantilever, respectively of a fabricated DC probe. And figure 3.31 is SEM micrograph

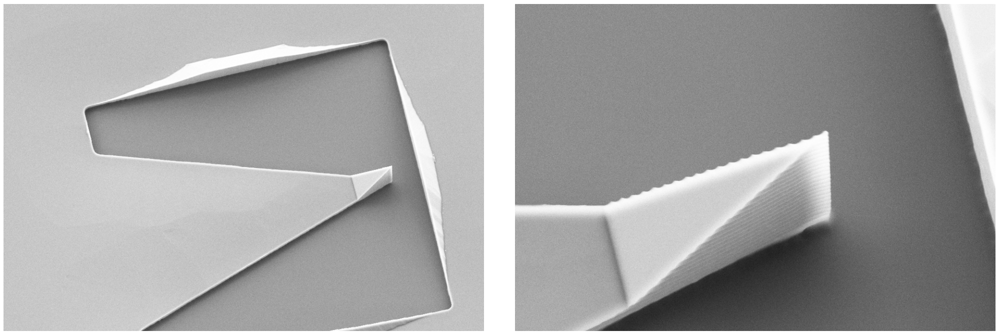

Figure 3.27: SEM micrographs of tip region (left) and magnified tip (right) region of a DC probe taken after the 400Å thick wet thermal oxide was removed from the vertical side walls of the tetrahedral tips.

of magnified tip region of a fabricated DC probe at different level of magnification. Except for the small bending of the cantilevers (figure 3.30), which is due to stress from the silicon nitride passivation layer, the DC probes' cantilevers and tips have very good morphologies. The layer below the cantilevers near the tip region is the silicon nitride passivation layer, figures 3.30 and 3.31. This layer would have not been there had we over exposed the wafers to the 49% HF vapor used to remove the BOX layer. Shown in figures 3.32 and 3.33 are SEM micrographs of a whole probe structure and cantilever, respectively of a fabricated AC probe. And figure 3.34 is SEM micrograph of magnified tetrahedral tip of a fabricated AC probe taken using secondary (left) and back scattered (right) electron detectors. The back scattered electron detector helps to identify material composition. Whereas the secondary electron detector is mainly gives topographic information. The morphology of the fabricated AC probes is very good and no cantilever bending due to the stress from the silicon nitride passivation layer is observed as the cantilevers in the AC probes are stiff by design. Both the fabricated DC and AC probes are well passivated as could be clearly seen in the figures 3.31 and 3.34, respectively.

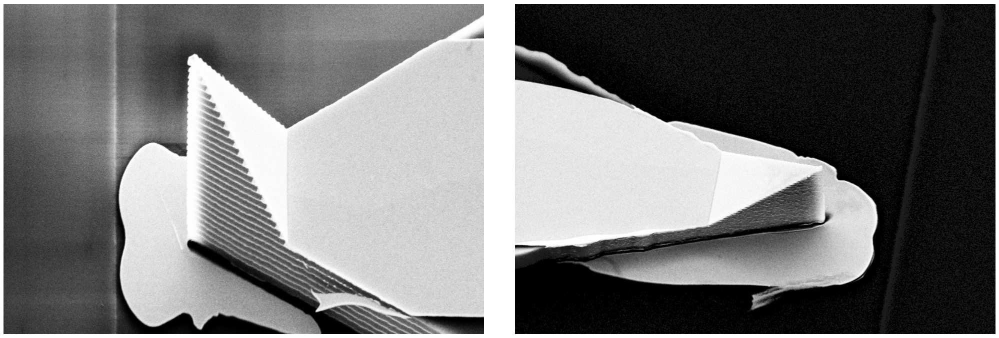

Figure 3.28: SEM micrographs of magnified tip region taken after the Cr + Au conducting layer lift-off process.

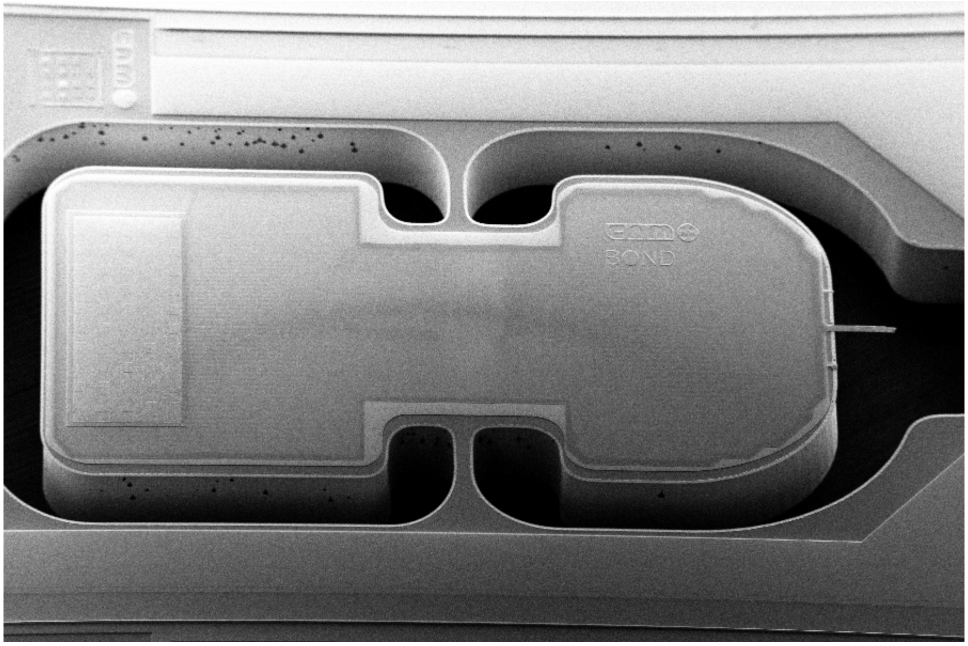

Figure 3.29: SEM micrograph of a DC probe taken after the fabrication process was finalized.

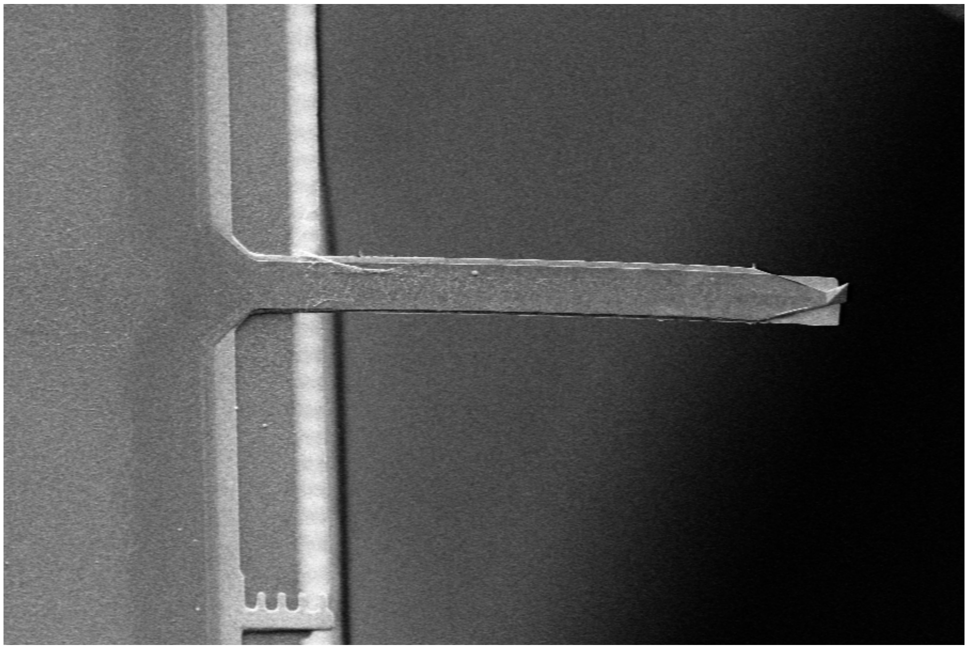

Figure 3.30: SEM micrograph of magnified cantilever region of a DC probe.

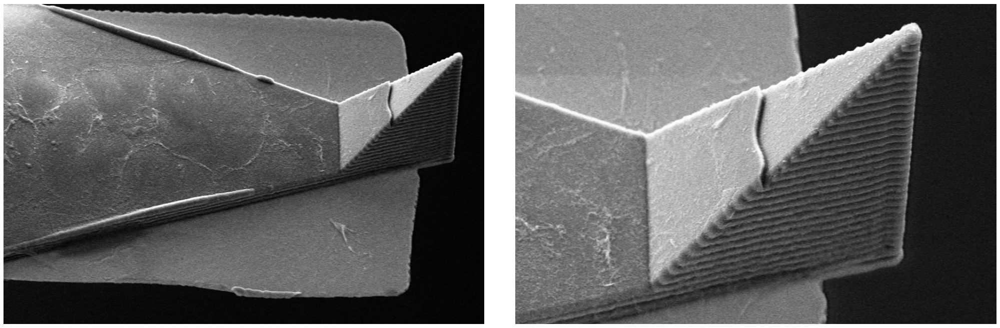

Figure 3.31: SEM micrographs of magnified DC probe tip at different level of magnifications.

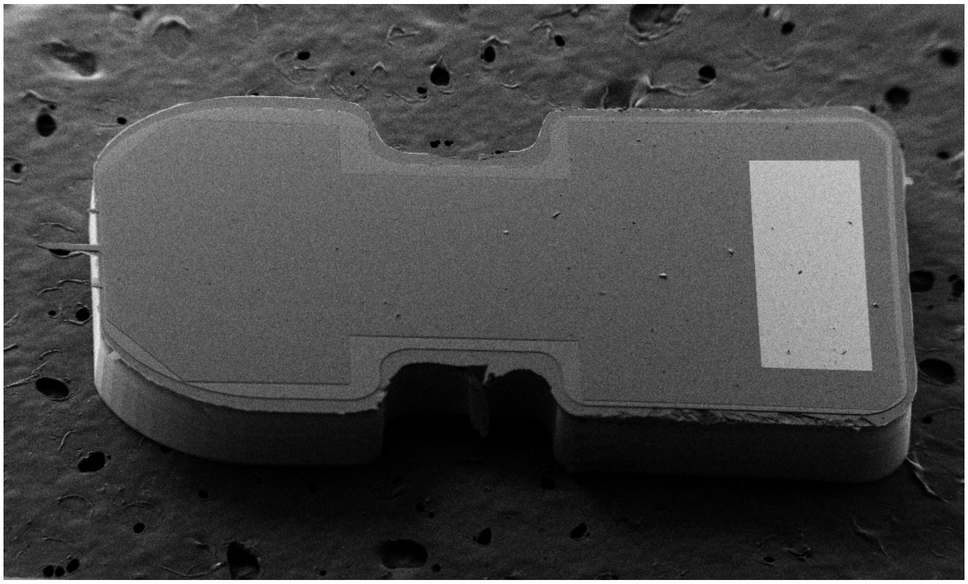

Figure 3.32: SEM micrographs of magnified tip (left) and whole probe (right)of AC probes fabricated using the optimized mask and process parameters.

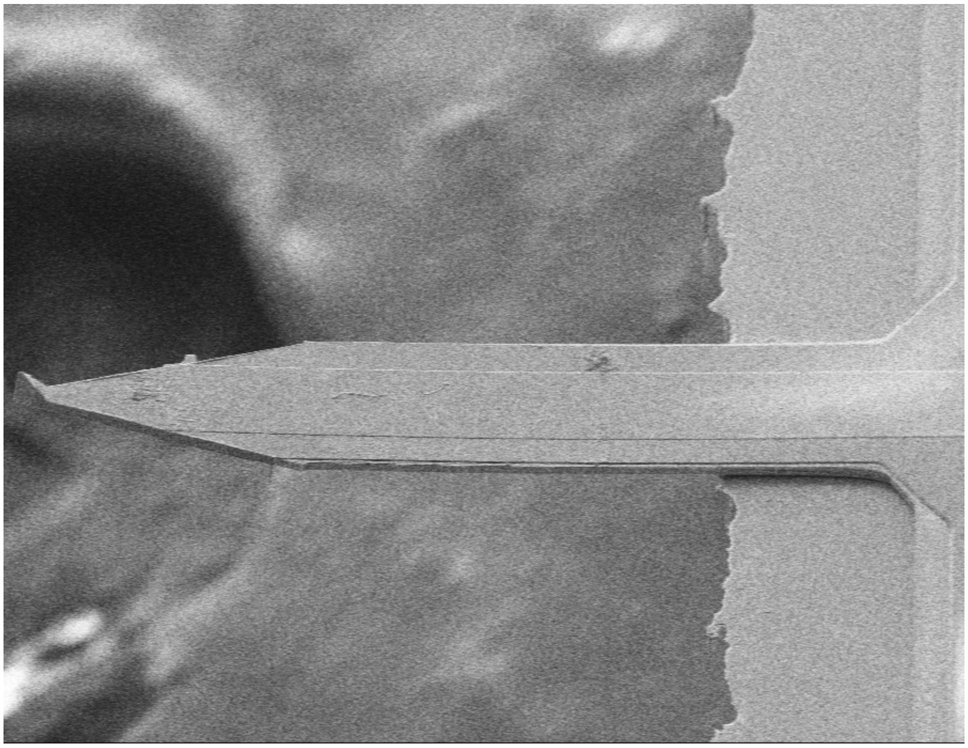

Figure 3.33: SEM micrographs of magnified cantilever region of an AC probe.

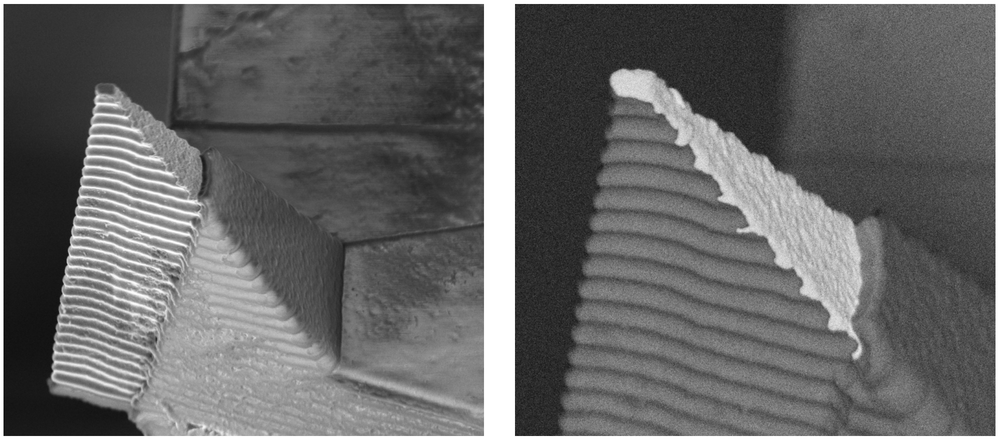

Figure 3.34: SEM micrographs of magnified tip taken using secondary (left) and back scatter (right) electron detectors.

3.7 Alternative fabrication technology test run

This test run was designed to solve the problems encountered in the previous runs in releasing the probe cantilevers by etching the BOX with 49% HF vapor from the backside of the wafers. As silicon will provide better protection to the silicon nitride passivation layer from HF vapor, we proposed to define the cantilever and substrate shapes of SPM probes just after the BOX layer is removed from the backside of the wafers. To this end we will test the possibility of defining cantilever and substrate shapes after BOX layer is removed with 49% HF vapor from the backside of the wafers.

Figure 3.35 is a schematic of the fabrication process. The starting material is a 100 mm diameter (100) oriented n-type SOI technology wafers with $2\mu m$ device layer, $1\mu m$ buried oxide (BOX) layer and $400\mu m$ thick bulk silicon (Figure 3.35 A). 100nm thick silicon nitride is grown on the front side of the wafers using PECVD process. The silicon nitride layer is patterned using photolithographic and RIE processes (Figure

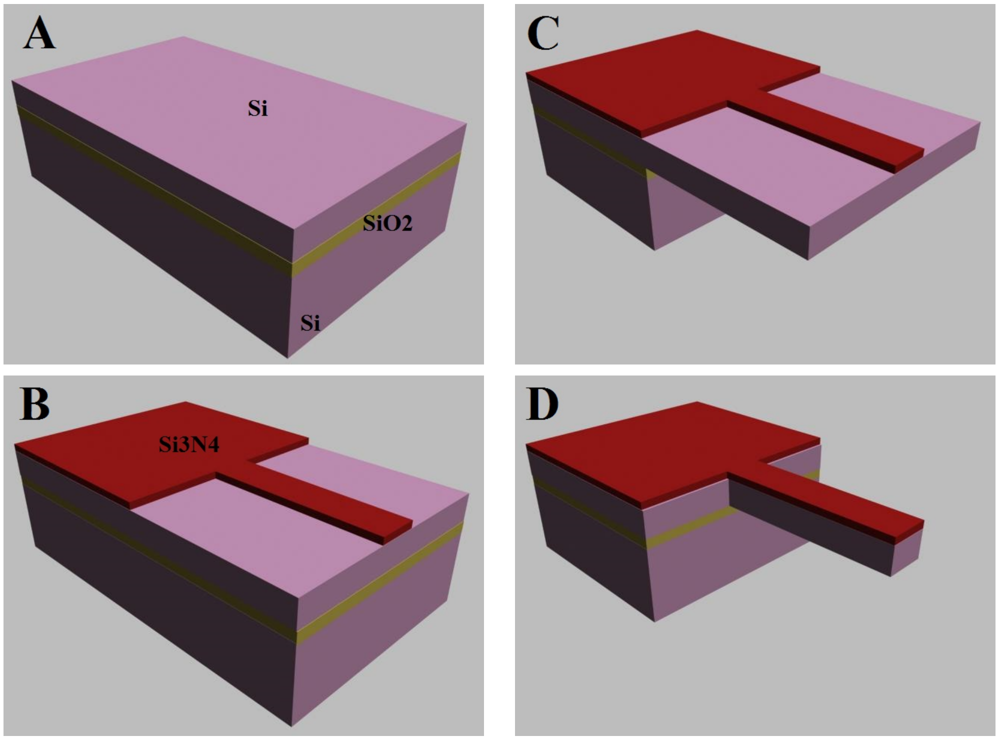

Figure 3.35: Schematic diagram for the fabrication of silicon cantilevers covered with thin silicon nitride layer. This is to test the possibility of defining the cantilever and substrate shapes in the device silicon after the bulk silicon and the BOX layers are removed from the backside of the wafers.

3.35 B). Later the substrate is etched from the backside by DRIE using a 1um thick Al mask layer and using the BOX as an etch stop (Figure 3.35 C). Then the BOX layer is exposed to 49% HF vapor for 5min from the backside of the wafers (Figure 3.35 C). During these backside processing steps the frontside of the wafers are protected with 24um thick photoresist to protect the device layer from possible scratches. Finally the cantilever and substrate shapes are defined using photolithography and DRIE steps (Figure 3.35 D).

Figures 3.36 and 3.37 are SEM micrographs of the whole cantilever-substrate and magnified cantilever structures fabricated in this test run. Straight cantilevers with no damage on the silicon nitride layer were obtained. But an outflow of the resist mask in the final DRIE of the device silicon resulted in strange cantilever edges (Figure 3.37). This DRIE was performed using 3G recipe which has much lower etching rate compared the standard DRIE (P601DEEP) process. We believe that had we used the P601DEEP recipe of DRIE in place of 3G, the resist mask would have little time to outflow and hence better cantilevers would have been fabricated. We can conclude from the results of this test run that cantilever and substrate shape definition in the device silicon, using a photolithographic step and DRIE process, after the bulk silicon and the BOX layers are etched from the backside of the wafers in the fabrication of insulated conductive SPM probes is feasible. This will address the silicon nitride passivation layer damage by the HF vapor during BOX etching step from the backside of the wafers that we encountered in the previous insulated conductive SPM probes fabrication processes.

3.8 Alternative fabrication technology

Here we propose a new fabrication process sequence for the fabrication of AC probes (to measure the AC response in dynamic mode) that will address the issue of silicon nitride passivation layer damage by the HF vapor during the BOX etching step. This fabrication process sequence, with few minor modifications, could also be used to fabricate DC probes (for DC electrical measurements in contact mode) once the conducting layer issue is addressed.

The starting material is a 100 mm diameter (100) oriented n-type SOI technology wafer with $15\mu m$ device layer, $1\mu m$ buried oxide (BOX) layer and $400\mu m$ thick bulk silicon. The fabrication process begins by fabricating the tips by opening a hole

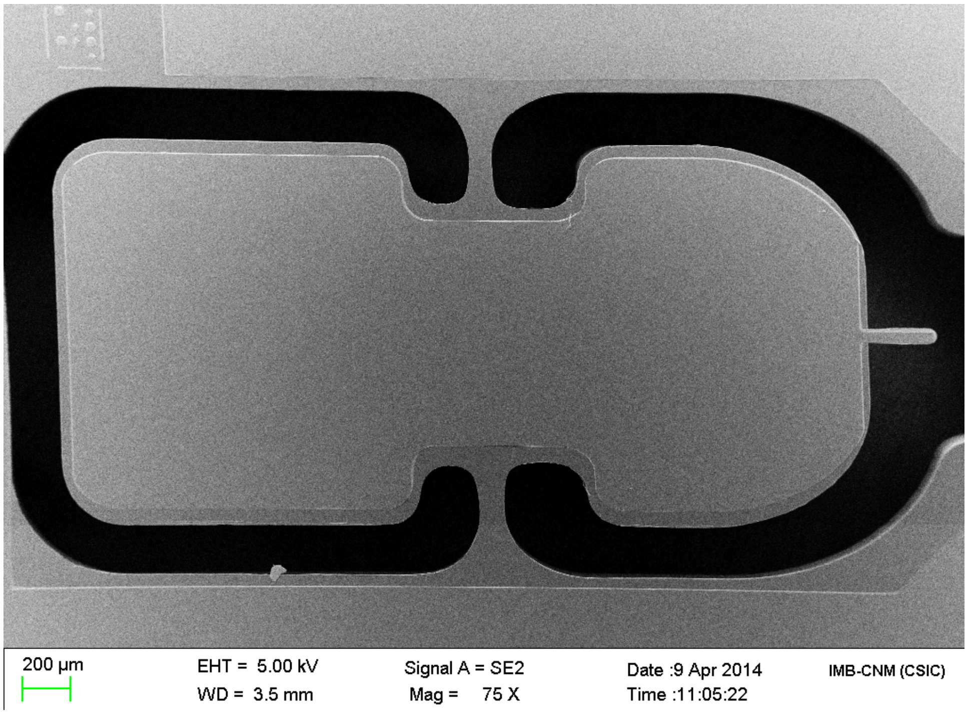

Figure 3.36: SEM micrograph of whole cantilever-substrate structure fabricated in this test run.

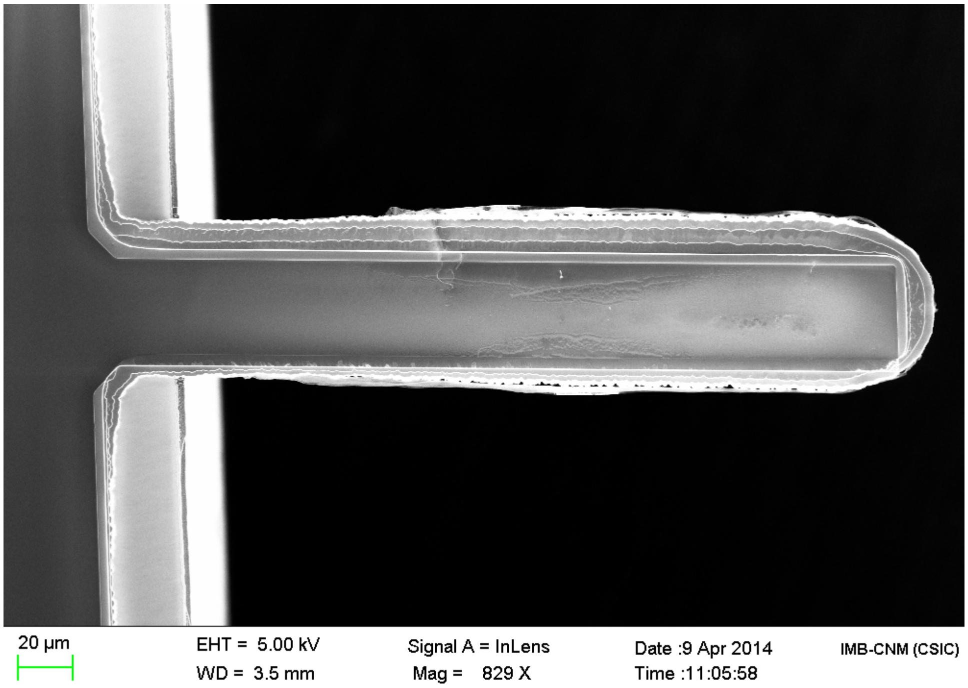

Figure 3.37: SEM micrograph of magnified cantilever region fabricated in this test run.

in the Si device layer with the 3G recipe of DRIE of silicon process using time as a control parameter. The DRIE step should be stopped when the remaining silicon layer matches the required probe cantilever thickness (which is 4um). The top surface is covered by a thin thermal oxide,100 nm of silicon nitride plus 100nm Al (Figure 3.38A). This defines the two vertical planes of the tetrahedral tips. The Al layer is removed in wet etching and the wafers undergo a wet thermal oxidation process to grow a 400 nm thermal oxide on the exposed silicon using the silicon nitride layer as an oxidation mask (Figure 3.38B). The silicon nitride and the thin thermal oxide layers are removed using wet etching processes and the wafers are etched in a 25% tetramethylammonium hydroxide (TMAH) solution at 80°C with time as a control parameter to define the third (111) plane of the tetrahedral tips and the thickness of the cantilevers. This wet etching process is stopped as soon as the remaining silicon layer in the wafers is approximately $4\mu m$, which is the thickness of the cantilevers (Figure 3.38B). Then a conducting layer is realized in the probes using 30 nm Cr + 100 nm Au deposited using physical vapor deposition and patterned with a lift-off process (Figure 3.38C). 3-4 pulses of ultrasound is used to agitate the lift-off process. Later a 400 nm thick silicon nitride layer is deposited using PECVD and patterned so that the whole probe is insulated except at the tips and electrical contact pads (Figure 3.38D). The substrate is etched from the backside by DRIE using a 1um thick Al mask layer and using the BOX as an etch stop (Figure 3.38E). Then the exposed BOX is etched with 49% HF vapor from the backside of the wafers (Figure 3.38E). $24\mu m$ thick photoresist is coated on the front side of the wafers to protect the tips during the backside processing steps. Finally, the cantilever and substrate shapes are defined with a photolithographic step using $24\mu m$ thick photoresist and etching using

DRIE (Figure 3.38D).

3.9 Summary

Figure 3.39 is a Block diagram that summarizes the different technology process runs that we performed to extract optimum design and process parameters for the fabrication of DC and AC probes. The runs are arranged in the block diagram with the first runs in the left and the most recent ones in right of the block diagram. Branching of arrows from a box in the block diagram means the results of the run (whose number and task performed in the run are expressed inside the box) from which the arrows branch were used to design the two runs whose number and task expressed in boxes at which the arrows terminate (one for AC and the other for DC probes fabrication). Finally, marching of two arrows into a circle in a block diagram means the run that follows the circle was used to test some process parameters for the fabrication of AC and DC probes.

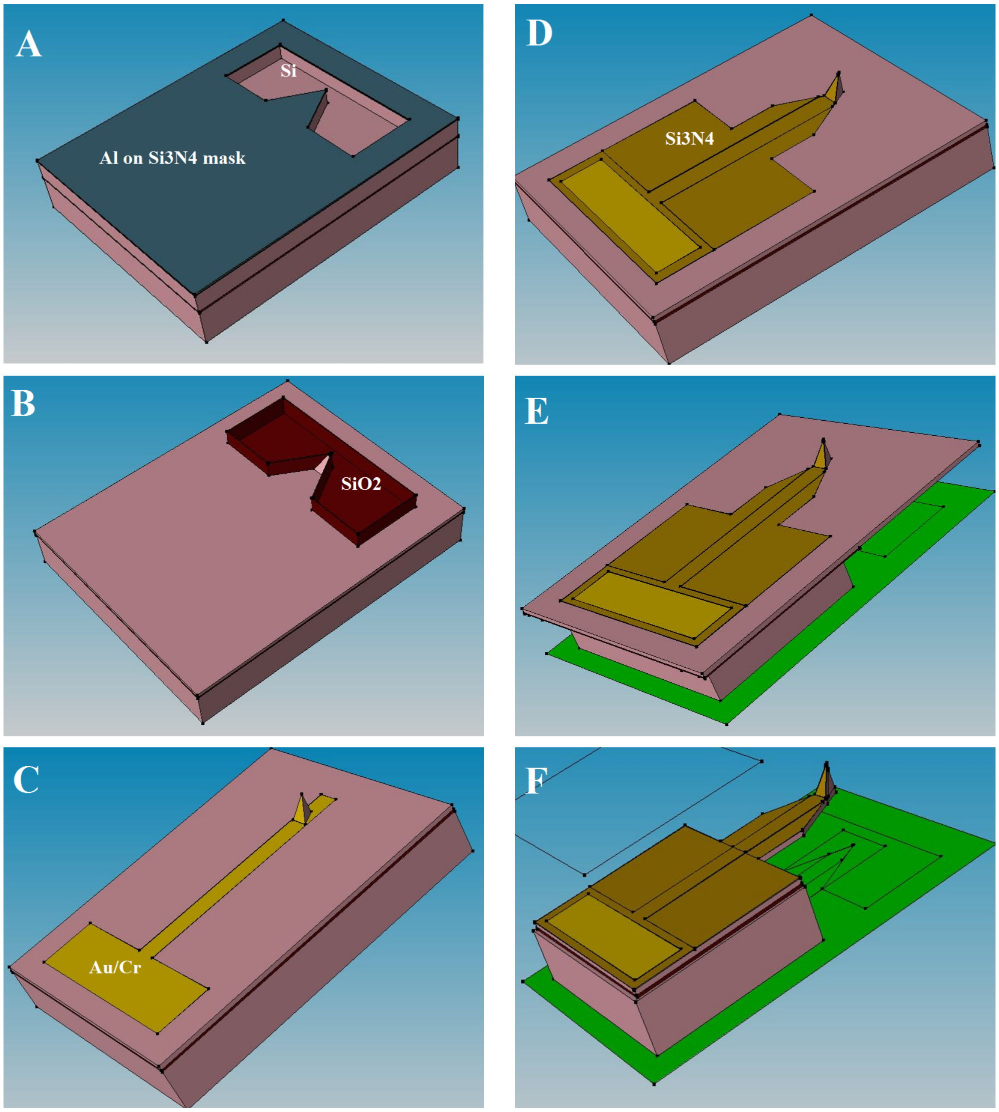

Figure 3.38: Schematic diagram of an alternative insulated conductive SPM probes fabrication sequence that addresses the issue of silicon nitride damage by HF vapor during the BOX etching step.

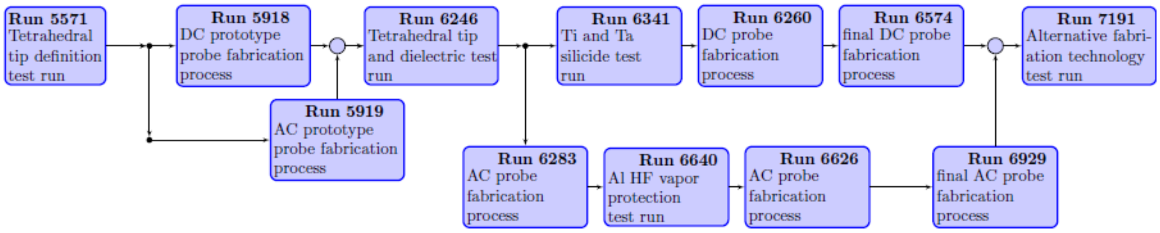

Figure 3.39: Block diagram that summarizes the different technology process runs that we performed to extract optimum design and process parameters for the fabrication of DC and AC probes.

Bibliography

[1] Christine Kranz, Gernot Friedbacher, Boris Mizaikoff, Alois Lugstein, Jrgen Smoliner, and Emmerich Bertagnolli. Integrating an ultramicroelectrode in an afm cantilever: Combined technology for enhanced information. *Analytical Chemistry*, 73(11):2491–2500, 2001. PMID: 11403290.

[2] J. Muller Daniel and F. Dufrene Yves. Atomic force microscopy as a multifunctional molecular toolbox in nanobiotechnology. *Nature Nano*, 3(2):261–269.

[3] A. Cuervo L. Carrascosa Jose L. Fumagalli, D. Esteban-Ferrer and G. Gomila. Label-free identification of single dielectric nanoparticles and viruses with ultraweak polarization forces. *Nature Mater*, 11, 9:808–816, 2012, 09.

[4] Advances in the production, immobilization, and electrical characterization of olfactory receptors for olfactory nanobiosensor development. *Sensors and Actuators B: Chemical*, 116(12):66 – 71, 2006.

[5] M. Gullo, T. Akiyama, N. F. de Rooij, P. Frederix, A. Engel, A. Tonin, and U. Staufer. Insulated Conductive Probes for in situ Experiments in Structural Biology. In *Twannberg Workshop on Nanoscience*, 2002.

[6] Phillip S. Dobson, John M. R. Weaver, Mark N. Holder, Patrick R. Unwin, and Julie V. Macpherson. Characterization of batch-microfabricated scanning electrochemical-atomic force microscopy probes. *Analytical Chemistry*, 77(2):424–434, 2005.

[7] Shinya Akamine and Calvin F. Quate. Microcantilever with integral self-aligned sharp tetrahedral tip. *U.S. Patent*, (5,021,364), June, 1991.

[8] G. Villanueva, J.A. Plaza, A. Sanchez, K. Zinoviev, F. Perez-Murano, and J. Bausells. DRIE based novel technique for AFM probes fabrication. *Microelectronic Engineering*, 84(58):1132 – 1135, 2007.

[9] L. J. Brillson, M. L. Slade, H. W. Richter, H. Vander Plas, and R. T. Fulks. Control of titanium-silicon and silicon dioxide reactions by low-temperature rapid thermal annealing. *Applied Physics Letters*, 47(10), 1985.

[10] A. Kermani, T. Debolske, J. Crowley, and T. Stultz. Process control of titanium silicide formation using rapid thermal processing. *Nuclear Instruments and Methods in Physics Research B*, 21:633–637, 1987.

[11] Ti-silicide formation during isochronal annealing followed by in situ ellipsometry. *Microelectronic Engineering*, 55(14):101 – 107, 2001.

[12] D. Pramanik, A. N. Saxena, Owen K. Wu, G. G. Peterson, and M. Tanielian. Influence of the interfacial oxide on titanium silicide formation by rapid thermal annealing. *Journal of Vacuum Science and Technology B*, 2(4), 1984.

[13] D.L. Kwong. Rapid thermal annealing of co-sputtered tantalum silicide films. *Thin Solid Films*, 121(1):43 – 50, 1984.

[14] R. W. Mann, L. A. Clevenger, P. D. Agnello, and F. R. White. Silicides and local interconnections for high-performance VLSI applications. *IBM Journal of Research and Development*, 39(4):403–417, July, 1995.

Chapter 4

Electrical and Mechanical Characterization of the C-SPM Probes

4.1 Introduction

In chapter 2, we have presented mechanical studies of cantilever beams using beam equations and finite element modeling techniques. These studies will aid for designing cantilever sensors of desired force constant and resonance frequency values. However, the dimensions of the fabricated cantilever beams may not be identical to those in the design due to changes induced by the different fabrication process steps. These process induced dimensional changes of the cantilever beams may some times be too large and hence, the mechanical properties of the cantilever beams are quite different from the desired ones. Therefore, before using fabricated cantilever sensors to perform some experiments, one should calibrate them to get reliable and accurate information about the sample under investigation.

In the case of AFM probes, apart from the probe cantilever one should also know the geometry of the probe tip as the tip geometry has direct effect on the topographic image resolution of the AFM equipment. And the tip geometry also limits the AFM imaging capability of certain structures such as deep trenches. Hence, in topographic study samples using an AFM equipment, one should have prior knowledge of tip geometry and mechanical properties of the probe cantilever to reliably and accurately relate the acquired topographic information to the sample under investigation.

In an electrical characterization of samples using SPM technique in air or liquid media, one should have prior knowledge of the electrical behavior of the conductive probes in order to interpret the acquired electrical signal reliably and accurately. For example in capacitive or impedance spectroscopy of samples using SPM, the total signal is the sum of the actual response of the sample and parasitic terms which arise from the interactions of the conducting path of the probe in the cantilever, cone apex of the tip and probe substrate with the surrounding environment. The actual electrical response of the sample is the one which resulted from the electrical interaction of the tip apex with the sample. But sometimes the electrical contact region between the probe tip and the sample is different from the nominal tip apex size obtained from topographic image resolution or using scanning electron microscopy technique. Hence, prior knowledge of effective electrical tip radius and the level of parasitic electrical signal due to the different parts of the conductive SPM probes will be useful for interpreting electrical signals of samples under investigation.

The mechanical and electrical characterization of the fabricated insulated C-SPM probes discussed in chapter 2 will be presented in this chapter. In section 4.2.1, standard probe tip calibration techniques, in which the tip radii is extracted from the topographic image resolution, will be discussed and then calibration results of our probes will be presented. In section 4.2.2, the common cantilever calibration techniques used to extract the force constant and resonance frequencies of the different modes of mechanical vibrations of probe cantilevers will be discussed. In section 4.2.3, the force constant and fundamental resonance frequency of vibrations of the fabricated probes extracted using the thermal tuning technique will be presented. Finally, in section 4.3, the electrical characterization results of the fabricated C-SPM probes will be presented.

4.2 Mechanical characterization of the fabricated probes

4.2.1 Tip calibration

To get reliable measurement of small sized samples, one needs to use very sharp tips having very small tip radii compared to the lateral size of the sample under investigation. For example to measure a 5nm feature (say a particle), the tip apex size must be in the order of 1nm to get a reliable lateral measurement.

Figure 4.1 shows schematically the artifact in the lateral size of a small sized sample of radii, Rsample with a fat tip of radii, Rtip. The lateral size of the sample as measured with the tip is $2X$, as shown in the figure 4.1. This lateral size of the sample (W) as measured by the tip could be expressed as:

$$W = 2X = 4\sqrt{R_{tip}R_{sample}}. \tag{4.2.1}$$

If there is a way to find the actual sample radii Rsample, the tip radii could be readily computed by inserting the actual sample radii Rsample and the lateral size of the sample (W) as obtained by the tip in equation 4.2.2. To this end, in cylindrical

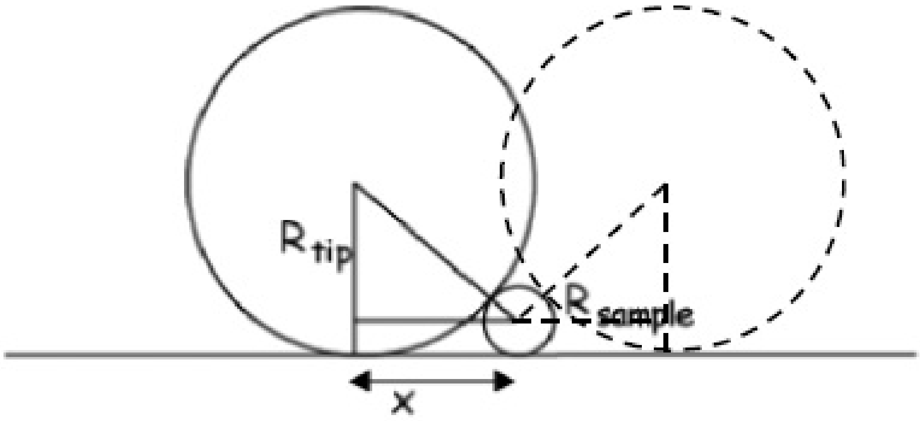

Figure 4.1: Topographic image artifacts of small sample due to finite tip size.

samples such as carbon nanotubes (CNTs), the actual sample radii could be obtained from the height signal. And hence, by imaging CNTs the tip radii for a fat tip could readily be computed from equation 4.2.2.

$$R_{tip} = \frac{\frac{W}{4}^2}{R_{sample}}. \tag{4.2.2}$$

The tip radii and apex cone angle of AFM probes can also be calibrated using nano-structured deep trenches. Figure 4.2 shows the artifacts of the image profile due to the finite tip radii and slope of the side wall of a typical AFM probe. The measured width of the deep trench is less than the actual width of the trench. And the sharp edges of the trench look like some slanted edge which is the convolution of the tip cone. The actual scan profile of a deep trench is dependent on the tip and the trench structure as well. Therefore, by measuring nano-structured deep trenches with known trench width and edge angle, one can extract the tip radii and cone angle of a probe tip from the resulting topographic image.

We have taken AFM topographic images of different samples with the fabricated conductive SPM probes by mounting them in a commercial AFM equipment. These

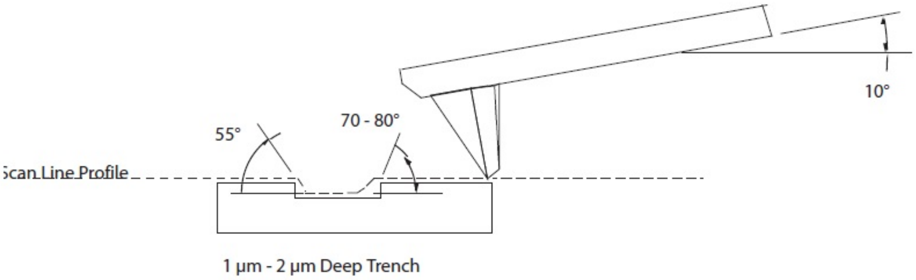

Figure 4.2: Topographic image artifacts of nanostructured deep trenches due to the finite tip size and slanted tip side wall.

experiments were made to observe topographic image qualities obtained by the fabricated probes and hence to estimate their tip radius from the topographic image resolution. Figure 4.3 is the topography of highly ordered pyrolytic graphite (HOPG) (left) and SiO_2 nanostructure (right) samples taken with a prototype DC-probe. These topographic images were taken at Institute for BioEngineering of Catalonia (IBEC). Good quality topographic images of the samples considered have been obtained showing good quality probe tip geometry. And from the topographic image resolution, the tip radius of the probe was estimated to be around 50nm. This tip radius value satisfies the specification as required by the BOND project.

In the case of prototype AC-probes, we were not able to perform mechanical or electrical characterization of the fabricated probes as we could not reliably align the optical laser spot, which is necessary for deflection sensing, on the back of the probe cantilevers. This phenomenon is illustrated schematically in figure 4.4. As the probe cantilevers are short by design and the substrate wall is vertical, as it was defined with DRIE of silicon, the substrate blocks the laser spot from reaching the free end of the probe cantilever, figure 4.4 (left). In the commercial AFM probes, this problem is not observed for the same probe cantilevers dimensions as the probe substrate is

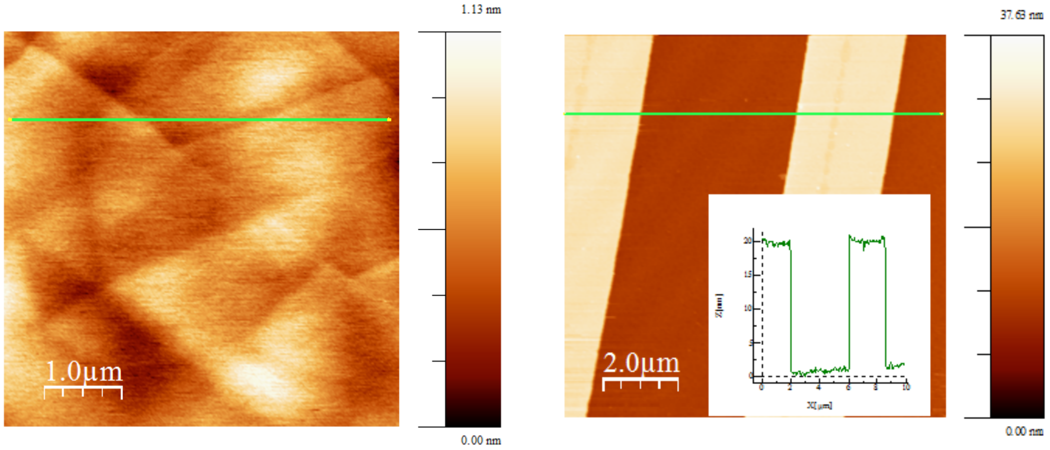

Figure 4.3: Images taken with the fabricated prototype DC-probes (AC-mode). Topography of HOPG. Topography of silicon dioxide nanostructure on silicon substrate (right).

defined with wet anisotropic silicon etching process and hence the substrate wall is at slanting angle, figure 4.4 (right). To avoid similar problems in the final AC-probes, the probe cantilever lengths were modulated to 250μm and 275μm in the final photo mask designs sets, CNM624, compared to 200μm and 225μm in the first photo mask sets, AC1, used for the fabrication of prototype AC-probes as discussed in chapter 3.

We have also characterized the final conductive SPM probes fabricated with optimized design and process parameters by mounting them in a commercial AFM equipment. We didn't encounter any laser alignment problem in both DC and AC probes as was in the prototype AC-probes. To observe the topographic image quality obtained with the probes and hence to estimate the probes tip radius from the topographic image resolution, we have taken topography of different samples with the probes. Figure 4.5 is topography of HOPG (left, taken at IBEC) and interdigitated

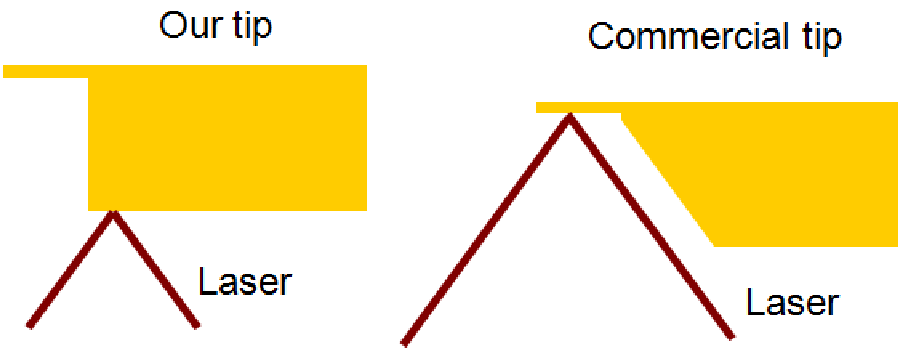

Figure 4.4: Schematics showing laser alignment in short cantilever probes with vertical and slanting substrate walls.

metal electrodes with 150nm pitch and 100nm metal thickness (right, taken at IMB-CNM) samples taken by AC-probes in tapping mode. Figure 4.6 is topography of silicon dioxide nanostructures on doped silicon substrate (left, taken at IBEC) and a carbon nanotube on silicon substrate (right, taken at IMB-CNM) samples taken by AC-probes in tapping mode as well. And figure 4.7 is topography of the inter-digitated metal electrodes (left) and the carbon nanotube (right) samples taken at IMB-CNM with a DC-probe operating in AC mode. As it is apparent in the figures 4.5, 4.6 and 4.7, we have obtained good quality of topographic image of samples with both AC and DC probes which shows the good quality of the probe tips. From the topographic image resolutions, the tip radius of the probes is estimated to be in the range of 30-50nm.

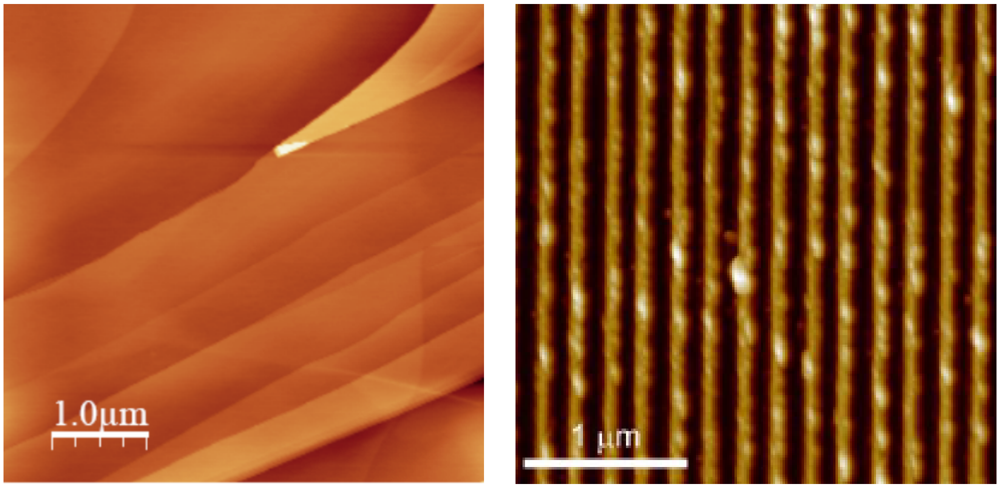

Figure 4.5: Images taken with the fabricated probes (AC mode). Topography of HOPG. Topography of inter-digitated metal electrodes on silicon dioxide.

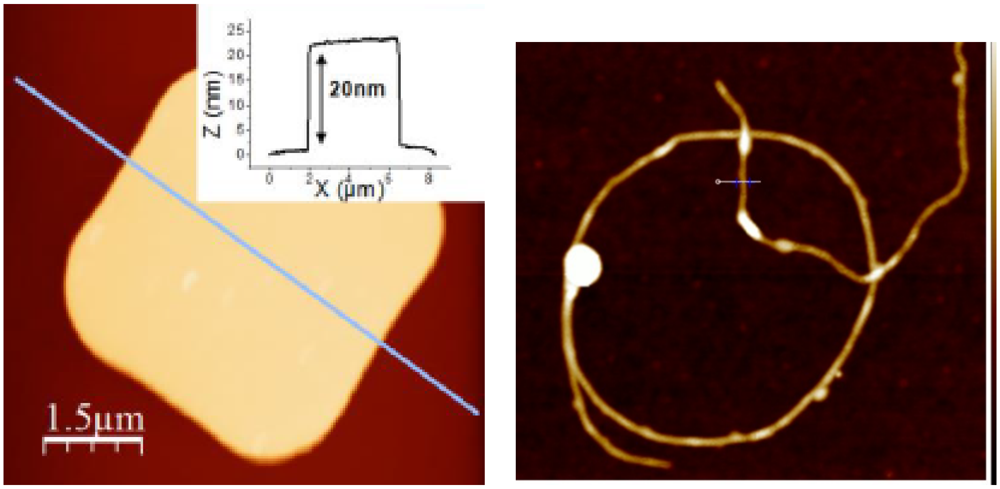

Figure 4.6: Images taken with the fabricated probes (AC mode). Topography of a silicon dioxide nanostructure on a doped silicon substrate (left).Topography of a carbon nanotube on silicon substrate (right, color vertical scale 0 to 9 nm).

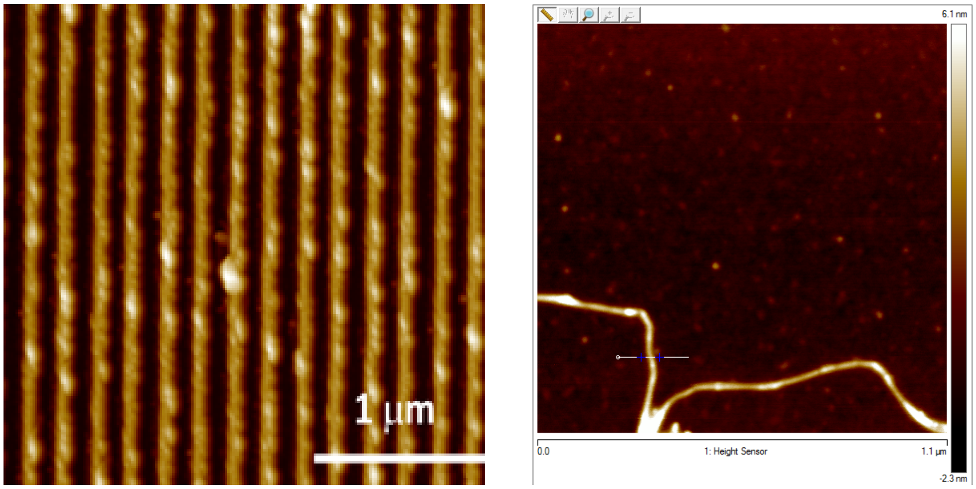

Figure 4.7: Images taken with the fabricated DC probes (AC mode). Topography of inter-digitated metal electrodes on silicon dioxide substrate. Topography of a carbon nanotube on silicon substrate (right).

4.2.2 Probe cantilever force constant calibration techniques

In the AFM topographic characterization of samples, the probe cantilever deflects in response to a force on the probe tip. The cantilever deflection is measured by an optical laser bouncing from the top of the cantilever free end into a photodetector as a function of time. As the probe cantilevers are sufficiently small in most contact and tapping mode AFM operations, the relation between the force and the cantilever deflection can be approximated by linear relation, Hooke's law applied to a spring, given by:

$$F = -k \times h, \tag{4.2.3}$$

where $F =$ the force on the tip in Newton, $h =$ vertical displacement of the free end of the cantilever toward or away from the sample in meters, and $k =$ the proportionality constant, known as the spring (force) constant, in Newtons/meter (or equivalently, and more typically in nanoscale work, in picoNewtons/picometer).

Given the force constant of a probe cantilever, measured probe cantilever deflections can be converted into tip/sample forces. Hence, the first step in making accurate force measurements using AFM is the determination of the force constant of the probe cantilever to be used. The force constant is a property of the probe cantilever. If determined in air, the force constant applies to the same probe cantilever in water or vacuum. Four methods are mostly used to deduce the force constant value of an AFM probe cantilever. These are estimation from representative geometry, comparison of the resonance frequency with and without added mass, thermal tuning and by hydrodynamic model.

The force constant estimation from the probe cantilever geometry provides quick determination of the force constant value but suffers from uncertainty because typically the specific cantilever geometry is not measured and may vary in production. Instead, a representative of the appropriate family of cantilevers is used. Each cantilever family is distinguished by a tip factor, b in $Newton - second^3/meter$, and the force constant for a cantilever in a family is derived from the measured resonant frequency, f of the free cantilever in air by [1]:

$$k = b \times f^3. \tag{4.2.4}$$

The assumptions that go into this relation are that cantilevers within a family agree in material properties and in geometry, with the exception of cantilever thickness.

Adding mass to the cantilever method of force constant calibration requires careful work that is rewarded with a more accurate value. In this method, the resonance frequency of the cantilever is measured before and after adding a known mass to the cantilever and the resonance frequency shift specifies the cantilever force constant.

The resonance frequency of a cantilever beam is given by [1]:

$$f = \frac{\omega}{2\pi} = \frac{1}{2\pi}\sqrt{\frac{k}{M + m^*}}, \tag{4.2.5}$$

where m^* and M are the effective mass of the cantilever and the known mass added to the cantilever free end, respectively.

Comparing the resonance frequency obtained using the above equation with the added mass to that without any is sufficient to solve for both the force constant and the effective mass of the cantilever. The accuracy of force constant determination with this method depends primarily on the uncertainty in the added mass as the resonant frequencies typically may be measured to higher precision.

The thermal tuning method of force constant calibration is often preferred because it is neither as demanding and time consuming as attaching a particle nor has as large an associated uncertainty as relying in the representative model. The measurement data consists of a time interval of the deflection signal in contact mode (with no driving oscillation applied electronically) at thermal equilibrium, while the cantilever is suspended, away from any solid surface. Brownian motion of surrounding molecules impart random impulses to the cantilever during the sampling. The resulting function of time is Fourier transformed to obtain its Power Spectral Density (PSD) in the frequency domain. Integrating the area under the resonant peak in the spectrum yields the power associated with the resonance.

The dynamics of the cantilever beam in thermal equilibrium to the surrounding environment can be approximated by the dynamics of an harmonic oscillator [2]. According to the equipartition theorem the average of the kinetic and potential energy terms of an harmonic oscillator (cantilever beam) in thermal equilibrium to an environment at a temperature T in Kelvin are both equals to

$$\frac{1}{2}k_B T, \tag{4.2.6}$$

where k_B is the Boltzmann's constant. In particular the average potential energy of the cantilever beam is expressed as,

$$\langle\frac{1}{2}m\omega_o^2 z^2\rangle = \frac{1}{2}k_B T, \tag{4.2.7}$$

where $\omega_o = \sqrt{(\frac{k}{m})}$ is the angular resonance frequency, m is the effective mass, z is the displacement of the free end of the cantilever and the 'angle' brackets indicate average value over time. Hence, the force constant of the cantilever is expressed as,

$$k = \frac{k_B T}{\langle z^2\rangle} = \frac{(k_B T)}{P} \tag{4.2.8}$$

The original displacement time-series is Fourier transformed to segregate other, broadband, noise contributions from the narrowband thermal noise around resonance. By integrating the area under the resonance in the PSD, while excluding both the noise floor and the "shoulders" to either side of the resonance peak, only the power, P, of the thermal cantilever fluctuations, which is equal to the mean square of the time-series data, is included.

The accuracy of the thermal tune method of cantilever spring constant calibration depends not only on the effective isolation of non-thermal noise contributions to the PSD, but also on the accuracy of the PSD and on its magnitude. The Nyquist Sampling Theorem guarantees Fourier Transform accuracy for frequencies up to one half the sampling rate. This particularly constrains using the method for small cantilevers in air. The thermal tune technique is mainly applicable to soft cantilevers, particularly in fluids where cantilever resonant frequencies are considerably lower than in air [2].

In the hydrodynamic technique of cantilever force constant calibration, the force constant of the rectangular cantilever beams are easily computed by comparing the resonance in vacuum to resonance in fluid and by introducing the hydrodynamic function, $\Gamma(\omega)$, which depends on the fluid Reynolds number, as [3]:

$$k = 0.1906\rho_f W^2 L Q_f \Gamma_i(\omega_f)\omega_f^2, \tag{4.2.9}$$

where W and L are the width and the length of the rectangular cantilever respectively, ρ_f = density of the fluid, Q_f = the cantilever resonance quality factor in fluid, ω_f = cantilever angular resonant frequency in the fluid and Γ_i = the imaginary component of the hydrodynamic function, $\Gamma(\omega)$. The limitations of the hydrodynamic method of cantilever force constant calibration are that the method is applicable to a high aspect ratio cantilever with $\frac{L}{W} > 5$ and a high quality resonance ($Q_f \gg 1$) is required.

4.2.3 AFM probe cantilever force constant calibration using the thermal tune technique

In calibrating the force constant of a cantilever beam, two steps are followed. The first step is to obtain the sensitivity of the cantilever in force mode. The deflection sensitivity of the cantilever is calculated based on the assumption that the tip and the sample do not deform. Hence, the deflection sensitivity calibration must be done on a hard, stiff surface. This should be made on a hard surface. After the deflection sensitivity data is acquired, the sensitivity should be updated and the probe withdrawn.

The second step in the force constant calibration of a cantilever using the thermal tune technique is to apply thermal tune to obtain cantilever deflection due to the random bombardment by the Brownian particles in the ambient. A number of steps are involved in acquiring cantilever deflection due to the random motion of ambient particles. First cantilever deflection information is obtained in the time domain after selecting frequency range over which the thermal tune is applied. Then the deflection information obtained in the time domain is Fourier Transformed to get the PSD. Either air or fluid could be chosen in the thermal tune panel to select Lorentzian or a simple harmonic oscillator model, respectively, of PSD to be least squares fit to the data. Finally the force constant of the cantilever is calculated after the bandwidth of the PSD fit is adjusted so that all frequencies that contribute power to the spectrum are included.

Figure 4.8 is cantilever deflection signal (nm) vs probe tip approach (nm) of a prototype DC-probe with $400\mu m$ long and $30\mu m$ width cantilever dimensions to a hard silicon substrate taken in the force mode. The measured cantilever sensitivity was $74nm/V$. And figure 4.9 is spectrum of the cantilever deflection data obtained using the thermal tune technique. The fundamental resonance frequency of the cantilever is 16kHz and its force constant was calculated to be 0.09N/m. The force constant and fundamental resonance frequency of the probe cantilever obtained using the thermal tune technique are consistent with the force constant and fundamental resonance frequency values obtained using the analytical and FEM simulation techniques discussed in chapter 2. Furthermore, the force constant of the fabricated prototype DC probe satisfies the specification as required by the BOND project, i.e., force constant value less than 1N/m.

As in the case of the fabricated prototype DC-probes, we used the thermal tuning technique to extract the force constant and fundamental resonance frequency of the

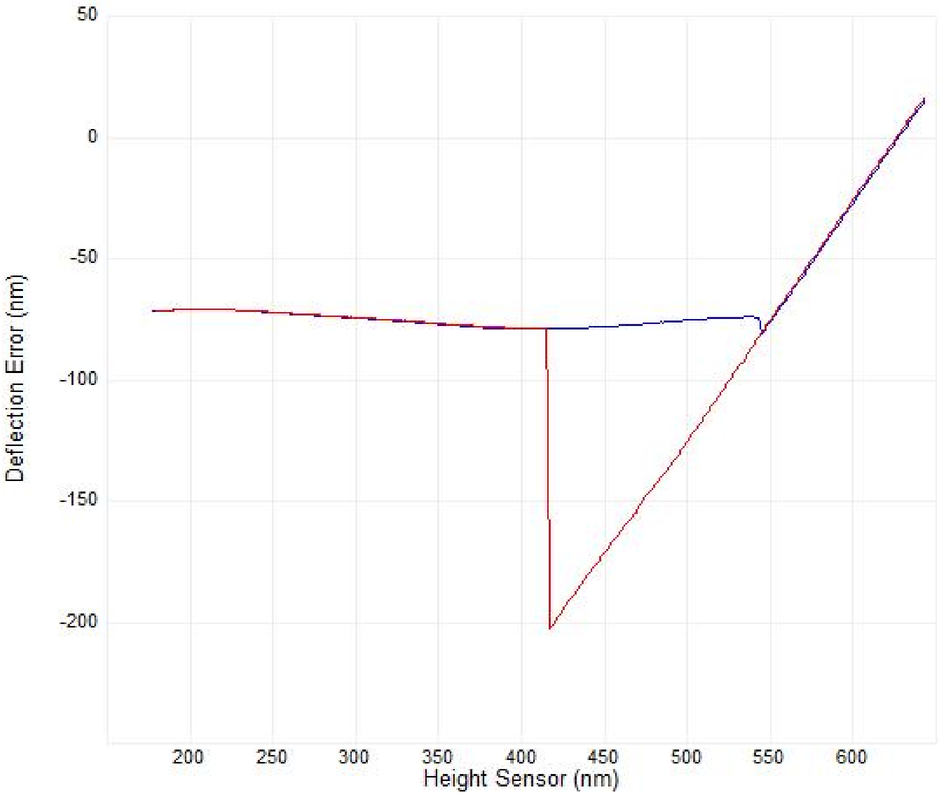

Figure 4.8: Deflection error (nm) vs distance curve of a DC prototype probe with 400um length, 30um width and 2um thickness cantilever dimensions taken on a hard silicon substrate in force mode. Approach (blue) and retract (red) curves.

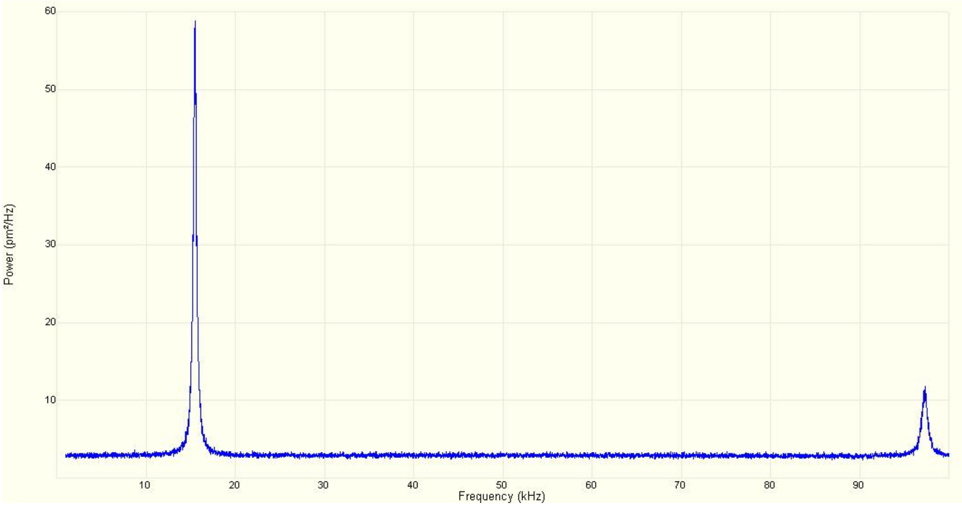

Figure 4.9: Spectral information of the DC prototype probe cantilever, whose force curve is given in figure 4.8, obtained using the thermal tune technique.

fabricated final DC and AC probes. The force curve was obtained by pressing the probes into a hard silicon substrate. Figures 4.10 and 4.11 are the force curves of a DC and AC probes, respectively. Sensitivity values of 213nm/V for the DC probe and 117nm/V for the AC probe were extracted from their respective force curves. Figures 4.12 and 4.13 are spectrum of cantilever deflection data of the DC and AC probes, respectively obtained using the thermal tune technique. And figure 4.14 is zoom of the AC probe cantilever spectrum near the resonance peak together with the Lorentzian model least square fit (red curve). Fundamental resonance frequency value of 43 kHz for the DC probe and 107.3 kHz for the AC probe were obtained from their respective spectrum of cantilever deflection data. Force constant values of 0.6N/m for the DC and 6.32N/m for the AC probes probes were extracted from their respective spectrum data and sensitivity values. The force constant value of the probes satisfies the specification as required by the BOND project.

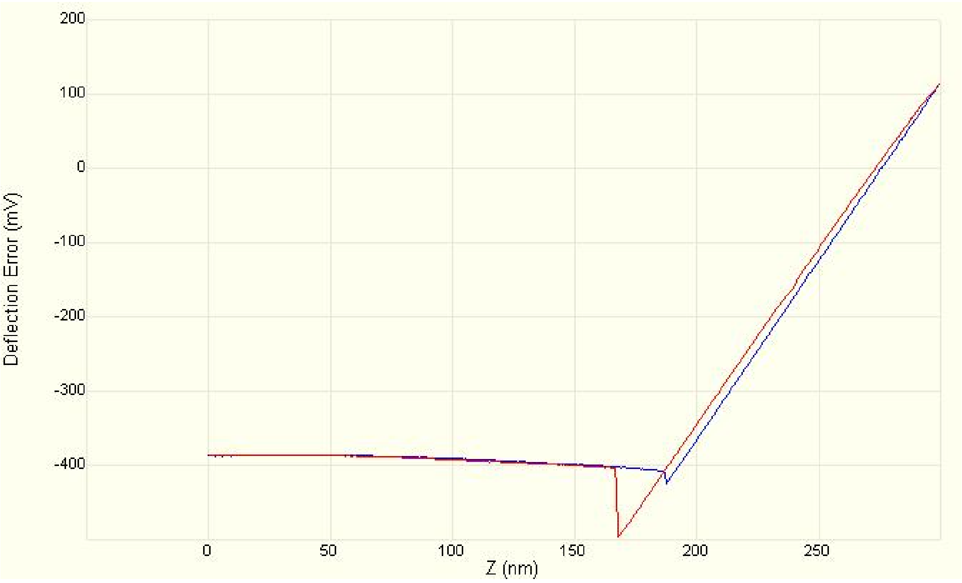

Figure 4.10: Deflection error (mV) vs tip-substrate distance curve of a DC probe taken on a hard silicon substrate in force mode. Approach (blue) and retract (red) curves.

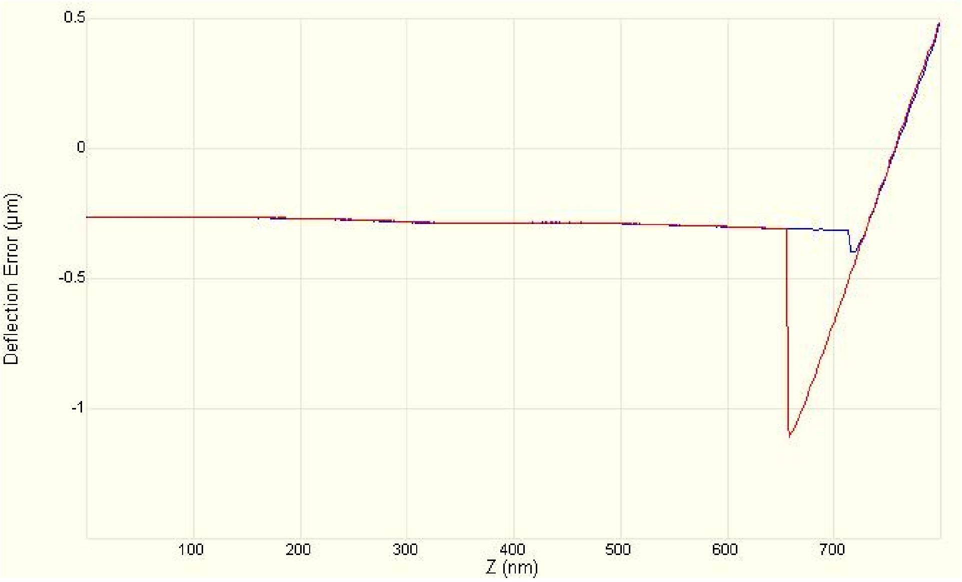

Figure 4.11: Deflection error (μm) vs tip-substrate distance curve of an AC probe taken on a hard silicon silicon substrate in force mode. Approach (blue) and retract (red) curves.

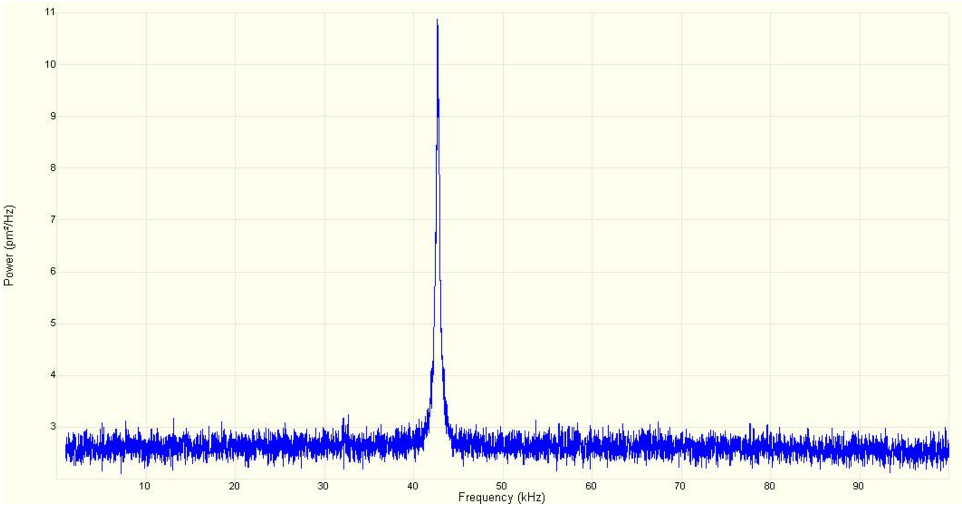

Figure 4.12: Spectral information of the DC probe cantilever, whose force curve is given in figure 4.10, obtained using the thermal tune technique.

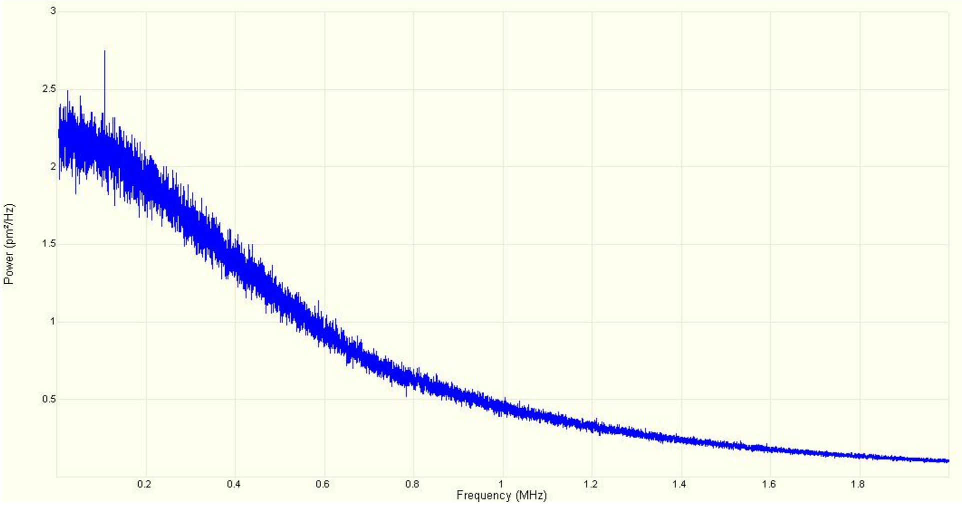

Figure 4.13: Spectral information of the AC probe cantilever, whose force curve is given in figure 4.11, obtained using the thermal tune technique.

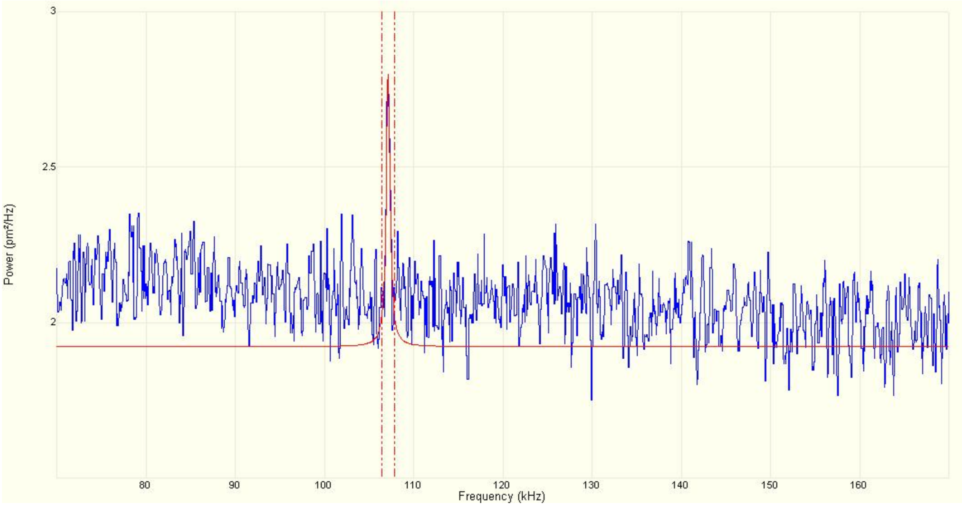

Figure 4.14: Spectral information zoomed near the resonance with Lorentzian model least square fit (red curve) of the AC probe cantilever, whose full spectral information and force curve are given in figures 4.13 and 4.11 respectively, obtained using the thermal tune technique.

4.3 Electrical characterization

4.3.1 AC capacitance measurement

Capacitance imaging have been performed using the setup illustrated in figure 1.3, which is based AC current sensing and lock-in detection technique commonly used for standard impedance measurement, to electrically calibrate the fabricated DC and AC probes. The instrument consists of a commercial AFM (Nanotec Electronica S.L) coupled to a custom-made current-to-voltage amplifier connected to the AFM tip. While scanning in contact over the surface under force feedback control, a sinusoidal input voltage signal, $\upsilon_{AC}(\omega)$, is applied between the AFM probe and the bottom electrode of the sample, and the AC current $\iota_{AC}(\omega)$ that flows through the sample is measured by the current amplifier. The amplified signal is fed into an analogue lock-in board included in the AFM electronics, which measures the in-phase and out-of-phase components of the current, thus extracting the real part (conductance, G) and imaginary part (susceptance, B), respectively, of the sample admittance (the inverse of the impedance, 1/Z). The lock-in analogue outputs are then sampled simultaneously to the AFM control signals by the 16 bit 15 kS s^{-1} analogue-to-digital (ADC) board of the AFM electronics. Thus, simultaneously to the acquisition of topography, images of conductance G and susceptance B are acquired in real time. Specifically, as B $= \omega C$, the capacitance image is obtained directly from the imaginary part of the admittance [4].

The total capacitance C measured in contact mode is the sum of several capacitance contributions, as illustrated in figure 1.4. Five capacitors in parallel corresponding to the tip apex C_{apex} (the local capacitance), the tip cone C_{cone}, the cantilever $C_{cantilever}$, and the chip C_{chip} (which mechanically supports the cantilever) and the holder C_{holder} (which accounts for all the parasitic of the AFM probe holder), are assumed to exist. Given the large distance between the surface and the holder, it is assumed to be constant with respect to nanometric changes in tip-substrate distance. But the role played by the apex is just the reverse to the role played by the probe holder. The contribution of the apex to the total capacitance signal is negligible in absolute term but its variation becomes dominant when small distance variations are involved [4].

The chip and cantilever contributions to the total capacitance signal can be modeled with a tilted rectangular plane capacitor. To this end the contribution of the cantilever of length (l), width (w), and tilt angle of α from the underlying conducting substrate to the total capacitance signal is mathematically expressed as [4,5],

$$C_{lever}(z) = \frac{\epsilon_0 w \tan^2(\alpha)}{\alpha^2 \tan(\frac{\alpha}{2})} \ln(1 + \frac{2l \tan(\frac{\alpha}{2})}{z + H}), \tag{4.3.1}$$

where z is the distance between the tip apex and the surface of the underlying electrode, and H is the tip apex height. Assuming a model of a truncated cone with spherical tip apex of radius R and half cone aperture angle θ_{cone}, the tip cone contribution to the total capacitance is given by [6],

$$C_{cone}(z) = \frac{-8\pi\epsilon_0}{(\pi - \alpha)^2}[f_1(\ln(f_1) - 1) - f_2(\ln(f_2) - 1) - \sin(2\theta_{cone}) \times (H \ln(2f_1) - \delta \ln(2f_2))], \tag{4.3.2}$$

where $f_1 = z + H - \frac{\delta}{2}$, $f_2 = z + \frac{\delta}{2}$ and $\delta = \frac{R}{(\tan(2\theta_{cone}))^2}$. Finally the capacitance term of the tip apex can be expressed as [5,7],

$$C_{apex}(z) = 2\pi\epsilon_0 R \ln(1 + \frac{R(1 - \sin(\theta_{cone}))}{z}). \tag{4.3.3}$$

To calibrate the tip geometry and to observe the capacitance coupling between the probes and the sample using the setup shown in figure 1.3, an AC voltage with angular frequency ω was applied between the probe and a conductive substrate (HOPG). The amplitude of the probe oscillation at 2ω as a function of tip-sample distance was measured and the capacitance gradient was calculated from it.

As described in [8], the applied voltage induces an electrostatic force on the probe given by:

$$F_{ele}(t) = \frac{1}{2}\frac{dC(z)}{dz}V^2, \tag{4.3.4}$$

where $\frac{dC(z)}{dz}$ is the capacitance gradient in the vertical direction and V is the sinusoidal applied voltage. As the force depends on the square of the applied voltage, the force has a component at the double of the applied frequency, 2ω, with amplitude,

$$|F_{2\omega}(z, \epsilon_r)| = \frac{1}{4}|\frac{dC(z, \epsilon_r)}{dz}|v_{in}^2. \tag{4.3.5}$$

If the frequency is well below the mechanical resonance of the probe cantilever, the cantilever oscillates at 2ω with deflection amplitude equal to

$$|D_{2\omega}(z)| = \frac{F}{k} = \frac{1}{4k}|\frac{dC(z)}{dz}|v_{in}^2, \tag{4.3.6}$$

where k is, as usual, the force constant of the cantilever. The capacitance gradient can then be obtained from the probe oscillation as,

$$|\frac{dC(z)}{dz}| = |D_{2\omega}(z)|\frac{4k}{v_{in}^2}. \tag{4.3.7}$$

Figure 4.15 shows the capacitance gradient between a prototype DC-probe and the conductive substrate as a function of the tip-sample distance. The capacitance gradient can be fitted to the theoretical predictions in equations 4.3.1-4.3.3. For the specific contribution of the apex, Hudlet et al. [7] derived an analytical model for the force (and hence for the capacitance gradient) as,

$$\begin{aligned} C'(z) = 2\pi\epsilon_0\{&\frac{1}{\ln[\tan(\frac{\theta}{2})]^2}[\ln(\frac{H}{z+R(1-\sin\theta)}) - 1 + \frac{R\cos^2(\theta)/\sin(\theta)}{z+R(1-\sin(\theta))}] \\ &+ \frac{R^2(1-\sin(\theta))}{z(z+R(1-\sin(\theta)))}\}. \end{aligned} \tag{4.3.8}$$

The capacitance gradient data in figure 4.15 was fitted to the theoretical prediction in equation 4.3.8 giving a cone aperture angle of 29±1 and an apex radius of 40±2nm. Figure 4.16 shows the capacitance gradient between an AC-probe and the conductive substrate as a function of the tip-sample distance. The applied oscillating potential had an amplitude of 10V and a frequency of 10kHZ. The capacitance gradient shown in Figure 4.16 was also fitted with the Hudlet formula 4.3.8 giving a cone aperture angle of 26±1 and an apex radius of 50±2nm. These experiments were performed at IBEC.

We emphasize the excellent agreement of the experimental results with the theoretical model in a long range of tip-sample distances (beyond 350 nm in both cases).

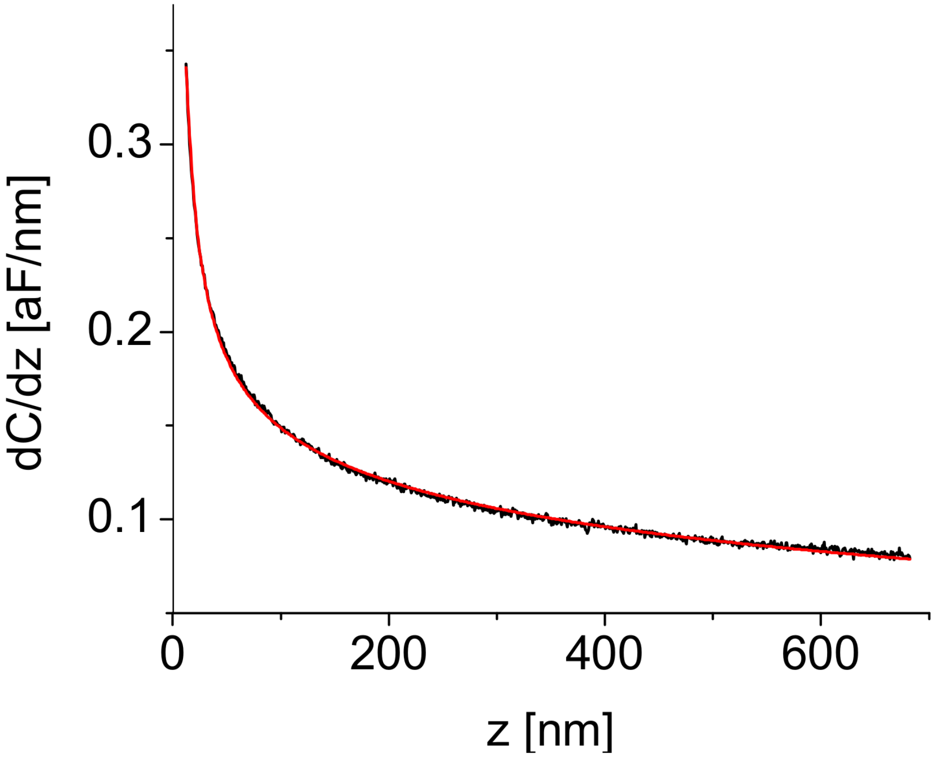

Figure 4.15: Capacitance gradient approach curve between a DC prototype probe and a conductive substrate. The good fit with theory (red curve) shows the good electrical behavior of the probe.

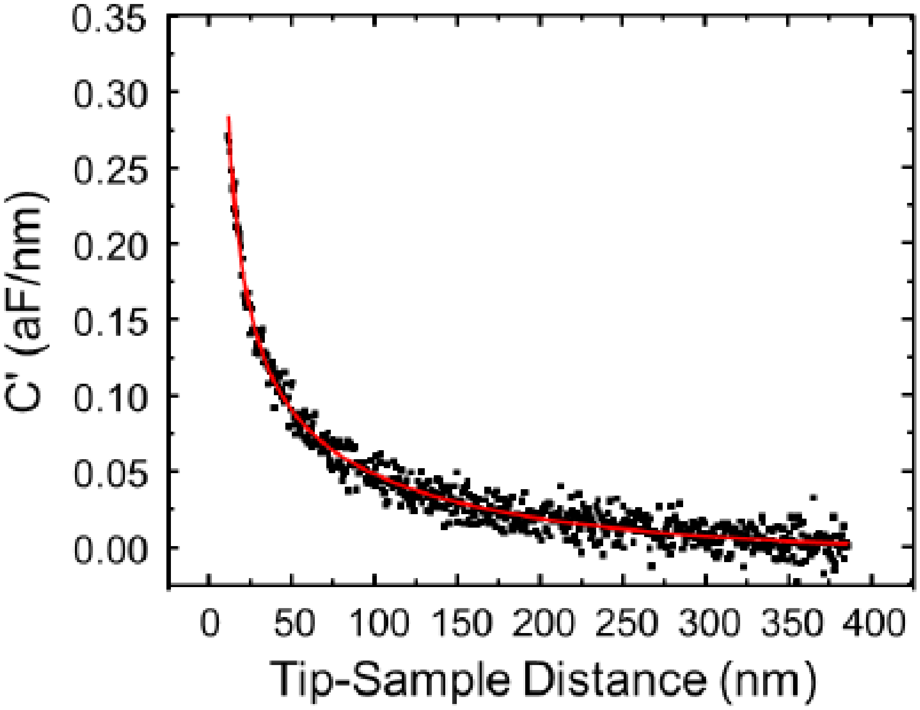

Figure 4.16: Capacitance gradient (which is proportional to the force) for a probe with an applied AC voltage approaching a conductive substrate (symbols) and fitting with the Hudlet formula (red solid line). From the fit a cone aperture angle of 26 ± 1 and an apex radius of 50 ± 2 nm are obtained.

Since the theoretical model only takes into account the contribution from the tip of the probe (with no contribution coming from the cantilever), this agreement between the theory and the experiments suggests that the stray contribution of the cantilever has been reduced to a non-detectable limit with our probe design.

4.3.2 DC measurements

Further electrostatic force microscopy (EFM) experiments were performed at IBEC to characterize the fabricated probes. In the first experiment simultaneous topographic and EFM images of silicon oxide nanostructures on a highly doped silicon substrate shown in figure 4.17 were taken with an AC-probe; the EFM image was acquired in non-contact mode at constant height (45nm) from the highly doped silicon substrate by applying a DC voltage of 9V between the tip and the substrate. The capacitance gradient image was then extracted from the changes in the normal force due to the electrostatic force between the probe and the sample [9]. The good lateral resolution and good EFM image demonstrate the correct operation of the conductive probes.

In the second measurement the static deflection of a probe cantilever due to the probe-substrate capacitance coupling was measured as a function of the DC applied voltage at constant distance from the sample (∼500 nm). Figure 4.18 shows the capacitance coupling between the different parts of the probe and the conducting substrate. The contributions from the tip apex and tip cone is negligible in this experiment [9] hence, the static deflection of a probe in the setup shown in figure 4.18 is predominantly due to the capacitance coupling between the probe cantilever and the conducting substrate. Figure 4.19 shows the static deflection of an AC-probe held at a constant distance (∼500 nm) from the conducting substrate as a

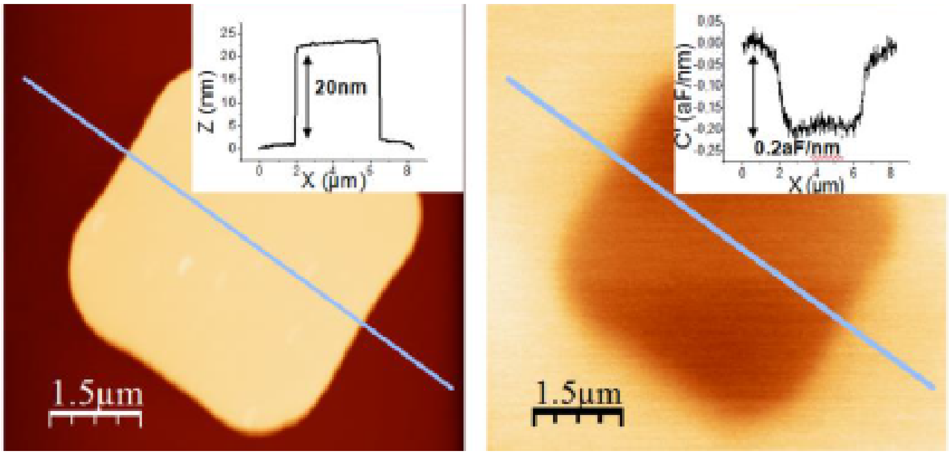

Figure 4.17: Images taken with the fabricated probes (AC mode). Topography (center) and constant-height DC-EFM image (right) of a silicon dioxide nanostructure on a doped silicon substrate.

function of DC applied voltage. The capacitance coupling between the probe and the metallic substrate was then compared with the analytical expression derived in [9] (solid lines in Figure 4.19) for both a cantilever fully covered with the metallic layer and a cantilever with a patterned metallic layer. For the calculation we used the measured values of the cone height, probe length and patterned metal line width, with no fitting parameters. The experimental results follow closely the theoretical predictions for the patterned metallic layer thus showing that the cantilever capacitive coupling was significantly reduced with respect to that of a cantilever fully covered by the metallic coating (red plot), which was consistent with the design of the probes.

Finally Peak force-tunneling AFM (TUNA) current measurements between the probes and a conducting substrate as a function of a DC bias voltage were performed with a commercial AFM equipment (Bruker Dimension icon AFM) at Barcelona Microelectronics Institute (IMB-CNM). TUNA differ from conductive AFM (C-AFM) in that the current range is much lower for TUNA (sub-pA to nA) than for C-AFM

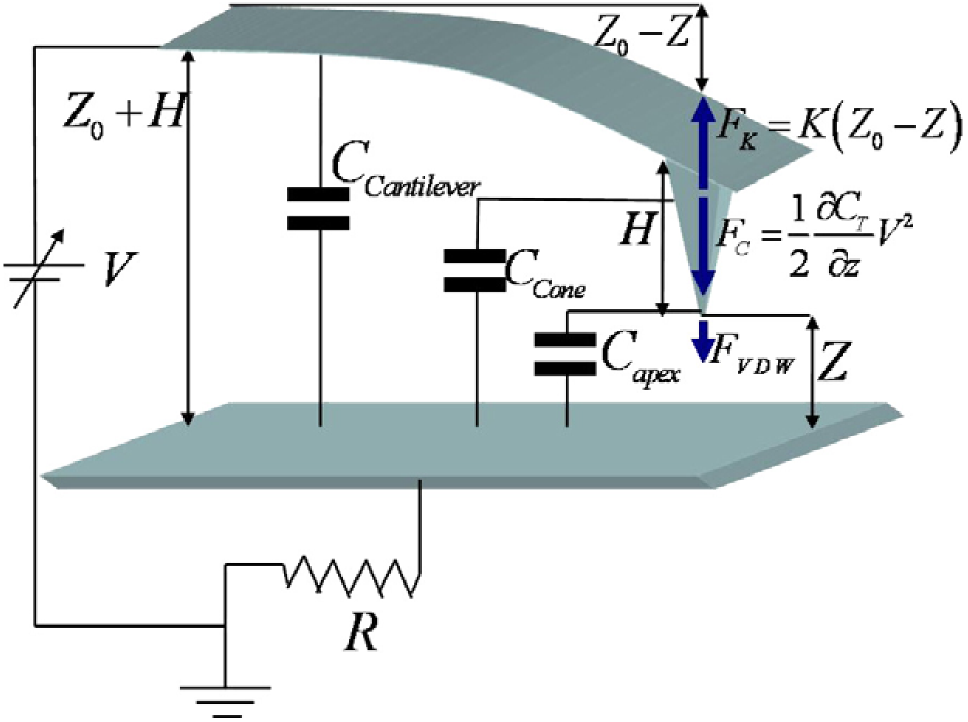

Figure 4.18: Diagrammatical representation of the probesubstrate system for static deflection study of conducting probes under DC bias [9].

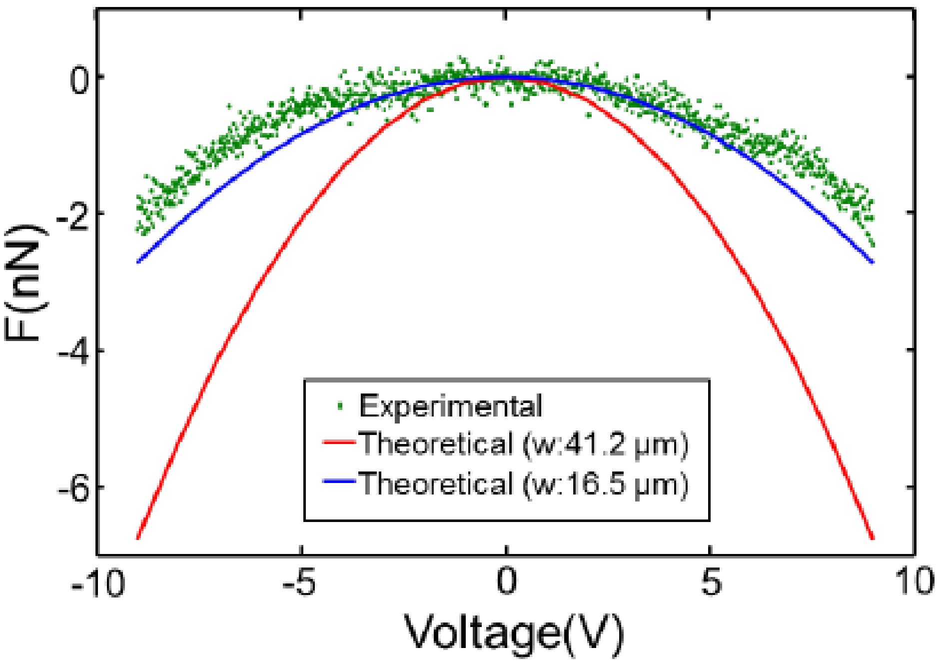

Figure 4.19: Experimental static deflection of a probe as a function of the DC applied voltage at a tip-substrate distance of 500 nm (symbols), compared to the theoretical value for the measured probe dimensions and no fitting parameters (blue line). This shows a reduced capacitive coupling of the probes when compared to the theoretical calculation for a fully metal covered probe (red line).

(nA to mA). The conducting substrate was 100nm thick gold metal structures on a 2 inch in diameter silicon dioxide wafer. The substrate contact was made with a micromanipulator. Figure 4.20 is optical microscope image of substrate contact area with the micromanipulator (left) and contact between the probe tip and the substrate (right). In this electrical measurement experiment the conductive probe was held at ground potential and a positive or negative polarity DC bias was applied on the conducting substrate. The resulting current between the conductive probe and the substrate was recorded with the current sensing element of the equipment. Figure 4.21 is current (nA) between a prototype DC-probe and the conducting substrate as a function a positive polarity DC bias at the conducting substrate. Positive polarity DC bias at the conducting substrate was chosen to avoid electrochemical oxidation of the silicon tip. And figure 4.22 is the current (nA) between an AC probe and a conducting substrate as a function of DC bias at the substrate. In the fabricated AC probes electrochemical oxidation of the probe tip is not an issue as the tip material of the probe is gold metal. Hence, both negative and positive polarity DC bias voltage was used in this experiment as it is apparent in figure 4.22. Linear relationship between the current and the DC bias voltage was observed indicating ohmic electric contact between the probes tip and the conducting substrate.

Initially we had a problem with the DC current measurements between the prototype DC probes and a conducting substrate. This is because as the tip material in these probes is silicon, thin native oxide grew when it was left for some time in the atmosphere. Hence the thin native oxide should be broken to have DC contact with the conducting substrate. To this end we were able to break the native oxide by applying higher DC applied voltage between the probe tip and the substrate. We

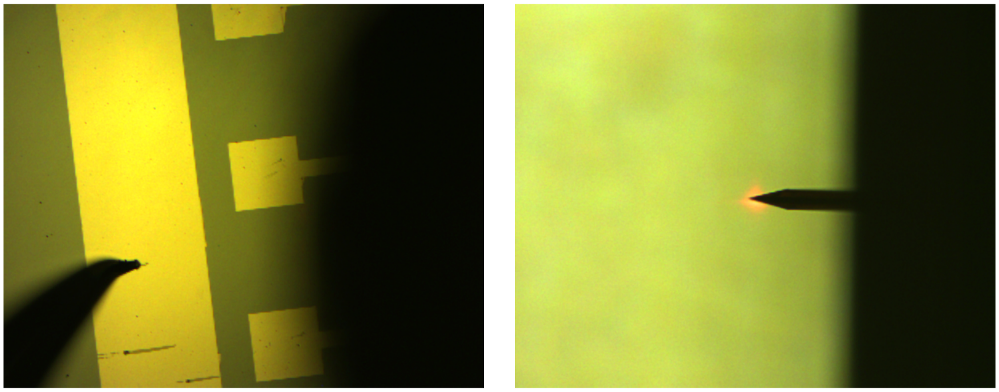

Figure 4.20: Optical microscope image of contact between micromanipulator and the conducting substrate (left) and contact between the conducting substrate and a probe tip (right).

used external power source to break the native oxide on the tips as the DC source of the AFM equipment is not enough for this purpose. The polarity of the DC applied voltage at the substrate should be positive as negative polarity DC bias at the substrate will further increase the thickness of the native oxide on the tip due to electrochemical oxidation process.

We observed similar problems in the final DC probes as was in the prototype DC probes. We used similar strategy to break the thin native oxide in the probe tips by applying higher DC bias between the probes tip and the conductive substrate. Here also we used positive polarity DC bias at the substrate to avoid electrochemical oxidation of the probes tips. The DC bias at which the native oxide broke was not the same in all the DC probes used in this experiment. In some probes it broke around 15-20V but in some others it go as higher as 50V. Besides the problem of DC contact due to the thin native oxide on the probes tip, we also observed that the current between the DC probes tip and the conducting substrate was not stable. As we move the probe into a new point in the conducting substrate with only few millivolts DC

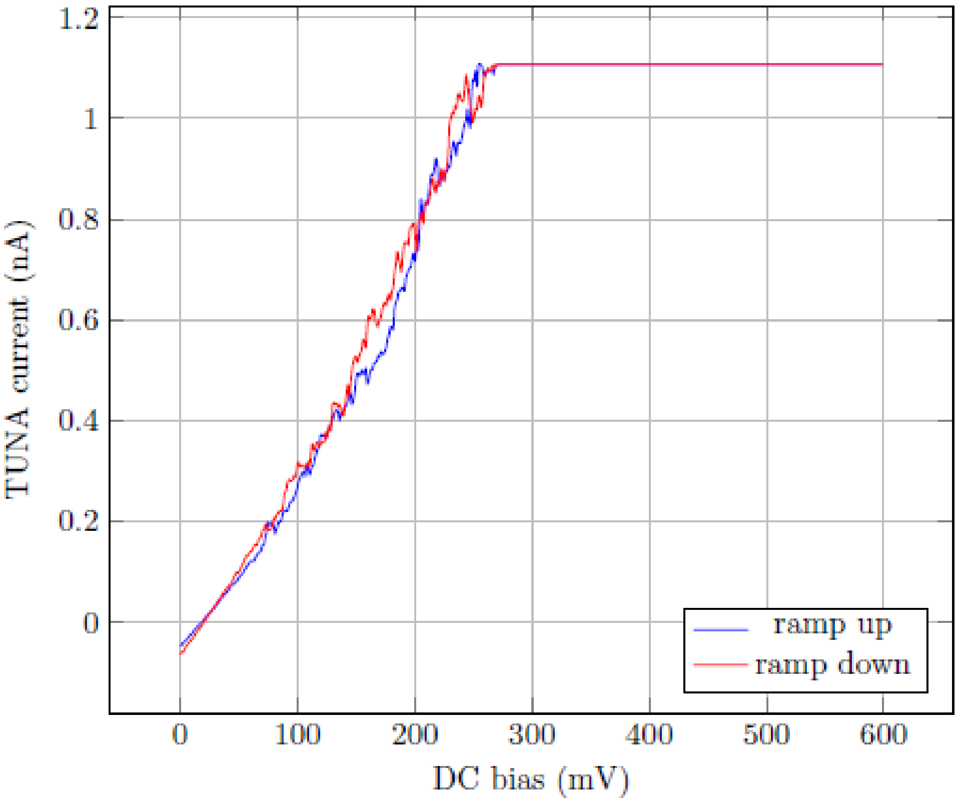

Figure 4.21: Current (nA) as a function of DC applied voltage between a prototype DC probe and a conducting substrate. Linear relationship between the DC applied voltage and the resulting current shows that the contact between the probe tip and the conducting substrate is ohmic.

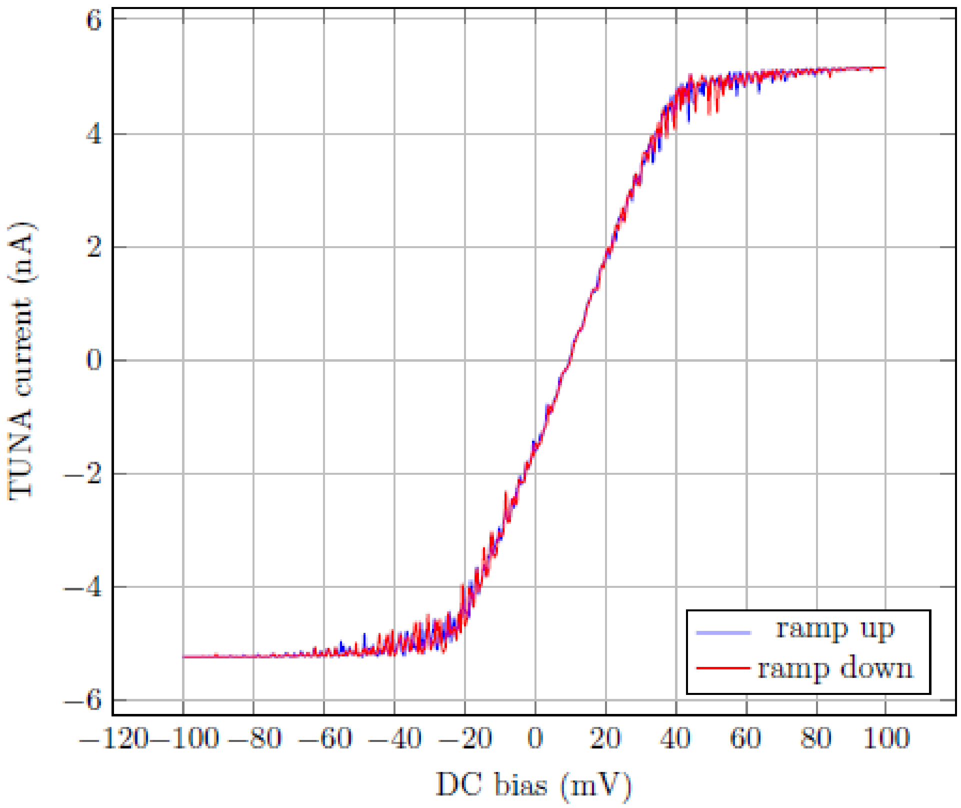

Figure 4.22: Current (nA) as a function of DC applied voltage between an AC probe and a conducting substrate. Linear relationship between the DC applied voltage and the resulting current shows that the contact between the probe tip and the conducting substrate is ohmic.

bias between the DC probes tip and the conducting substrate, the current dies out. We have not observed such effect in the AC probes. As this is critical problem, we stopped further electrical characterization of the DC probes.

To address the problem of native oxide in silicon, we made technology tests of titanium and tantalum silicide in section 3.16. But we found that the etching conditions for silicon nitride passivation layer available in IMB-CNM clean room facility have poor selectivity towards these silicide layers. Hence, further tests are needed to address the selectivity issue of titanium or tantalum silicide layers for the fabrication of optimum conductive SPM probes for contact mode electrical and topographical characterization of samples in liquid environment.

Bibliography

[1] J. P. Cleveland, S. Manne, D. Bocek, and P. K. Hansma. A nondestructive method for determining the spring constant of cantilevers for scanning force microscopy. *Review of Scientific Instruments*, 64(2):403–405, 1993.

[2] Jeffrey L. Hutter and John Bechhoefer. Calibration of atomic-force microscope tips. *Review of Scientific Instruments*, 64(7):1868–1873, 1993.

[3] John E. Sader, James W. M. Chon, and Paul Mulvaney. Calibration of rectangular atomic force microscope cantilevers. *Review of Scientific Instruments*, 70(10):3967–3969, 1999.

[4] L Fumagalli, G Ferrari, M Sampietro, I Casuso, E Martnez, J Samitier, and G Gomila. Nanoscale capacitance imaging with attofarad resolution using AC current sensing atomic force microscopy. *Nanotechnology*, 17(18):4581, 2006.

[5] B. M. Law and F. Rieutord. Electrostatic forces in atomic force microscopy. *Phys. Rev. B*, 66:035402, Jun 2002.

[6] A Gil, J Colchero, J Gomez-Herrero, and A M Baro. Electrostatic force gradient signal: resolution enhancement in electrostatic force microscopy and improved Kelvin probe microscopy. *Nanotechnology*, 14(2):332, 2003.

[7] S. Hudlet, M. Saint Jean, C. Guthmann, and J. Berger. Evaluation of the capacitive force between an atomic force microscopy tip and a metallic surface. *The European Physical Journal B - Condensed Matter and Complex Systems*, 2(1):5–10, 1998.

[8] L. Fumagalli, D. Esteban-Ferrer, A. Cuervo, J.L. Carrascosa, and G. Gomila. Label-free identification of single dielectric nanoparticles and viruses with ultraweak polarization forces. *Nature Materials*, 11:808–816, 2012, Supplementary information.

[9] J Toset, I Casuso, J Samitier, and G Gomila. Deflectionvoltage curve modelling in atomic force microscopy and its use in DC electrostatic manipulation of gold nanoparticles. *Nanotechnology*, 18(1):015503, 2007.

Chapter 5

Conclusions

We have developed insulated conductive SPM probes for scanning impedance microscopy characterization in liquid environment. The probes have been developed due to the need of characterizing olfactory biosensor devices within the European project BOND. We have made separate developments for DC probes (for DC electrical measurements in contact mode) and AC probes (to measure the AC response in dynamic mode).

We have demonstrated the batch fabrication of conductive SPM probes (cantilevers integrated with sharp tetrahedral tips) insulated except at the very tip apex and the contact pad area with standard microfabrication processes. The tip radius of the fabricated probes obtained from topographic image resolution and electrical calibration techniques show very good agreement and gave tip radius values in the range of 30-50nm. These tip radius values satisfy the specification for the probes tips as required by the BOND project (which was tip radius value of less than 100nm). The force constant of the fabricated probes was calibrated using the thermal tuning technique. The force constant values of the characterized probes were found to satisfy the specification values for the probe cantilevers as required by the BOND project (which was force constant values in the range of 0.1-1N/m for the DC probes and in the range of 5-20N/m for the AC probes).

Capacitance gradient between the fabricated probes and a conductive substrate (HOPG) as a function of tip-substrate distance was measured by a setup with attofarad resolution at IBEC. These measurements demonstrated that the stray capacitance between the different parts of the probes (cantilever, tip cone and probe substrate) and the conductive substrate was reduced to a non-detectable limit for both DC and AC probes. Static deflection of an AC probe cantilever due to the probe-substrate capacitance coupling was measured as a function of DC applied voltage at constant tip-substrate distance (∼500 nm) at IBEC. Capacitance coupling between the fabricated AC probe cantilever and the conductive substrate was highly reduced compared to what will be between the conductive substrate and a probe cantilever with full metallic coating. These results are consistent with the design of the probes. We claim, to the best of our knowledge, that we are the first in fabricating insulated conductive SPM probes with much reduced stray capacitance contributions. Simultaneous topography and EFM measurements of a silicon oxide nanostructures on a highly doped silicon substrate were also performed at IBEC with AC probes. Very good agreement between topography and EFM images was observed, which shows good electrical behavior of the probes. Finally, tunneling AFM (TUNA) current measurement between AC probes and a conductive substrate (gold structures on a 2inch silicon oxide wafer) as a function of a DC applied voltage was performed in contact mode at IMB-CNM to study the contact behavior between the probes tip and the substrate. Linear relationship between the measured current and the applied DC bias was observed. The linear relationship obtained between the current and the DC applied voltage shows that an ohmic contact between the probe tip and the substrate was achieved. The dielectric coating is expected to minimize the parasitic conductance between the probe cantilever and samples in liquid media. Therefore, it is expected that the AC probes can be utilized for local topographic and electrical characterization of small signal samples in liquid environment such as biological samples in their native physiological environment.

In the DC probes, as the tip material is silicon, the native oxide on the tip blocked electrical contact between the probe tip and the conductive substrate in TUNA current measurement. By applying higher DC applied voltage as high as 50V between the DC probes and the conductive substrate, we were able to break the native oxide. Linear relationship between the applied DC voltage and the measured TUNA current was observed after the native oxide had been broken at higher DC voltage. Unfortunately, the TUNA current between the DC probes and the conductive substrate was not stable, i.e., the TUNA current died out when we moved the probe tip to a new position in the conducting substrate. To address the issue of native oxide, we performed titanium and tantalum silicide test runs. But we found that the silicon nitride etching conditions which are available at IMB-CNM clean room facility have poor selectivity to titanium and tantalum silicide layers. We believe that further test is needed to address the titanium or tantalum silicide selectivity problem to fabricate optimum DC probes for topographic and electrical characterization of samples in liquid environment.

We acknowledge that our fabricated probes lags behind the standard commercial AFM probes in terms of tip sharpness. The sharpest tips we have fabricated have tip radius value of around 30nm compared to sub-10nm for standard commercial AFM probes. We believe that pushing our fabrication technology towards the fabrication of insulated conductive SPM probes with comparable or better tip sharpness to that of the standard commercial AFM probes is an open area for future research.

Appendix

List of publications and conference presentations

Peer reviewed articles

[1]. Y. Birhane, J. Otero, F. Perez-Murano, L. Fumagalli, G. Gomila, and J. Bausells. Batch fabrication of insulated conductive scanning probe microscopy probes with reduced capacitive coupling. Microelectronic Engineering, vol. 119 (2014) pp. 44-47 (DOI: 10.1016/j.mee.2014.01.018).

Conference presentations

[1]. G. Tosolini, Y.M. Birhane, and J. Bausells. Advances in the development of micro-nanomechanical cantilever devices. Nanoselect Annual Meeting 2010, 14-16 July 2010, Sant Feliu de Guxols (Spain), poster presentation.

[2]. G. Tosolini, Y.M. Birhane, F. Perez-Murano, and J. Bausells. Piezoresistive and MOSFET cantilevers for measuring (biomolecular) forces. Nanomaterials based biosensors and biosystems (NANOJASP 2010), 29-30 November 2010, Barcelona (Spain), poster presentation.

[3]. J. Bausells, G. Tosolini, Y.M. Birhane, and F. Perez-Murano. Piezoresistive probes for (biomolecular) force sensing. The 8th Annual IEEE International Conference on Nano/Micro Engineered and Molecular Systems (IEEE-NEMS 2013), 7-10 April 2013, Suzhou (China), oral presentation. Proceedings of IEEE-NEMS 2013 (IEEE Cat. N: CFP13NME-ART, ISBN: 978-1-4673-6351-8), pp. 1112-1115 (DOI: 10.1109/NEMS.2013.6559917).

[4]. Y. Birhane, G. Gramse, G. Gomila, and J. Bausells. Fabrication of conductive scanning probe microscopy (C-SPM) probes for local electrochemical analysis of biological samples. 10th International Workshop on Nanomechanical Sensing (NMC 2013), 1-3 May 2013, Stanford, CA (USA), poster presentation.

[5]. Y. Birhane, J. Otero, F. Perez-Murano, G. Gomila, and J. Bausells. Batch-fabrication of insulated conductive Scanning Probe Microscopy probes with reduced capacitive coupling. 39th International Conference on Micro and Nano Engineering (MNE 2013), 16-19 September 2013, London (UK), oral presentation.